INTEGRATING BIOCHEMISTRY AND METABOLISM INTO BIOGEOCHEMICAL REACTION MODELING

by

QIONG WU

A DISSERTATION

Presented to the Department of Earth Sciences
and the Division of Graduate Studies of the University of Oregon
in partial fulfillment of the requirements
for the degree of
Doctor of Philosophy

June 2021

DISSERTATION APPROVAL PAGE

Student: Qiong Wu

Title: Integrating Biochemistry and Metabolism into Biogeochemical Reaction Modeling

This dissertation has been accepted and approved in partial fulfillment of the requirements for the Doctor of Philosophy degree in the Department of Earth Sciences by:

Prof. Qusheng Jin	Chairperson/Advisor
Prof. Mark Reed	Core Member
Prof. Matthew Polizzotto	Core Member
Prof. Stilianos Louca	Institutional Representative

and

Andy Karduna	Interim Vice Provost for Graduate Studies

Original approval signatures are on file with the University of Oregon Division of Graduate Studies.

Degree awarded June 2021

DISSERTATION ABSTRACT

Qiong Wu

Doctor of Philosophy

Department of Earth Sciences

June 2021

Title: Integrating Biochemistry and Metabolism into Biogeochemical Reaction Modeling

Microbial kinetics study on the microbial metabolic rates and their dependence on biological and environmental conditions. It has been widely used in biogeochemical models. However the empirical nature of microbial kinetics masks the mechanisms of growth kinetic parameters and challenges the applicability to natural environments. Whereas metabolism analysis can heal reveal the mechanism how enzymatic kinetics affect the microbial kinetics. Thus it is necessary to bridge the gap between microbial kinetics and cell metabolism. We firstly implemented cell metabolism of a model methanogen which can utilize a spectrum of substrates to produce methane gas. We validated the model and explored the mechanisms of resource allocation. We then focus on the metabolism of methanol methanogenesis. The simulation results in methanol concentrations ranging from 0.001 mM to 100 mM, proteome allocation shows a trade-off between growth related sector and methanogenesis sector. In addition, the model results link the rate-law parameters to kinetically-influential enzymes, and illustrate the plasticity and trade-off of the parameters as a manifestation of cellular resource allocation. Then we apply the microbial kinetics by integrating the physiological acclimation to individual functional group of acetoclastic methanogen including

Methanosarcina and *Methanosaeta* species. Current models usually treat microbes as auto catalysts, and couple methane production to cell growth by using rate laws and constant kinetics parameters. However, microbes are capable of acclimating and adapting to ambient environment by modulating kinetic properties. Here, we constructed an acclimation model to describe the variations of methanogenesis parameters with substrate concentrations and thermodynamic conditions, as experienced by microbes in environments of different trophic status. Our results show that modeling microbes as a self-adapting catalyst is critical for predicting methanogenesis kinetics. At last, we applied microbial kinetics to microbial communities to study the temperature sensitivity of anaerobic organic matter decomposition. The model framework included the transition from soil organic matter to dissolved organic matter by extracellular enzymes, fermentation, acetoclastic and hydrogenotrophic methanogenesis by fermenters and methanogens. We applied the enzyme-assisted Arrhenius, Cardinal temperature equations and Monod equation to explore the temperature sensitivity of microbial kinetics. Results show that fermentation is the bottleneck of the anaerobic organic matter degradation.

This dissertation includes unpublished material

CURRICULUM VITAE

NAME OF AUTHOR: Qiong Wu

GRADUATE AND UNDERGRADUATE SCHOOLS ATTENDED:

University of Oregon, Eugene
Beijing Normal University, Beijing, China
Minzu University of China, Beijing, China

DEGREES AWARDED:

Doctor of Philosophy, Earth Sciences, 2021, University of Oregon
Doctor of Engineer, Environmental Sciences, 2015, Beijing Normal University
Bachelor's degree, Environmental Sciences, 2010, Minzu University of China

AREAS OF SPECIAL INTEREST:

Biogeochemical Modeling
Methanogenesis
Carbon Cycle

PROFESSIONAL EXPERIENCE:

Research assistant, University of Oregon, 2017.9-2021.6
Teaching assistant, University of Oregon, 2020.9~2020.12, 2020.3~2020.6
2019.3~2019.6, 2018.3~2019.6

GRANTS, AWARDS, AND HONORS:

Johnston Award, Department of Earth Sciences, 2017

Summer Fellowship, Department of Earth Sciences, 2018

Stovall Fellowship, Department of Earth Sciences, 2018

Stovall Fellowship, Department of Earth Sciences, 2019

Stovall Fellowship, Department of Earth Sciences, 2020

PUBLICATIONS:

ACKNOWLEDGMENTS

I would like to thank my advisor, Professor Qusheng Jin, for being a supportive and dedicated advisor and for his big help with revising manuscripts as well as training my ability of reasoning and independent thinking. His dedication to high-quality science, his vision and optimistic attitude has helped me to become a better researcher and a better person. I would also like to thank the rest of my dissertation committee and comps committee for their generous guidance, help, and support during the past four years – Mark Reed, Matthew Polizzotto, Stilianos Louca, and Frederick Colwell, their encouragement have given me lots of confidence and courage. Also I would like to thank Scott Bridgham and Rongzhong Ye, who have helped me with the study on temperature sensitivity. I am also grateful to everyone at Department of Earth Sciences of University of Oregon. They have made and are making this department an amazing and comfortable place to stay. I am so fortunate to have had these wonderful officemates and friends in our department, who have given me a beautiful memory of the graduate journey at Eugene: Adrian Broz, Brooke Hunter, Kathy Trafton, Lissie Connors, Gabbie Lafayette, Kellum Tate-Jones, Gordon Bowman, Markus Koeneke.

I owe a debt of thanks to my families: my husband, my parents, and my younger sister, who always stand by my side, tolerate the grumpy side of me, and support the critical decisions of my life. I also want to thank my friends who has accompanied me for quite long time, some of these friendship are longer than 10 years. Their tolerant, patient, humorous and brave characteristics have influenced me and also made me a better person.

At last, I want to thank the NSF EAR-1636815, 753436, and the NASA Grant

NNX16AJ59G for funding my research.

TABLE OF CONTENTS

LIST OF FIGURES

Figure Page

Chapter II

Figure Page

Chapter IV

Figure Page

Chapter V

LIST OF TABLES

CHAPTER I INTRODUCTION

Microbial kinetics analyze the microbial metabolic rates and their dependence on biological and environmental conditions. Rate laws of microbe kinetics such as the Monod equation depicts the microbial growth rate, and has gained wide support from laboratory investigations. However, its empirical nature masks the physical meanings of growth kinetic parameters and challenges its applicability to natural environments. Whereas, metabolism of microbial cell can help understand the resource allocations and their relationship with kinetic parameters. Chapter II shows how to how to bridge the gap between the microbial kinetics and cell metabolism. We simulate the growth of a model methanogen across a spectrum of nutrient concentrations, including those of laboratory bioreactors and pristine sediments, and the goal is to investigate how microbial growth kinetics is influenced by the optimal allocation of cellular resources. By combining kinetic modeling with optimization of cellular resource allocation, our modeling approach uncovers emergent properties arising from the kinetics of methanogenesis enzymes. These results support the application of mechanistic driven microbial kinetics in biogeochemical models, and also link rate-law parameters to kinetically-influential enzymes, and illustrate the plasticity and trade-off of the parameters as a manifestation of cellular resource allocation. The results also open new perspectives for microbial kinetic studies, from extrapolating laboratory observations to natural environments to the applications of metabolic scaling laws.

After bridging the gap between cell metabolism and microbial kinetics, we tried to explore how to integrate the mechanisms of physiological acclimation of single microbial cell to an individual functional group using reactive transport model.

Methanogenic microorganisms face the challenge of limited energy resources in natural environments and this observation has important implications for interpreting and predicting the dynamics of methane emissions to the atmosphere. Current models treat microbes as a self-catalyst, and couple methane production to cell growth by using rate laws and constant kinetic parameters. However, microbes are capable of acclimating and adapting to ambient environments by modulating their kinetic properties. Here we show that modeling microbes as a self-adapting catalyst is critical for predicting methanogenesis kinetics. Our approach extrapolates laboratory observations to natural environments without introducing a new parameter, and has broad importance in biogeochemical kinetics.

In Chapter IV, we applied the microbial kinetics to microbial community by studying the temperature sensitivity of anaerobic organic matter degradation. The Q_{10} coefficient is the ratio of reaction rates at two temperatures 10 °C apart, and has been widely applied to quantify the temperature sensitivity of organic matter decomposition. However, biogeochemists and ecologists have long recognized that a constant Q_{10} coefficient does not describe the temperature sensitivity of organic matter decomposition accurately. To examine the consequence of the constant Q_{10} assumption, we built a biogeochemical reaction model to simulate anaerobic organic matter decomposition in peatlands in the Upper Peninsula of Michigan, USA, and compared the modeling results to the predictions with Q_{10} coefficients. By accounting for the reactions of extracellular enzymes, mesophilic fermenting and methanogenic microbes, and their temperature responses, the biogeochemical model reproduces the observations of previous laboratory incubation experiments, and confirms that fermentation limits the progress of anaerobic

organic matter decomposition. The modeling results illustrate the oversimplification inherent in the constant Q_{10} assumption and how the assumption undermines the kinetic prediction of anaerobic organic matter decomposition. In particular, the model predicts that at <37^{o}C, the decomposition rate increases almost linearly with increasing temperature, which stands in sharp contrast to the exponential relationship given by the Q_{10} coefficient. As a result, the constant Q_{10} approach tends to underestimate the rates of organic matter decomposition within the temperature ranges where Q_{10} values are determined, and overestimate the rates outside the temperature ranges. The results also show how biogeochemical modeling, combined with laboratory experiments, can help uncover the temperature sensitivity of organic matter decomposition arising from underlying catalytic mechanisms.

Chapter V focuses on analyzing the energy metabolism of acetoclastic methanogenesis of *Methanosarcina barkeri*. So far, there are several studies describing the trade-off between rate and yield. These research emphasizes the trade-off from theoretical and macroscopic perspective without mechanistic understanding. Here we built an enzymatic kinetic model of acetoclastic methanogen based on Michaelis-Menten equation. Methanogens conserve energy via pumping out proton/sodium by membrane-associated enzymes, and the established chemiosmotic gradients generate proton motive force to sustain the complex biological processes such as biosynthesis. Here we analyzed the metabolism of the acetoclstic methanogenesis pathway to understand how acetotrophic methanogens allocate the energies for biosynthesis and methanogenesis to achieve the maximal growth rate. Our results show that all membrane associated enzymes function to alter the ATP flux and yield. In the meantime, ECH plays dominant roles in affecting the

growth rate, ATP flux and ATP yield. Our results also exhibit a significant trade-off between ATP flux and ATP yield due the variations in proton/sodium translocation numbers by membrane bound enzymes. In addition, the optimized ATP yield shows an increased linear correlation with available energy in the ambient environment, then reaching a constant when the available energy is high enough. The results suggest that methanogens tends to lower their conserved energy to adapt to the energy limitation environment. This acclimation mechanisms can also be applied to other microbes living at thermodynamic edge environment.

CHAPTER II BRIDGING THE GAP BETWEEN MICROBIAL KINETICS AND METABOLISM: A MODELING APPROACH

1. Introduction

The Monod equation is (Jin et al., 2013a; Panikov, 1995) the most commonly used rate law for predicting the kinetics of microbially-driven biogeochemical processes, such as methane bioproduction.(Button, 1998; Liu, 2007) The Monod equation shares the same mathematical structure as the Michaelis-Menten equation for enzyme reactions, and constrains methane production fluxes from substrate concentration C,

$$J = k \cdot \frac{C}{C + K}, \qquad (1)$$

by using two parameters, the rate limit k and the half-saturation constant K.

But unlike the Michaelis-Menten equation, the Monod equation is empirical, which leads to a misconception of microbial kinetics and erroneous predictions of biogeochemical fluxes. For example, substrate affinity is a key functional trait that determines microbial competitive fitness. But how to measure substrate affinity by using microbial kinetic parameters remains controversial. As another example, despite repetitive evidence for the significant difference in methanogenesis kinetics between laboratory cultures and natural methanogens, most current ecosystem and biogeochemical models are still based on the kinetic parameters of laboratory cultures, leading to the significant deviation of model predictions from field observations.

Here we explore the relationship between growth rates and nutrient concentrations by simulating the growth of a model methanogen Methanosarcina barkeri. Methanogen growth produces methane, a potent greenhouse gas, and hence is of environmental

significance. Like other unicellular organisms, methanogens acclimate to nutrient conditions by allocating finite cellular resources, including ATPs, ribosomes, and proteins, to methanogenesis, protein synthesis and biomass formation, and other intracellular processes (Enoki et al., 2011; Xia et al., 2009). We are interested in how cellular resource allocation influences the relationship between growth rates and the concentrations of external energy resources. For this purpose, we construct a kinetic model that focuses on the biochemical network of methanogenesis and energy conservation (fig 1a). We couple the network fluxes, including the fluxes of ATPs, to cell reproduction using genome-scale flux balance analysis (FBA) (Benedict et al., 2012; Shapiro et al., 2018), and optimize enzyme expressions under the constraints of proteome partition and ribosome allocation (fig 1b) (Berkhout et al., 2013; Hui et al., 2015; G. W. Li et al., 2014; Scott et al., 2010). This way, our approach goes beyond standard kinetic and stoichiometric metabolic modeling, and is related to dynamic metabolic optimization (Ewald et al., 2017; Villaverde et al., 2016) and resource allocation analysis (Goelzer & Fromion, 2011; Mori et al., 2016a). By explicitly simulating enzyme expressions and fluxes, we seek to uncover emergent metabolic properties that bear out the mechanism between cell metabolism and growth kinetic parameters.

We simulate methanogenic growth on methanol. Recently, methylotrophic methanogenesis, $\frac{4}{3}CH_3OH = \frac{2}{3}H_2O + \frac{1}{3}CO_2 + CH_4$, has been recognized as one of the dominant methanogenic pathways in marine settings (Zhuang et al., 2018). Our results include (1) model-derived emergent properties that distinguish microbial growth from inanimate systems, including the plasticity and trade-off of growth kinetic parameters, (2) mechanistic links between macroscopic growth kinetic parameters to the properties of

enzymes, and (3) illustration of trait plasticity and trade-off as an outcome of cellular resource allocation and a key component in applying the Monod equation.

2. Materials and Methods

2.1 Kinetic model

The kinetic model defines the metabolic state of *M. barkeri* using metabolite concentrations and represents methanogen growth as an initial value problem of ordinary differential equations (ODEs). Each ODE describes the rate at which a metabolite concentration changes with time *t*, and is constructed according to the principle of mass balance. Specifically, the ODE of metabolite j is

$$\frac{dC_{\mathrm{j}}}{dt} = \frac{1}{V_{\mathrm{j}}} \cdot \left(J_{\mathrm{j}} + \sum_{\mathrm{i}} \nu_{\mathrm{j,i}} J_{\mathrm{i}} \right) , \qquad (2)$$

where C_{j} is the concentration (mol·L^{-1}) of the metabolite, J_{j} is the diffusive flux (mol·s^{-1}) of methanol, carbon dioxide, or methane, J_{i} is the reaction flux of enzyme i (mol·s^{-1}), $\nu_{\mathrm{j,i}}$ is the stoichiometric coefficient of metabolite j in the reaction of enzyme i (negative for metabolite consumption), V_{j} is the volume of the compartment of metabolite j, which is either the cytoplasm volume V_{cyto} or the membrane volume V_{mem} (L). Chemiosmotic coupling builds membrane potential $\Delta\psi$, whose ODE is

$$\frac{d\Delta\psi}{dt} = \frac{F}{C_{\mathrm{m}}} \cdot \sum_{\mathrm{i}} \nu_{\mathrm{C,i}} \cdot J_{\mathrm{i}} \ . \quad (3)$$

Here F is the Faraday constant (96485 C·mol^{-1}), C_{m} is the membrane capacitance (F, or C·V^{-1}), and $\nu_{\mathrm{C,i}}$ is the stoichiometric coefficient of protons or sodium cations translocated out of the cytoplasm (negative if charges are translocated into the cytoplasm).

We calculate diffusive flux J_{j} according to the Fick's law and by taking *M. barkeri*

cell as a sphere of radius r(Fiksen et al., 2013),

$$J_j = 4\pi D_j r \left(C_{j,env} - C_{j,cyto} \right) \qquad (3)$$

where D_j is the diffusion coefficient ($dm^2 \cdot s^{-1}$), and $C_{j,env}$ and $C_{j,cyto}$ are the concentrations in the environment and the cytoplasm, respectively. We apply a generalized reversible Michaelis-Menten equation to calculate reaction flux J_i (Noor et al., 2013),

$$J_i = \rho_{prot} \cdot V_{cyto} \cdot k_i \cdot \phi_i \cdot \prod_A \frac{C_S / K_{m,S}}{1 + C_S / K_{m,S} + C_P / K_{m,P}} \cdot \left[1 - \exp\left(\frac{\Delta G_i}{\chi_i RT} \right) \right] , \quad (4)$$

where ρ_{prot} is the protein density, the mass of proteins per cell volume ($g \cdot L^{-1}$), k_i is the catalytic constant of enzyme i ($mol \cdot g^{-1} \cdot s^{-1}$), ϕ_i is the mass fraction of enzyme i in the proteome, C_S and C_P are the concentrations of substrate and product, respectively, $K_{m,S}$ and $K_{m,P}$ are the respective Michaelis constants, ΔG_i is the Gibbs free energy change of the reaction ($J \cdot mol^{-1}$), χ_i is the stoichiometric number of electrons transferred or charges translocated per reaction, R is the gas constant (8.3145 $J \cdot mol^{-1} \cdot K^{-1}$), and T is the temperature in kelvin. The free energy change is calculated according to

$$\Delta G_i = RT \ln\left(\frac{Q_i}{K_i} \right) + \nu_{C,i} F \Delta\psi \qquad , \qquad (5)$$

where Q_i is the quotient and K_i is the equilibrium constant of the reaction. We calculate the flux of the pseudo-biomass reaction and hence the specific growth rate from the flux difference between ATP production by ATP synthase and consumption by maintenance metabolism. In this way, the growth rate is determined by the net flux of ATP, which in turn depends on external methanol concentrations, a condition applicable to both laboratory bioreactors and natural environments.

2.2 Flux balance analysis

We estimate the stoichiometric coefficients of the pseudo-biomass reaction with flux balance analysis (FBA) (Heirendt et al., 2011). This method predicts steady-state flux distribution through metabolic networks from fitness objective, e.g., maximizing growth rates, under the stoichiometric constraints of metabolic reactions and within the permissible ranges of individual fluxes. We perform FBA with the updated iMG746 genome-scale metabolic model of M. barkeri (Benedict et al., 2012; Shapiro et al., 2018). We neglect the maintenance reaction because it has already been considered in the kinetic model. We drive FBA with methanol uptake flux as input and calculate the stoichiometry of the pseudo-biomass reaction from FBA output, in particular the specific growth rate and the fluxes of ATPs, reduced cofactor F420 and ferredoxin, and acetyl-coenzyme A out of the methanogenesis network. We also calculate protein yields from the growth rate and the exchange fluxes of methanol and methane.

2.3 Enzyme expression optimization

A unique feature of the kinetic model is that the model parameters include enzyme proteome fractions ϕ_i, which we estimate by optimization. We take the proteome fractions as decision variables and maximize specific growth rate μ,

$$\max \mu(\phi_i) \ . \qquad (6)$$

The optimization is subject to the ODEs of the metabolites and membrane potential (eqs 7, 8, and Dataset S1), and hence is a dynamic optimization problem. The optimization is further constrained by the allocation of finite cellular resources (fig 1b). First, the expressions of methanogenesis enzymes are limited by the proteome fraction ϕ_M partitioned to methanogenesis,

$$\sum_i \phi_i = \phi_M \ . \qquad (7)$$

Based on laboratory observations (see Dataset S1), we also assume that two thirds of ϕ_M are distributed to the enzymes in the cytoplasm, and the membrane-associated ones account for the rest. Second, the proteome fraction ϕ_i of the enzymes is constrained by the cost and benefit associated with ribosome allocation (Berkhout et al., 2013; G. W. Li et al., 2014).

2.4 Proteome partition

We estimate the proteome fraction ϕ_M of methanogenesis according to quantitative "growth laws" that relate proteome composition to growth rates (fig 1b). Following the coarse-grained model of *E. coli* (Hui et al., 2015; Mori et al., 2016a; Scott et al., 2010), we separate the methanogen proteome to a fixed sector Q, a sector of methanogenesis (M), and a growth-related sector that includes biosynthesis enzymes and ribosome-affiliated proteins (G). The proteome fractions of the M and G sectors (ϕ_M and ϕ_G, respectively) change with growth rate according to

$$\mu = k_G \cdot \phi_G \ , \qquad (8)$$

and

$$\mu = k_M \cdot \phi_M \ , \qquad (9)$$

but the total proteome fraction □max of the two sectors,

$$\phi_{max} = \phi_M + \phi_G \ , \quad (10)$$

does not change. Here k_G and k_M are the rate coefficients. These equations describe the tug-of-war between the M and G sector for the available proteome ϕ_{max}.

To maximize the growth rate, methanogens partition the proteome to the M sector

according to

$$\phi_M = \frac{k_G}{k_M + k_G} \cdot \phi_{max} \ . \qquad (11)$$

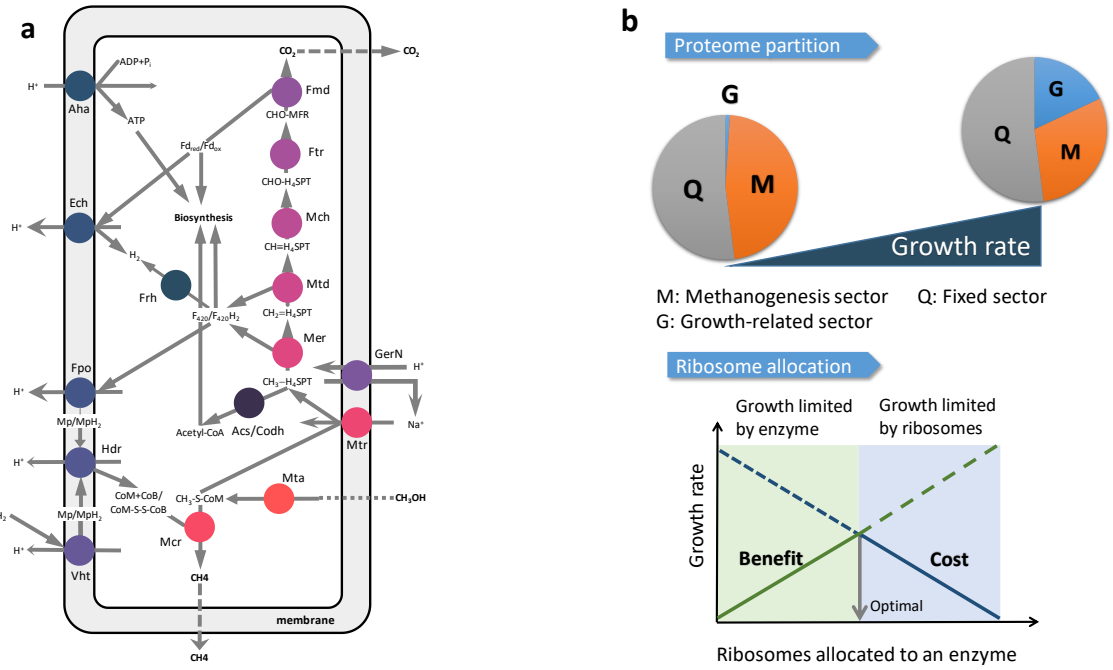

Figure 1. Modeling framework of M. barkeri growth. a. The kinetic model includes the enzyme reactions of methanogenesis and energy conservation, a maintenance reaction, and a pseudo-biomass reaction. Dashed and solid arrows indicate diffusion and biochemical reactions, respectively; circles represent enzymes; see Materials and Methods for abbreviations. b. Enzyme expressions are constrained by the relationships between proteome partitions and growth rates, and by the cost and benefit of ribosome allocation. The proteome is partitioned to three sectors, a fixed sector (Q) and two adjustable sectors – the methanogenesis and growth sector; the methanogenesis sector (M) includes enzymes of methanogenesis and energy conservation, and the growth sector (Q) contains biosynthesis enzymes, ribosomal proteins, and their affiliates. Increases in

the proteome fractions of the M and G sectors (ϕ_M and ϕ_G) increase growth rate, but the fractions of the two sectors add up to a constant, $1 - \phi_Q$. Ribosome allocation incurs both benefit and cost on growth rate. Dedicating more ribosomes to the synthesis of an enzyme increases growth rate (benefit), but lowers the ribosomes available for the remaining enzymes and proteins, which decreases growth.

At this fraction, the fluxes through the methanogenesis enzymes balance the fluxes of the enzymes in the G sector. We determine coefficient kG based on laboratory observations. In laboratory bioreactors, *M. barkeri* grows at ~1.0 d^{-1}, and the M sector accounts for ~30% of the proteome (see Dataset S1). Setting ϕ_{max} at 48%, the value determined for *E. coli* (Scott et al., 2010), gives a ϕ_G value of 18%. Substituting these values to equation 8 gives a k_G value of 5.3 d^{-1}. Coefficient k_M depends on both external methanol concentration and how the proteome fraction of the M sector is distributed to individual methanogenesis enzymes. Therefore, at a methanol concentration of acclimation and a given proteome fraction ϕ_M, we optimize individual methanogenesis enzymes to maximize the growth rate (eq 12), and calculate the kM value as the ratio of the maximized growth rate to the proteome fraction ϕ_M.

2.5 Ribosome allocation

We account for the cost and benefit of ribosome allocation by relating growth rates to the ribosomes committed to an enzyme (fig 1b) (Berkhout et al., 2013; G. W. Li et al., 2014). The fraction of the ribosomes allocated to the synthesis of an enzyme corresponds to the proteome fraction of the enzyme. On one hand, allocating more ribosomes increases the proteome fraction of the enzyme, which in turn tends to raise growth rates – the benefit of

ribosome allocation. The benefit depends on both the kinetics of methanogenesis enzymes and external methanol concentrations, but no analytical expression is available to relate the benefit to ribosome allocation (Berkhout et al., 2013). On the other hand, the cost is that fewer ribosomes are left for synthesizing the rest of the proteins, thereby lowering growth rate. In light of the linear dependence of growth rates on ribosomes (G. W. Li et al., 2014; Scott et al., 2010)., the function that accounts for the cost of ribosome allocation is

$$\mu = \mu_0 \left(1 - \frac{\phi_i}{\phi_{max}}\right), \qquad (12)$$

where μ_0 i is the hypothetical growth rate without accounting for the cost (Berkhout et al., 2013; G. W. Li et al., 2014).

According to equation 12, the highest cost of ribosome allocation comes from the most abundant enzyme, which is Mcr or Mta, depending on the methanol concentrations of acclimation. Therefore, at a given acclimation concentration, we build the benefit function by sweeping the proteome fraction of the most abundant enzyme. At each swept fraction, we optimize the remaining methanogenesis enzymes to maximize growth rate (eq 6). Parsimonious resource allocation requires that the benefit-enabled growth rate should not exceed the cost-adjusted rate (eq 12). Otherwise, ribosomes would be invested without raising growth rate, wasting cellular resources (fig 1b). The optimization solutions that balance the cost and benefit of ribosome allocation give the optimal fractions of the enzymes.

2.6 Nutrient acclimation

To simulate the growth of M. barkeri acclimating to a given methanol concentration, we build the kinetic model by optimizing the proteome fractions ϕ_i of the

enzymes. We take an iterative approach to account for the constraints of ribosome allocation and proteome partition. We start with a default M-sector fraction ϕ_{Mo} and build the benefit function of ribosome allocation by sweeping the proteome fraction of Mcr or Mta. The largest growth rate across the swept fractions represents the hypothetical growth rate μ_o obtained without accounting for the cost of ribosome allocation. By balancing the benefit with the cost of ribosome allocation, we optimize the enzyme proteome fractions that give the maximum growth rate μ_{op}.

We then balance the tug-of-war for the available proteome between the M and G sectors (eq 11). We calculate the rate coefficient k_M by substituting the maximum growth rate μ_{op} obtained at the default M-sector fraction ϕ_{Mo} to equation 9, and the optimal fraction $\phi_{M,op}$ of the M sector by substituting the k_M and k_G values to equation 11. We replace the default M-sector fraction ϕ_{Mo} with $\phi_{M,op}$ and repeat the above steps to solve for a new optimal fraction of the M sector. The repetition stops until the change in the optimal methanogenesis fractions between the two consecutive repetitions falls below a threshold of <0.1% of the proteome.

2.7 Model implementation and analysis

We implement and evaluate the kinetic models with the software COPASI (build 217) (57). We perform FBA using the COBRA Toolbox (Version 3.0) (Heirendt et al., 2011). We assume in the environment dissolved carbon dioxide at 20 mM and methane at 0.1 atm. We also assume methanol at 100 mM in laboratory bioreactors. Considering the homeostatic control of energy balance, we fix the concentrations of ATP, ADP, and inorganic phosphate in the cytoplasm. We also fix the ATP flux of the maintenance metabolism (Shapiro et al., 2018). We follow the method of control vector parameterization

and solve the dynamic optimization problem by splitting into an outer optimization problem and an inner initial value problem (Villaverde et al., 2016). The outer optimization problem searches for optimal enzyme levels, and is solved with the Nelder-Mead method – a simplex-based direct-search algorithm. The maximum iteration number, tolerance, and the relative size of initial simplex are set to 10^4, 10^{-10}, and 10, respectively. The inner initial value problem simulates the dynamics of methanogen growth, and is integrated forward for 10^6 s, well beyond the time of 10^3 s required for reaching steady state. Absolute and relative error tolerance were 10^{-8} and 10^{-6}, respectively. Because we focus on the growth of M. barkeri acclimating to different but constant methanol concentrations, we focus on steady-state solutions.

We calculate numerically the scaled control coefficient ε_i of enzyme i (eq 13) by changing the proteome fraction of the enzyme by 1%.

$$\varepsilon_i = \frac{\phi_i}{\mu} \cdot \frac{\partial \mu}{\partial \phi_i}, \quad (13)$$

To estimate growth kinetic parameters, we fit the simulated growth rates to the Monod equation by using the least square method. We quantify the error of the fitting with the mean squared error (MSE):

$$\sigma^2 = \frac{1}{n} \sum_{i=1}^{n} \left(\hat{\mu}_i - \mu_i \right)^2 , \quad (14)$$

where n is the number of data points, $\hat{\mu}_i$ is the fitted specific growth rate at methanol concentration i, and μ_i is the respective value from modeling results.

The kinetic model in SBML and COPASI formats, the MATLAB program for running FBA, and the least-square fitting program in Python are available from GitHub (https://github.com/geomicrobiology/Methanosarcina). The model components, including

the ODEs and initial concentrations of metabolites, the kinetic expressions of metabolic reactions, and respective thermodynamic and kinetic parameters, are available in Dataset S1 (xlsx).

2.8 Abbreviations

Enzymes. Aha, ATP synthase; Codh/Acs, carbon monoxide dehydrogenase/acetyl-CoA synthase, Ech, energy-converting ferredoxin-dependent hydrogenase; Fmd, formylmethanofuran dehydrogenase; Fpo, F420 dehydrogenase; Frh, F420-reducing hydrogenase; Ftr, formylmethanofuran-tetrahydromethanopterin N-formyltransferase; GerN, sodium/proton antiporter; Hdr, heterodisulfide reductase; Mch, methenyltetrahydromethanopterin cyclohydrolase; Mcr, methyl-coenzyme M reductase; Mer, 5,10-methylenetetrahydromethanopterin reductase; Mta, methanol:coenzyme M methyltransferase; Mtd, methylenetetrahydromethanopterin dehydrogenase; Mtr, methyl-H4SPT:coenzyme M methyltransferase; Vht, methanophenazine-dependent hydrogenase.

Metabolites. CoA, coenzyme A; CH3CO-CoA, acetyl-coenzyme A; CoB, coenzyme B; CoM, coenzyme M; CoB-CoM, mixed disulfide of CoB and CoM; F420/F420H2, oxidized and reduced cofactor F420, respectively; Fdox/Fdred, oxidized and reduced ferredoxin, respectively; Mp/MpH2, oxidized and reduced methanophenazine; CHO-MF, formyl-methanofuran; H4SPT, tetrahydrosarcinapterin; CHO-H4SPT, formyl-H4SPT; CH≡H4SPT, methenyl-H4SPT; CH2=H4SPT, methylene-H4SPT; CH3-H4SPT, methyl-H4SPT; CH3-CoM, methyl-coenzyme M.

3. Results

3.1 Kinetic Model of Methanogen Growth

We constructed a kinetic model to represent the growth of M. barkeri acclimating to a given methanol concentration. The model considers methanol diffusion from the environment to the cell and uses enzyme reactions to describe the stepwise processing of methanol to carbon dioxide and methane and concurrent chemiosmotic energy conservation (fig 1a). The model also includes an ATP hydrolysis reaction to represent the energy consumption by maintenance metabolism, and a pseudo-reaction of biomass synthesis that describes the mole numbers of ATPs, reduced cofactor F420 and ferredoxin, and acetyl-coenzyme A consumed by the production of 1 g protein (Millard et al., 2017). In total, the model contains 16 enzymes, 21 reactions, and 35 metabolites.

We estimate the stoichiometry of the pseudo-biomass reaction from the M. barkeri genome-scale metabolic model by performing FBA (Heirendt et al., 2011). This method allows us to couple the fluxes of the methanogenesis network to cell reproduction via the principle of mass balance. We compute fluxes of enzyme reactions according to the reversible Michaelis-Menten equation (Noor et al., 2013) and by taking the abundances and the catalytic constants of enzymes as model parameters. While most kinetic models favor maximum velocities V_{max}, i.e., the products of enzyme abundances and catalytic constants, the choice of catalytic constants is based on the observations that V_{max} values determined in vitro generally do not represent those in vivo (van Eunen et al., 2012; Teusink et al., 2000) and that significant correlation exists between the catalytic constants of *Escherichia coli* enzymes obtained *in vivo* and *in vitro* (Davidi et al., 2016). We sourced enzyme kinetic parameters from the literature. To the extent possible, we used the parameter values determined for the enzymes harvested from M. barkeri laboratory cultures at exponential

growth phase, and in assay media of 37 ℃ and neutral pH. Parameters not available in the literature were assigned based on the laboratory analyses of closely-related enzymes.

We optimize enzyme abundances and maximize growth rates under the constraints of proteome partition and ribosome allocation (fig 1b). The two constraints are universal in that they are experienced by all living cells. Specifically, the proteome constraint resembles the upper bound to cellular protein content given by the molecular crowding effect, a limitation on molecular machinery or available energy, or toxic effects resulting from protein synthesis (Berkhout et al., 2013; Mori et al., 2016b). The ribosome constraint arises from the well-known growth effect of gratuitous or nonfunctional proteins, that is the competition for ribosomes between gratuitous and functional proteins reduces growth rates (Dekel & Alon, 2005; G. W. Li et al., 2014). The optimization bridges external nutrient conditions and enzyme expressions under the principle of growth-rate maximization, and allows us to investigate how cellular resource allocation underlying nutrient acclimation influences the relationship between growth rates and external nutrient concentrations. Further details of the model construction are available in Materials and Methods.

3.2 Growth in Laboratory Bioreactors

To validate the modeling approach, we simulated the growth of *M. barkeri* in laboratory bioreactors and compared the modeling results to the independent experimental observations that had been excluded from the model construction. We first optimized the expression levels of the enzymes. In agreement with the enzyme assays using cell-free extracts (fig 2a and b), the results show that the enzyme expressions *in silico* are highly skewed: Mcr accounts for the largest mass fraction of the proteome, 11.5%, Mta comes in second with a proteome fraction of 4.9%, and the other enzymes have fractions <4.0%. Mcr

is the enzyme that produces methane in different methanogenesis pathways, whereas Mta is unique to the methylotrophic pathway by consuming methanol in the cytosol.

We then evaluated the model, and found that the results captured the metabolic state of the laboratory cultures. For example, the simulated membrane potential is 136 mV, close to the value of 130 mV determined experimentally (Blaut & Gottschalk, 1984). Out of the electron fluxes from the oxidation to the reduction of the methyl-group in methanol, 86% are carried by the production and consumption of H2, whereas cofactor F420 oxidation and reduction account for the remaining 14% (fig 2c), consistent with the dominant role of hydrogen cycling detected by laboratory experiments (Kulkarni et al., 2018). In addition, H2 and cofactor F420 share similar reduction potentials (fig 2c), which has been observed in laboratory studies (de Poorter et al., 2005). The model also reproduces two metabolic patterns documented by the metabolomic studies of Escherichia coli (Bennett et al., 2009; Park et al., 2016). First, the free energy is unevenly distributed among the metabolic reactions, ranging from –31 kJ·mol^{-1} to close to 0 (fig 2d). Second, 84% of the metabolites have concentrations greater than their respective Michaelis constants (fig 2e).

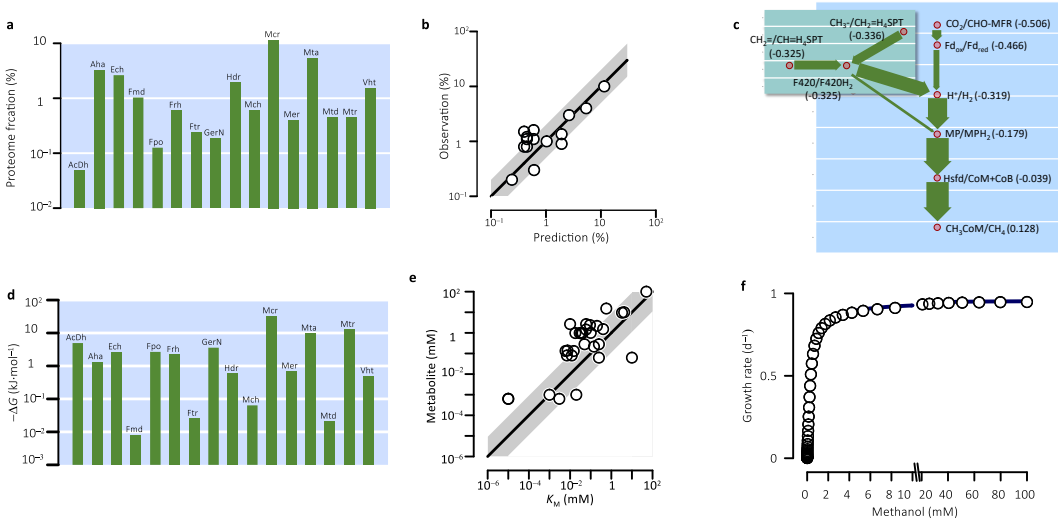

Figure 2. The kinetic model reproduces independent experimental observations of M. barkeri laboratory cultures. a. Optimized proteome fractions of enzymes. b. Optimized enzyme expressions are in agreement with those determined from in vitro cell-free lysates. Solid line shows the 1:1 ratio; shaded area covers up to 2-fold deviations from the 1:1 ratio. c. Electron fluxes from the oxidation to the reduction of the methyl-group in methanol. Values in parentheses show the reduction potentials (V); arrow widths indicate the magnitudes of the fluxes relative to the flux of the reduction of methyl-coenzyme M to methane (i.e., 1.74×10^{-18} mol·s^{-1}). d. Gibbs free energy ΔG is unevenly distributed among enzyme reactions. e. ~84% of metabolites have concentrations greater than the respective Michaelis constants K_M. Solid line shows the 1:1 ratio; shaded area covers up to tenfold deviations from the 1:1 ratio. e. Specific growth rates vary hyperbolically with external methanol concentrations. Data points are modeling results; solid line represents the results of the least-square fitting to the Monod equation; the mean square error of the fitting is 1.8×10^{-5}.

We characterized the growth kinetics of the laboratory cultures by evaluating the kinetic model with different external methanol concentrations. These simulations mimicked laboratory experiments for determining growth kinetic parameters – by inoculating microbes into fresh growth media of different nutrient concentrations and then immediately analyzing growth rates. The simulation results quantify how the laboratory cultures instantaneously respond to the changes in methanol concentrations, without re-allocating cellular resources. As shown in figure 2f, the growth rates vary with external methanol concentrations hyperbolically – the rates increase linearly at low methanol and approach maximum values at high methanol concentrations, and fit well to the Monod equation. The

best-fit maximum growth rate μ_{max} is 0.96±0.00 d^{-1}, the best-fit half-saturation constant K_M is 0.34±0.01 mM, and their ratio, μ_{max}/K_M, gives the methanol uptake affinity of $2.84\pm0.04\times10^3$ $M^{-1}\cdot d^{-1}$ (Button, 1998; Healey, 1980). These parameters constitute phenotypic traits that impact fitness, and have been frequently analyzed by laboratory experiments (Dataset S1). The laboratory-determined μ_{max} and K_M are 1.04±0.46 d^{-1} and 0.39±0.18 mM, respectively, in support of the modeling results. Combining these tests, we conclude that the modeling approach captured the experimental observations at different scales.

3.3 Growth at Different Nutrient Concentrations

To investigate the influence of cellular resource allocation on methanogen growth, we built kinetic models for M. barkeri acclimating to different methanol concentrations. We first accounted for methanol acclimations by optimizing the expression levels of the enzymes. According to the optimization results, methanol acclimations shift the proteomic composition of the methanogen (fig 3a and S1). From the acclimation concentration of 100 mM down to 1 μM, the proteome fraction partitioned to methanogenesis increases from ~30% to near 48%. Within the methanogenesis network, Mcr and Mta stand out by their relatively large proteome fractions. In addition, the proteome fractions of the two enzymes correlate strongly and negatively with each other (fig 3b).

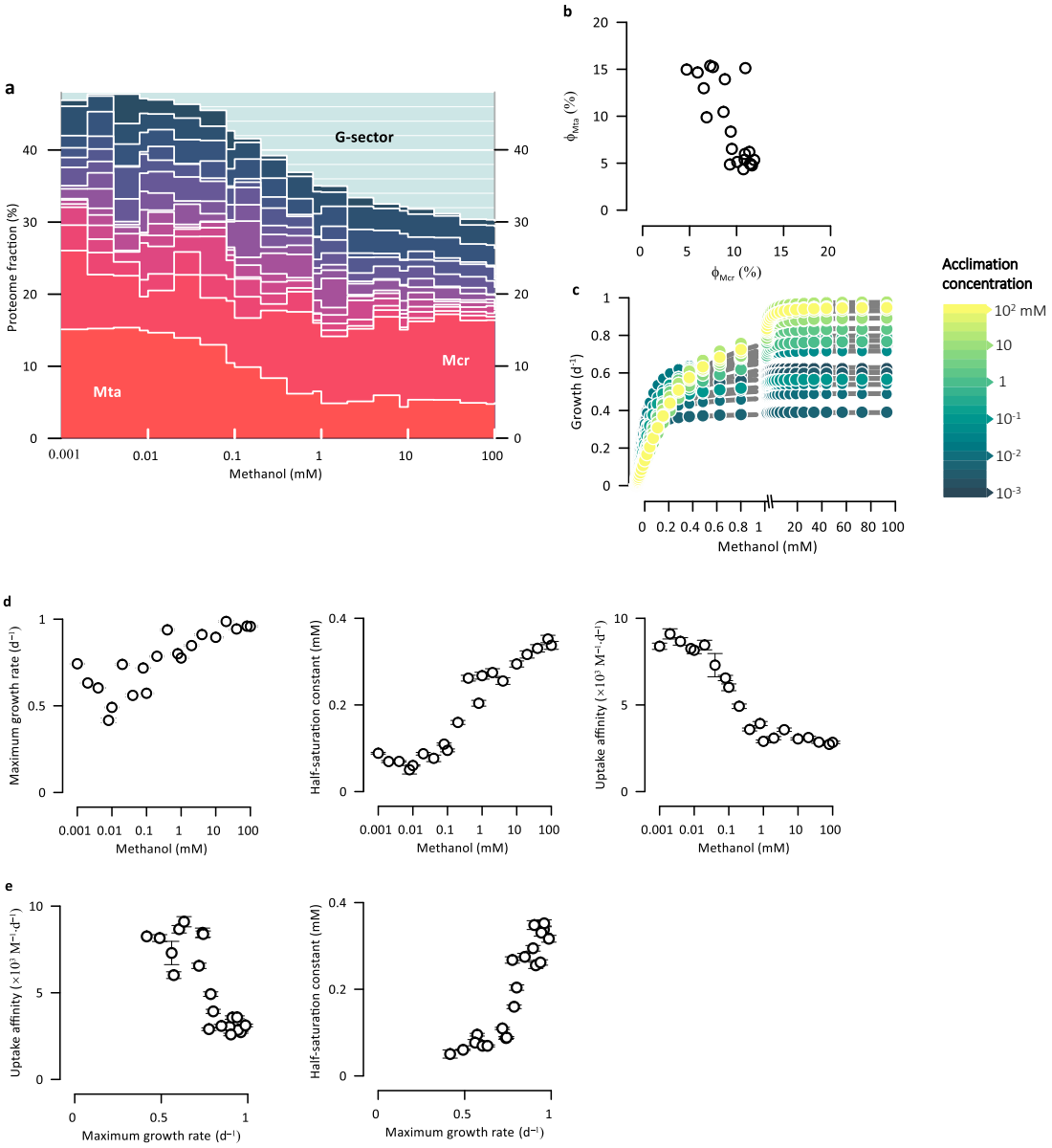

Figure 3. Growth of M. barkeri at different methanol concentrations. a. Optimal proteome fractions of enzymes at different methanol concentrations of acclimation. G-sector includes biosynthesis enzymes and ribosomal and ribosome-affiliated proteins; see fig 1a for color codes. b. Spearman's coefficient reveals statistically significant correlation between the proteome fractions of Mcr and Mta ($r_S[21] = -0.67$, $p<10^{-3}$). c. Instantaneous responses of growth rates to variations in external methanol concentrations without re-allocating cellular resources. Data points are the modeling results; lines are the best-fits to

the Monod equation; the mean square errors of the fittings are $<3.6\times10^{-3}$. d. Variations with methanol concentrations of acclimation in best-fit growth kinetic parameters. e. Spearman's coefficient reveals statistically significant correlation between best-fit maximum growth rates and uptake affinities ($r_S[19] = -0.78$, $p<10^{-3}$) and between maximum growth rates and half-saturation constants ($r_S[19] = 0.91$, $p<10^{-3}$). Error bars indicate standard deviations; those smaller than symbols are not shown.

To characterize the kinetics of methanogen growth, we applied the kinetic models and simulated how M. barkeri, having acclimated to a given methanol concentration, instantaneously responds to the changes in methanol concentrations. Regardless of the acclimation concentrations, the rate responses fit well to Monod's hyperbolic relationship (eq 1, fig 3c and S2). The best-fit maximum growth rates μ_{max} and the half-saturation constants K_M acquire different values at various acclimation concentrations, and so do the methanol uptake affinities α, highlighting the plasticity of the phenotypic traits (fig 3d). Furthermore, as shown in figure 3e, the maximum growth rates correlate negatively with the uptake affinities, and positively with the half-saturation constants. By acclimating to >10 mM methanol, *M. barkeri* acquires relatively large μ_{max} and K_M but small α values, a behavior referred to by ecologists as *r* strategy (Fredrickson & Stephanopoulos, 1981; Kilham & Hecky, 1988). By acclimating to <0.01 mM methanol, the methanogen obtains small μ_{max} and K_M but large α, the properties of *K* strategists. Therefore, the trait plasticity is characterized by the trade-off between the maximum growth rates and the uptake affinities, and confers to the methanogen a continuum of *r* to *K* strategies.

We note that both Monod's hyperbolic relationship and the trait trade-off arise directly from the model solutions, without any ad hoc constraint on the growth rates, and

hence represent emergent properties of methanogen growth. These emergent properties suggest that cellular resource allocation does not alter the kinetic expression of methanogen growth, but it does change the growth kinetic parameters, giving rise to the trait plasticity and trade-off. Accordingly, by taking the kinetic parameters as input, the Monod equation does not account for cellular resource allocation, and hence is best applied to short-term kinetic responses of microbial growth, before cellular resources are re-allocated. In addition, because of the parameter trade-off, methanogens may not limit themselves to r- or K-strategy, but can adopt the r/K continuum to gain competitive advantage across different methanol concentrations. In this respect, the trait trade-off reflects the adaptive capacity of methanogens to the surrounding environment, and distinguishes methanogen growth from inanimate systems.

Although few field or laboratory observations of M. barkeri are available for comparison, the modeling results are consistent with experimental studies of other microbes. Specifically, the proteome shift agrees with patterns of the proteome partition of *E. coli*, that is, more proteins are allocated to catabolic enzymes at smaller growth rates (Hui et al., 2015; Scott et al., 2010). At the enzyme level, Mta affects the diffusive uptake of methanol from the environment by consuming methanol in the cytosol. Therefore, the high Mta levels at low methanol concentrations are consistent with the reports that in response to nutrient limitations, microbes upregulate nutrient permeases and transporters (Ferenci, 1999; Risso et al., 2008). Moreover, the trait plasticity resonates with the emerging consensus that microbial kinetic parameters do not behave as true biological constants (Ferenci, 1999; Jin et al., 2013b). Correlations between maximum growth rates and half-saturation constants have also been detected for E. coli (Kovárová-Kovar & Egli,

1998), methane-oxidizing prokaryotes (Dunfield & Conrad, 2000), and phytoplanktons (Litchman et al., 2007).

Finally, the trait plasticity echoes the need of in situ kinetic parameters for applying the Monod equation (Jin et al., 2013a). For example, in the deltaic surface sediments of the Western Mediterranean Sea, methanol-driven methanogenesis contributes to >90% of methane bioproduction, but methanol concentrations occur at ~1 μM (Zhuang et al., 2018). By using kinetic parameters estimated for methanogens acclimating to 1 μM methanol, we predict a growth rate of 8.3×10^{-3} per day. By approximating the methanogen abundance at 10^4 cell per cm^3 sediments (Pancost et al., 2000), we also predict a methanogenesis rate of 1.4×10^{-11} $mol\cdot cm^{-3}\cdot d^{-1}$, close to the upper range of 2.0×10^{-11} $mol\cdot cm^{-3}\cdot d^{-1}$ determined with the ^{14}C-labelled method (Zhuang et al., 2018). However, if we used the parameters of laboratory cultures, we would predict a growth rate of 1.8×10^{-3} per day and a methanogenesis rate of 3.0×10^{-12} $mol\cdot cm^{-3}\cdot d^{-1}$, nearly an order of magnitude smaller than the field observations.

3.4 Metabolic Control Analysis

To account for the kinetic influence of cellular resource allocation, we analyze the kinetic models with metabolic control analysis (MCA) – a quantitative framework for probing the control by enzymes on fluxes through a metabolic network (Kacser et al., 1995). According to MCA theory, the control exerted by enzyme i on growth rate can be quantified with a scaled control coefficient ε_i. The fractional change in growth rate by a fractional change in the mass fraction ϕ_i of the enzyme in the proteome. A control coefficient near 0 applies to enzymes of little impact, whereas an enzyme with a value near 1 is influential in controlling the growth rate. Within a network, the coefficients of the

different enzymes add up to unity -the summation theorem of MCA (Kacser et al., 1995).

The MCA results suggest that Mcr and Mta are the two enzymes that significantly control the growth rates at high and low methanol concentrations, respectively. Figure 4a shows the control coefficients of Mcr and Mta across different external methanol concentrations. Regardless of the acclimation concentrations, the control coefficients of Mcr and Mta approach unity at >10 mM and <0.01 mM methanol, respectively. In-between 0.01 and 10 mM methanol, the coefficients of Mcr and Mta vary from close to 0 to near 1 and in opposite directions, and that their sums stay close to unity. In contrast, the rest of the enzymes have control coefficients <0.1 (fig S3).

From the MCA results appear another set of emergent metabolic properties. First, the near-unity coefficients suggest that the growth rates can be expressed in terms of the proteome fractions of Mcr and Mta (fig S4 and Supplementary Text). At >10 mM methanol, both the growth rates and Mcr reaction velocities approach their respective maxima, and the two maxima can be related to each other via the protein yield $Y_{P/CH4}$ per methane ($g \cdot mol^{-1}$),

$$\mu_{max} = Y_{P/CH4} \cdot k_{Mcr,app} \cdot \phi_{Mcr} . \qquad (15)$$

Here $k_{Mcr,app}$ and ϕ_{Mcr} are the apparent catalytic constant ($mol \cdot g^{-1} \cdot s^{-1}$) and the proteome fraction of Mcr, respectively, and their product gives the maximum velocity. At <0.01 mM methanol, both the growth rates and the Mta velocities increase linearly with methanol concentrations. The slopes of the velocity increases, combining with the protein yield $Y_{P/CH3OH}$ per methanol, determine the slopes of the growth rate increase, i.e., the methanol uptake affinities α (Button, 1998; Healey, 1980),

$$\alpha = Y_{\mathrm{P/CH3OH}} \cdot \frac{k_{\mathrm{Mta,app}} \cdot \phi_{\mathrm{Mta}}}{K_{\mathrm{m,CH3OH}}} \quad . \qquad (16)$$

Here $k_{\mathrm{Mta,app}}$ is the apparent catalytic constant, and $K_{\mathrm{m,CH3OH}}$ is the Michaelis constant of Mta for methanol (Molal). The product of $k_{\mathrm{Mta,app}}$ and the proteome fraction ϕ_{Mta} gives the maximum velocity, and the ratio of the maximum velocity to $K_{\mathrm{m,CH3OH}}$ defines the catalytic efficiency or specificity of Mta ($\mathrm{L \cdot g^{-1} \cdot s^{-1}}$) (Northrop, 1998). Equation 3 and 4 reveal that the maximum growth rate $\mu_{\max}$ and the uptake affinity α vary linearly with the expression levels of Mcr and Mta, respectively. Accordingly, the ratio of $\mu_{\max}$ to α, or the half-saturation constant, depends linearly on the expression ratios of Mcr to Mta. These relationships are supported by the correlation analyses between the best-fit kinetic parameters and the optimized enzyme levels shown in figure 4b.

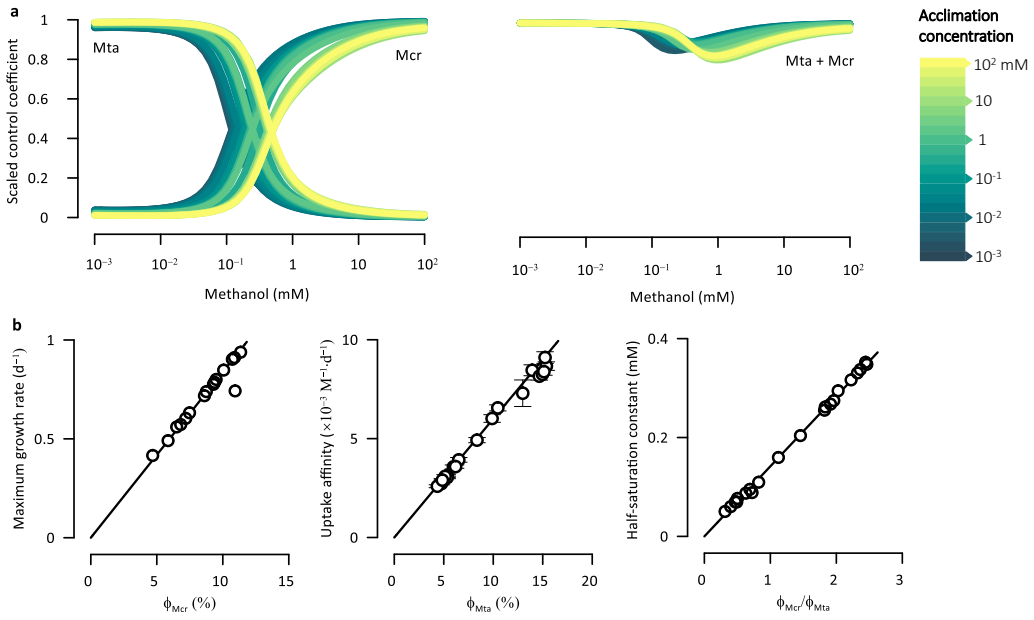

Figure 4**.** Metabolic control analysis (MCA) connects growth kinetics to enzyme expressions. **a.** Variations with ambient methanol concentrations in scaled control coefficients of Mcr and Mta and their sum. Lines are the results of performing MCA with

the kinetic models constructed for different methanol concentrations of acclimation. **b.** Pearson's correlation coefficients reveal statistically significant correlation between best-fit maximum growth rate and optimal proteome fraction of Mcr, between uptake affinity and proteome fraction of Mta, and between half-saturation constant and the proteome fraction ratio of Mcr to Mta. Error bars indicate standard deviations, and those smaller than symbols are not shown; lines are best-fit linear regressions.

From these results, we observe how cellular resource allocation influences the kinetics of methanogen growth. First, cellular resource allocation controls enzyme expressions, including those of Mcr and Mta, and thereby determines maximum growth rates and nutrient uptake affinities. Across the different methanol acclimations, cellular resource allocation shifts the proteome composition and changes the expression levels of Mcr and Mta, giving rise to the plasticity of the growth kinetic parameters. Second, cellular resource allocation does not alter Monod's hyperbolic relationship. According to the derivation, the hyperbolic relationship arises as a logical outcome of a bimodal control pattern – the growth rates are controlled by two different enzymes at high and low methanol concentrations, respectively. Despite the significant proteome shift, Mcr and Mta always remain as the enzymes of prominent growth-rate control. The control by Mcr at high methanol concentrations is consistent with Mcr being the methanogenesis enzyme of the lowest catalytic rate constant (Dataset S1). The control by Mta occurs where its velocity is limited significantly at low methanol concentrations. Similar bimodal control pattern has been noted for microbial growth on other nutrients, such as glucose and acetate (Bakker et al., 1999; Risso et al., 2008). The parameter plasticity has been observed from other microbes (e.g., (Dunfield & Conrad, 2000; Kovárová-Kovar & Egli, 1998; Litchman et al.,

2007).

3.5 Trait Plasticity

Having linked trait plasticity to enzyme expressions, we are curious about how the pragmatic principles of optimal resource allocation govern enzyme expressions and thereby shape the trade-off of growth kinetic parameters. First, a key factor underlying enzyme expression is the strength of the growth-rate control by enzymes □ more proteins are allocated to the enzymes that exert stronger control. Figure 5a compares the optimal proteome fractions and the scaled control coefficients of the enzymes computed at the methanol concentrations of the acclimation. Strong positive correlations appear between the abundances and the control coefficients of Mta and Mcr. For the rest of the enzymes, whose control coefficients remain <0.1, their proteome fractions correlate weakly with the control coefficients. These results support the theory that in order to maximize growth rates, microbes mitigate the strong control of enzymes by upregulating the expressions of the enzymes (Heinrich et al., 1991; Klipp & Heinrich, 1999). Specifically, in response to the shift in the growth control, Mcr and Mta are upregulated at high and low methanol concentrations, respectively.

Surprisingly, neither Mcr nor Mta accounts for more than half of the proteins allocated to methanogenesis (fig 3a). Why does M. barkeri not express more Mcr or Mta proteins? This is because enzyme expressions requires ribosomes and therefore are subject to the trade-off between the cost and benefit of ribosome allocation (fig 1b) (Berkhout et al., 2013; G. W. Li et al., 2014). For example, at >10 mM methanol, allocating more ribosomes to Mcr synthesis raises the expression level and mitigates the growth control of the enzyme, raising the rates of growth. But the consequence is that fewer ribosomes are

left for the production of other proteins, reducing growth rates. Figure 5b demonstrates the trade-off arising from the cost and benefit of synthesizing Mcr on growth rates. By optimizing the trade-offs, at >10 mM methanol, the fastest growth is achieved where Mcr accounts for ~11% of the proteome. Likewise, at methanol <0.01 mM, the growth rate is maximized where Mta is expressed at ~15% of the methanogenesis proteins (fig 5c).

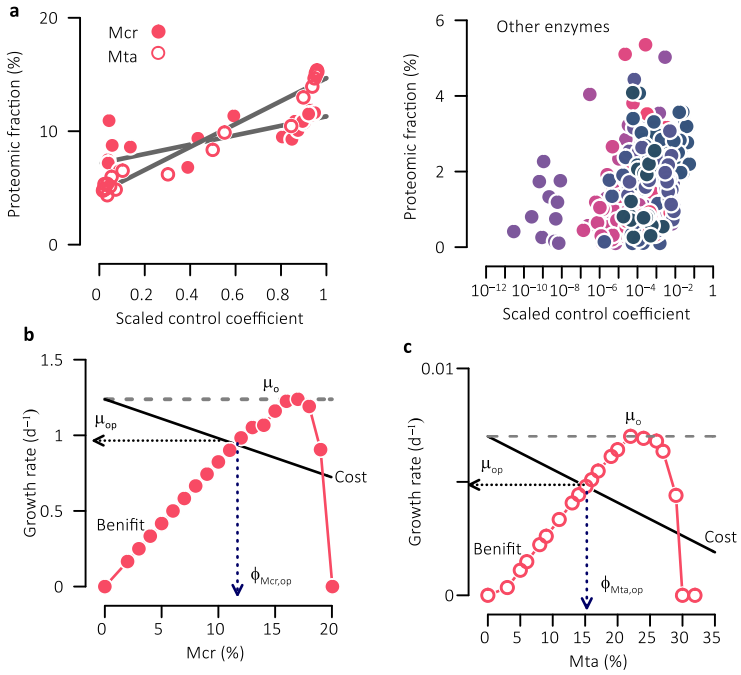

Figure 5**.** Constraints of proteome partition and ribosome allocation on enzyme expressions. **a.** Spearman's coefficients reveal statistically significant correlations between the optimal proteome fractions and scaled control coefficients of Mcr, Mta, and the rest enzymes. See fig 1a for color code. **b.** Trade-off between the cost and benefit of ribosome allocation at 100 mM methanol of acclimation. The benefit function is constructed by sweeping the proteome fraction of Mcr and then optimizing the rest enzymes. The cost function is calculated according to equation 18. $\mu_{Mcr,op}$ is the optimal proteome fraction of Mcr that balances the cost and benefit of ribosome allocation; μ_{op} and μ_o represent the optimal growth rates with and without balancing the cost and benefit,

respectively; **c.** Trade-off between the cost and benefit of allocating ribosomes to the synthesis of Mta at 1 μM methanol of acclimation. $\mu_{Mta,op}$ is the optimal proteome fraction of Mta.

The expressions of Mcr and Mta are also constrained by the proteome partitioned to methanogenesis, giving rise to the negative correlation between maximum growth rates and uptake affinities. The trait trade-off has been attributed to allometry or the differential investment of cellular resources between ribosomes and nutrient uptake (Litchman et al., 2007). Our results connect the two parameters to Mcr and Mta and therefore offer an alternative explanation. In particular, the expressions of the two enzymes are in a tug-of-war for the proteins allocated to methanogenesis. Upregulating Mta expression downregulates the expression of Mcr, and vice versa. Moreover, the proteome partition varies with the acclimation concentrations of methanol (fig 3a). Greater proteome fractions for methanogenesis at lower methanol concentrations coincide with the upregulation of Mta expressions, leading to about an order of magnitude variation in Mta abundances and hence in the uptake affinity of methanol. In contrast, Mcr expression is upregulated at high methanol concentrations, where the proteome fractions of methanogenesis are small. Therefore, Mcr abundances and the maximum growth rates vary only by a factor of 2 (fig 3b).

4. Discussion

Microbes in the environment of limited energy resources are under selection pressure to optimize their resource allocation. However, it is not clear how cellular resource allocation influences the kinetics of microbial growth. This question is critical for addressing current environmental challenges, from contaminant remediation to greenhouse

gas emissions. Here we addressed this question by constructing and analyzing kinetic growth models for M. barkeri acclimating to different methanol concentrations. Our modeling framework integrates kinetic metabolic modeling with flux balance analysis and dynamic optimization, and is based on the fact that biomass synthesis requires not only the supplies of ATPs, reducing equivalents, and metabolic precursors, but also the allocation of proteins and ribosomes. The new modeling approach predicts growth rates from nutrient concentrations and simulates emergent properties arising from the kinetics of methanogenesis enzymes, the stoichiometry of genome-scale metabolic reactions, and proteome-wide resource allocation.

The emergent properties obtained from the simulations allowed us to derive the Monod equation ab initio and to link macroscopic kinetic parameters to the expressions and kinetics of methanogenesis enzymes. Specifically, the dependence of growth kinetic parameters on enzyme expressions limits the equation application to short-term growth responses to changing nutrient concentrations. To apply to microbes that have acclimated to different nutrient conditions, the Monod equation should be combined with models that account for the plasticity and trade-off of microbial kinetic parameters – a growing trend in trait-based ecosystem modeling (Smith et al., 2014). The simulation result supports the maximum growth rate and nutrient uptake affinity as the primary growth kinetic parameters – the two parameters reflect the properties of two rate-controlling enzymes under high and low nutrient concentrations. In contrast, by relating to the expression ratio of the two rate-controlling enzymes, the half-saturation constant does not directly measure the competitive ability of microbes at low nutrient conditions, but reflects the tug-of-war in proteome partition and therefore the trade-off between the maximum growth rates and nutrient uptake

affinities.

In addition, our results also allowed us to suggest the r-K strategy continuum as an outcome of optimal resource allocation. Traditionally, microbes have been classified into r- or K-strategists according to their growth kinetics (Fredrickson & Stephanopoulos, 1981; Kilham & Hecky, 1988). In our growth models, the r-K strategy continuum arises from optimal resource allocation under the constraints of proteome partition and ribosome allocation. Because these constraints are experienced by all living cells and universal, the r-K continuum may not be unique to methanogens, but a strategy of prokaryotes in general. This hypothesis resonates with the emerging consensus about the pivotal role of cellular resource allocation in cell metabolism and physiology. In particular, optimal resource allocation has been recognized as a unifying principle underlying distinct metabolic strategies across nutrient regimes, including diauxic growth that switches between carbon sources and the metabolic shift from respiration to fermentation (Molenaar et al., 2009). The hypothesis adds that, within a metabolic pathway, optimal resource allocation equips microbes with the r-K continuum, another strategy for maximizing fitness over different nutrient conditions.

The results also open new opportunities for investigating microbial kinetics in natural environments. For example, microbial kinetics in soils and sediments has thus far resisted traditional experimental interrogation, due to the technical difficulties in differentiating metabolically-active cells from dormant or dead ones and microbial activities from bulk chemical fluxes. The mechanistic links between microbial kinetic parameters and enzyme properties demonstrate the feasibility of enzyme abundances or the expression levels of target genes as proxies for in situ microbial kinetic parameters

(Holmes et al., 2013; Wilkins et al., 2011). Specifically, in light of the linear relationships between parameter values and enzyme expressions, we propose to extrapolate laboratory determined parameter values to the environment by comparing expression levels of Mcr and Mta of natural methanogens to those of laboratory cultures. As another example, metabolic scaling laws, originally developed for metabolic activities of macro- fauna and flora across temperatures (Brown et al., 2004), might also be applicable to methanogens and other prokaryotes. Where nutrients are either abundant as in bioreactors or scarce as in oligotrophic environments, methanogen growth is controlled predominantly by single enzymes in a methanogenesis network (e.g., Mcr or Mta). Because the temperature response of enzyme kinetics follows the Arrhenius equation, the growth rate in the two opposite nutrient regimes should also follow the Arrhenius equation, a foundation for the development of metabolic scaling laws (Brown et al., 2004).

In summary, we fill the gap between metabolic modeling and microbial kinetics, we found the trade-off of resource allocation and kinetic parameters with substrate ranging from relative low to high concentrations. We have focused on M. barkeri, but the approach outlined in this study should be applicable to other microbes. By doing so, we hope to improve applications of the Monod equation and to move microbial kinetics beyond empirical equations by building models tailored for environmental and ecosystem applications while still grounded in fundamental biochemical pathways and metabolic principles.

CHAPTER III PHYSIOLOGICAL ACCLIMATION AND THE METHANOGENESIS KINETICS IN NATURAL ENVIRONMENTS

1. Introduction

Methane is a potent greenhouse gas, accounting for 4–9% of the Earth's greenhouse effect (Lashof & Ahujah, n.d.). Every year, microbes output a total of 1 billion metric tons of methane, directly contributing to the steady accumulation of atmospheric methane in the recent 200 years (Nisbet et al., 2016; Schaefer et al., 2016). To understand atmospheric methane dynamics and to forecast future climate, a key question is how fast methanogenesis proceeds in natural environments.

Current models describe microbes as an autocatalyst (Bethke, 2008). They calculate methane production rate r by using a generalized Monod equation,

$$r = k \cdot \frac{C_S}{K_M + C_S} F_T, \qquad (1)$$

and couple methanogenesis to microbial growth according to,

$$\frac{dC_X}{dt} = Y_X r \left(1 - \frac{C_X}{K_X}\right) C_X - DC_X .. \qquad (2)$$

Here k is the rate constant ($mol \cdot g^{-1} \cdot s^{-1}$), the methanogenesis rate per unit biomass where substrate concentration C_S (molal or M) is much larger than the half-saturation constant K_M (M), and where F_T, the dimensionless factor accounting for methanogenesis thermodynamics, reaches unity, C_X is the biomass concentration ($g \cdot L^{-1}$), Y_X is the biomass yield per methane ($g \cdot mol^{-1}$), K_X is the carrying capacity, or the maximum biomass concentrations supported by the environment ($g \cdot L^{-1}$), and D is the maintenance rate (s^{-1}).

These parameters have been analyzed for laboratory methanogen cultures (Conklin et al., 2006; Min & Zinder, 1989), but in natural environments, microbes have escaped traditional kinetic analysis, due to the technical challenges in enumerating live cells of interest and in determining low chemical fluxes with acceptable accuracy.

A point of controversy is how to predict methanogenesis rates in natural environments. Current predictions are obtained by evaluating the autocatalytic model (eqs 1 and 2) with the parameters of laboratory cultures. However, natural methanogens tend to have kinetic properties differ notably from those of laboratory cultures. Taking as an example the pathway that dismutates acetate to methane and carbon dioxide,

$$\text{Acetate} + H^+ \rightleftarrows CH_4 + CO_2 \text{,} \quad (3)$$

the half-saturation constants determined for methanogens in natural sediments are <0.05 mM, but those obtained for laboratory cultures are above 0.5 mM (Derek R Lovley & Klug, 1986; Roden & Wetzel, 2003). Different kinetic properties have also been reported between laboratory cultures and natural microbes of sulfate reduction, iron reduction, and other processes (Jin et al., 2013a; Pallud & Van Cappellen, 2006). For this reason, direct application of the autocatalytic model to natural environments has led to predictions that deviated by orders of magnitude from field observations (Jin et al., 2013a).

Another point of debate is the contradiction between the constant kinetic parameters employed by the autocatalytic model and the parameter plasticity associated with physiological acclimation. Acclimation refers to reversible changes in phenotypic traits induced by the changes in environmental conditions. Well-known examples include the variations of microbial kinetic parameters with pH and temperature (Jin & Kirk, 2018; Rosso et al., 1995). Likewise, kinetic parameters also vary with substrate concentrations

(Friedrich et al., 2015; Litchman et al., 2015). Such variations can arise from active metabolic regulations or occur as an automatic outcome of physicochemical principles, and provide microbes with fitness across different environmental conditions (Leroi et al., 1994). From this perspective, microbes are also a self-adapting catalyst, capable of modulating their kinetic parameters.

Here we predict methanogenesis rates by developing a model that describes microbial acclimation to the substrate and thermodynamic conditions of the environment. We focus on acetoclastic methanogenesis (eq 3), a pathway that accounts for two thirds of the global methane bioproduction (Prakash et al., 2019). This pathway is catalyzed by two genera, *Methanosarcina* and *Methanosaeta*, that show distinct niche preferences. *Methanosarcina* dominates the pathway in the environment with relatively high acetate concentrations, whereas *Methanosaeta* takes over under low acetate conditions (Conklin et al., 2006; Min & Zinder, 1989; K. S. Smith & Ingram-Smith, 2007). Our results show that the autocatalytic model alone is not sufficient for predicting methanogenesis rates or the niche separation, but the predictions can be improved by the acclimation model we constructed here.

2. Acclimation model

We assume that microbes gain competitive fitness by maximizing the production rate of adenosine triphosphate (ATP). This assumption recognizes that ATP is the universal energy currency of life and is required by growth, maintenance, and other metabolic processes (Nirody et al., 2020). ATP production rate depends on both the ATP yield Y_P per methane and the rate of methanogenesis. We first consider how methanogenesis rate is controlled by the allocation of intracellular resources, such as proteins, ribosomes, and

other macromolecules (fig 1A).

Pahlow (2005) and Smith and Yamanaka (2007) developed an acclimation model to describe nutrient uptake kinetics and its dependence on ambient nutrient concentrations. Following their methodology, we assume that:

The rate constant reflects methanogenesis rates at very high substrate concentrations and is determined by the cellular resources allocated to methanogenesis pathway.

The ratio of the rate constant to the half-saturation constant, i.e., the specific affinity α, reflect methanogenesis rates at very low substrate concentrations (Healey, 1980) , and is determined by the cellular resources allocated to substrate transport from the environment to the cytoplasm.

Methanogens maximize methanogenesis rate by optimizing the partition of cellular resources between methanogenesis and substrate transport.

From these assumptions, we formulate an optimization problem that maximizes the rate of methanogenesis by partitioning the resources between acetate transport and methanogenesis (see Data Repository). Solving the optimization problem gives the kinetic parameters (i.e., k_a, α_a, and $K_{M,a}$) of methanogens that acclimate to acetate concentration C_{Ac},

$$k_a = k_o \frac{K_{M,o} + C_{Ac,o}}{C_{Ac,o} + K_{M,o} C_{Ac,o}^{\frac{1}{2}} C_{Ac}^{-\frac{1}{2}}}, \quad (4)$$

$$\alpha_a = \frac{k_o}{K_{M,o}} \frac{K_{M,o} + C_{Ac,o}}{K_{M,o} + C_{Ac,o}^{\frac{1}{2}} C_{Ac}^{\frac{1}{2}}}, \quad (5)$$

and

$$K_{M,a} = K_{M,o} C_{Ac,o}^{-\frac{1}{2}} C_{Ac}^{\frac{1}{2}}. \quad (6)$$

Here k_o and $K_{M,o}$ are the parameters determined for laboratory cultures, and $C_{Ac,o}$ is the acetate concentration in laboratory growth media (i.e., 50 mM). According to equation 4 to 6, compared to laboratory cultures, methanogens acclimating to low acetate concentrations acquire smaller rate constants, smaller half-saturation constants, but larger specific affinities, because more cellular resources are allocated to acetate uptake than to methanogenesis.

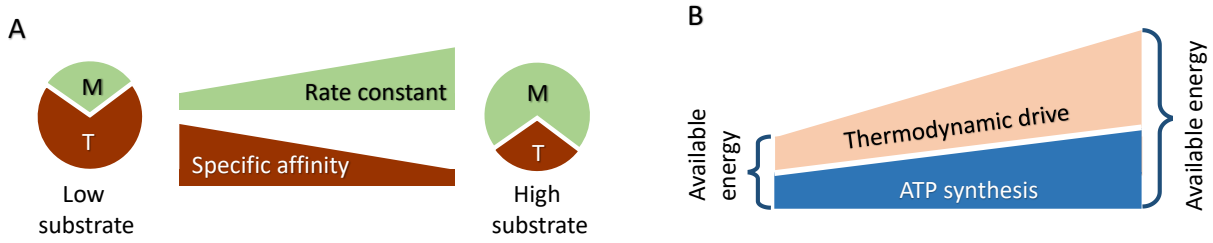

Figure 1. Physiological acclimation model. (A) Methanogens acclimate to substrate concentrations by allocating intracellular resources between methanogenesis (M) and substrate transport (T), leading to large rate constants at high substrate concentrations and large specific affinities at low concentrations. (B) They also acclimate to the energy available in the environment by partitioning the energy between ATP synthesis and thermodynamic drive of methanogenesis, raising ATP yield with increasing available energy.

We then consider the trade-off between the rate and the ATP yield (fig 1B, Pfeiffer et al., 2001). By catalyzing methanogenesis, microbes release the chemical energy in the environment and conserve a part of the released energy by synthesizing ATP. The difference between the released and the conserved energy gives the thermodynamic drive f for methanogenesis,

$$f = \Delta G_A - Y_P \Delta G_P . \quad (7)$$

Here ΔG_A is the energy available in the environment – the negative of the Gibbs free energy change of methanogenesis reaction ($J \cdot mol^{-1}$), ΔG_P is the energy consumed by ATP synthesis from adenosine diphosphate and phosphate in the cytoplasm, and its value is 45 $kJ \cdot mol^{-1}$ (Jin, 2012). At a given available energy, increases in ATP yield lower the thermodynamic drive and hence methanogenesis rate. Such trade-off can be captured by using the thermodynamic potential factor (Jin et al., 2013a),

$$F_T = 1 - \exp\left(-\frac{f}{\chi RT}\right), \quad (8)$$

where χ is the average stoichiometric number and its value is 2 per methane, R is the gas constant ($J \cdot mol^{-1} \cdot K^{-1}$), and T is the absolute temperature.

We formulate another optimization problem by assuming that microbes adjust ATP yields in order to maximize ATP production rates (see Data Repository). The solution to this problem relates the ATP yield to the energy available in the environment,

$$Y_P = \alpha \cdot \Delta G_A^{\beta} . \quad (9)$$

Here coefficient and exponent are 4.2×10□6 and 1.1, respectively. To ensure that the ATP yield predictions are biochemically feasible, we assume that the predicted YP values do not exceed those of laboratory cultures. The ATP yield gives the biomass yield YX (eq 2) according to

$$Y_X = Y_{X/P} \cdot Y_P . . \quad (10)$$

Here $Y_{X/P}$ is the biomass yield per ATP and its value is 5 $g \cdot mol^{-1}$ (Jin, 2012).

3. Results

3.1 Laboratory Observations

We compiled the kinetic parameters determined for the laboratory cultures of mesophilic *Methanosarcina* and *Methanosaeta* (fig 2). The results show that *Methanosarcina* has a rate constant of $2.3\pm0.5\times10^{-6}$ mol·g^{-1}·s^{-1}, a half-saturation constant of 4.4±1.2 mM, and a growth yield of 2.3±0.5 g·mol^{-1}, while for *Methanosaeta*, these values are $6.4\pm3.5\times10^{-7}$ mol·g^{-1}·s^{-1}, 0.8±0.3 mM, and 1.3±0.1 g·mol^{-1}, respectively. From these results, we calculated that *Methanosarcina* and *Methanosaeta* have a specific affinity of $5.1\pm0.9\times10^{-4}$ and $8.0\pm2.2\times10^{-4}$ L·g^{-1}·s^{-1}, and an ATP yield of 0.46±0.10 and 0.27±0.02 per methane, respectively. These results confirm the kinetic differences between the two methanogens (Conklin et al., 2006; Min & Zinder, 1989), and provide the foundation for applying the acclimation model.

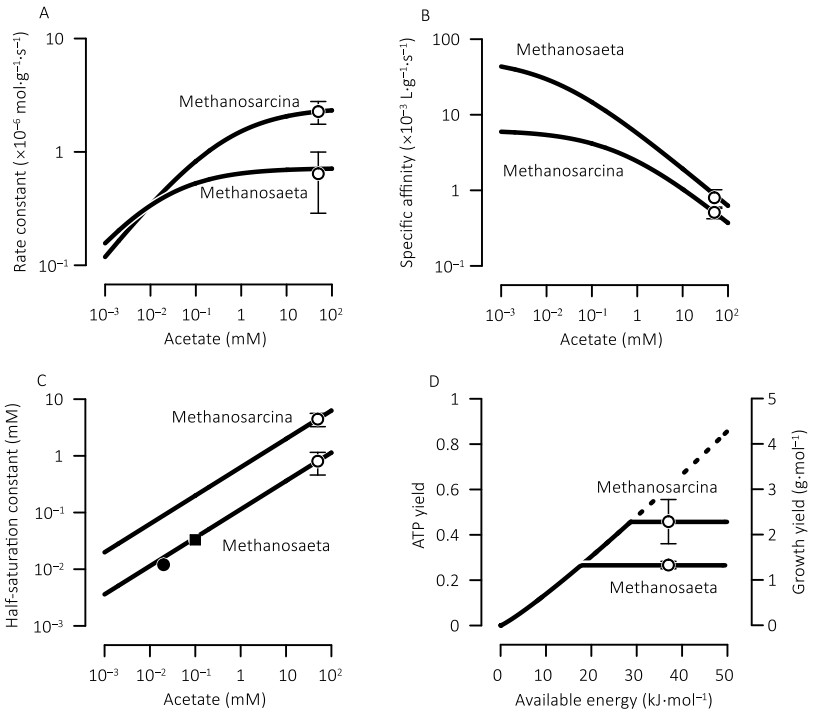

Figure 2. Variations in the rate constant (A), specific affinity (B), half-saturation constant (C) of Methanosarcina and Methanosaeta with acetate concentrations, and the ATP yield

and biomass yield (C) with the energy available in the environment. Solid lines are the predictions according to the acclimation model; dashed line in panel D indicates that the predicted ATP yield exceeds the values determined for laboratory cultures and hence is not biochemically feasible. Open symbols are the values determined experimentally for pure cultures and error bards show standard deviations; closed symbols are those determined in the sediments from a lake (■, Lovley and Klug, 1983 and a wetland (●, Roden and Wetzel, 2003).

3.2 Model Predictions

The acclimation model (eqs 4 to 6 and 9) predicts large variations in the kinetic parameters of methanogenesis. In response to the decreases in acetate concentration from 50 mM to 1 μM, the rate constants and the half-saturation constants decrease by up to two orders of magnitude, while the specific affinities increase by up to two orders of magnitude (fig 2). Furthermore, the rate constant decrease is faster in *Methanosarcia* than in *Methanosaeta*, whereas the specific affinity increase is faster in *Methanosaeta* than in *Methanosarcia.* The different responses may reflect the different availabilities of intracellular resources and the differences in the methanogenesis pathway between the two microbes (see Welte & Deppenmeier, 2014).

The acclimation model also predicts notable differences in ATP yield between laboratory cultures and natural methanogens (fig 2D). For example, the culture media contains 50 mM acetate, 12 mM bicarbonate (Rosenberg et al., 2014). Assuming a methane concentration of 1 mM gives the available energy at ~37 $kJ \cdot mol^{-1}$. Under these conditions, equation 9 predicts a yield of 0.6 ATPs per methane, close to the value of *Methanosarcina* cultures. In natural environments, the available energy is small. For example, in the Rømø

aquifer, Denmark, the available energy ranges from 10 to 20 $kJ \cdot mol^{-1}$ (Hansen et al., 2001). Accordingly, the predicted ATP yield varies between 0.1 and 0.3 per methane, and the growth yield varies from 0.5 to 1.5 $g \cdot mol^{-1}$.

The predicted variations in the half-saturation constants agree with the values determined previously for the sediments sampled from a lake and a wetland (fig 2C). The predicted low growth yields are also consistent with the observations that methanogens accounts for <2% of natural microbial communities (Bomberg et al., 2008; Kotelnikova, 2002; Mouser et al., 2016). No other field-determined parameters are available for comparison. Nevertheless, the agreements between the model predictions and the limited field observations support the acclimation model and provide an incentive for future analysis of methanogenesis kinetics in natural systems.

The acclimation model helps improve the predictions of methanogenesis. For example, in the surface sediments of Wintergreen Lake, Michigan, USA, acetate concentration reaches 110 μM, and acetoclastic methanogenesis releases about 24 $kJ \cdot mol^{-1}$ of energy (see Data Repository). From these observations, the acclimation model predicts a rate constant of 4.9×10^{-7} $mol \cdot g^{-1} \cdot s^{-1}$, a half-saturation constant of 0.04 μM, and an ATP yield of 0.3 per methane for *Methanosaeta* in the sediments. Substituting to equation 1 and 8 gives a methanogenesis rate of 3.3×10^{-7} $mol \cdot g^{-1} \cdot s^{-1}$, close to the rate of 5.2×10^{-7} $mol \cdot g^{-1} \cdot s^{-1}$ determined by using the radiotracer method (D. R. Lovley et al., 1982). However, if we directly applied the parameters of *Methanosaeta* laboratory cultures, we would arrive at a value of 6.8×10^{-8} $mol \cdot g^{-1} \cdot s^{-1}$, nearly an order of magnitude smaller than the field observations.

As a second example, in the Rømø aquifer, Denmark, where acetate concentration

is ~1 μM and proceeds at 3.4×10^{-8} mol·g^{-1}·s^{-1} (Hansen et al., 2001). By applying the acclimation model, we predict a rate constant of 1.4×10^{-7} mol·g^{-1}·s^{-1}, 3.6×10^{-3} mM, and a methanogenesis rate of 1.7 to 2.5×10^{-8} mol·g^{-1}·s^{-1}. If we applied the kinetic parameters of *Methanosaeta* cultures, we would arrive at a rate up to 5.8×10^{-10} mol·g^{-1}·s^{-1}, nearly two orders of magnitude smaller than the field observations.

3.3 Reactive Transport Model

The acclimation model is also critical for predicting the competition between *Methanosarcina* and *Methanosaeta*. To illustrate this point, we constructed a reactive transport model for a sediment bed where an acetate solution flows through and the two microbes grow by competing for acetate. We accounted for the transport of chemical species and the methanogenesis and growth of the two microbes, and solved for the steady-state distribution of pore-water composition and methanogen biomass. Details of how we constructed the simulation and related files are available from Data Repository.

We first followed the current practice and tracked methanogenesis and microbial growth by evaluating the autocatalytic model (eqs 1 and 2) with the parameters of the laboratory cultures. To allow methanogenesis to proceed at <0.1 mM acetate, we set the ATP yields to 0. In the simulation results (fig 3), the water chemistry and the methanogen populations have adjusted to a steady state, where acetate concentration decreases, methane accumulates, and the available energy decreases along the flow path. *Methanosarcina* dominates the sediment bed where acetate concentrations are >0.1 mM, but coexist with *Methanosaeta* at <0.1 mM acetate.

Next, we reran the simulation by combining the autocatalytic model with the acclimation model (eqs 4 to 6 and 9). The simulation results differ considerably from the

above (fig 4). The two methanogens segregated into two zones. *Methanosarcina* lives in the upstream portion of the sediment bed, where acetate concentrations remain >0.2 mM. *Methanosaeta* occupies a narrow zone where acetate concentrations range from a few uM to 0.2 mM.

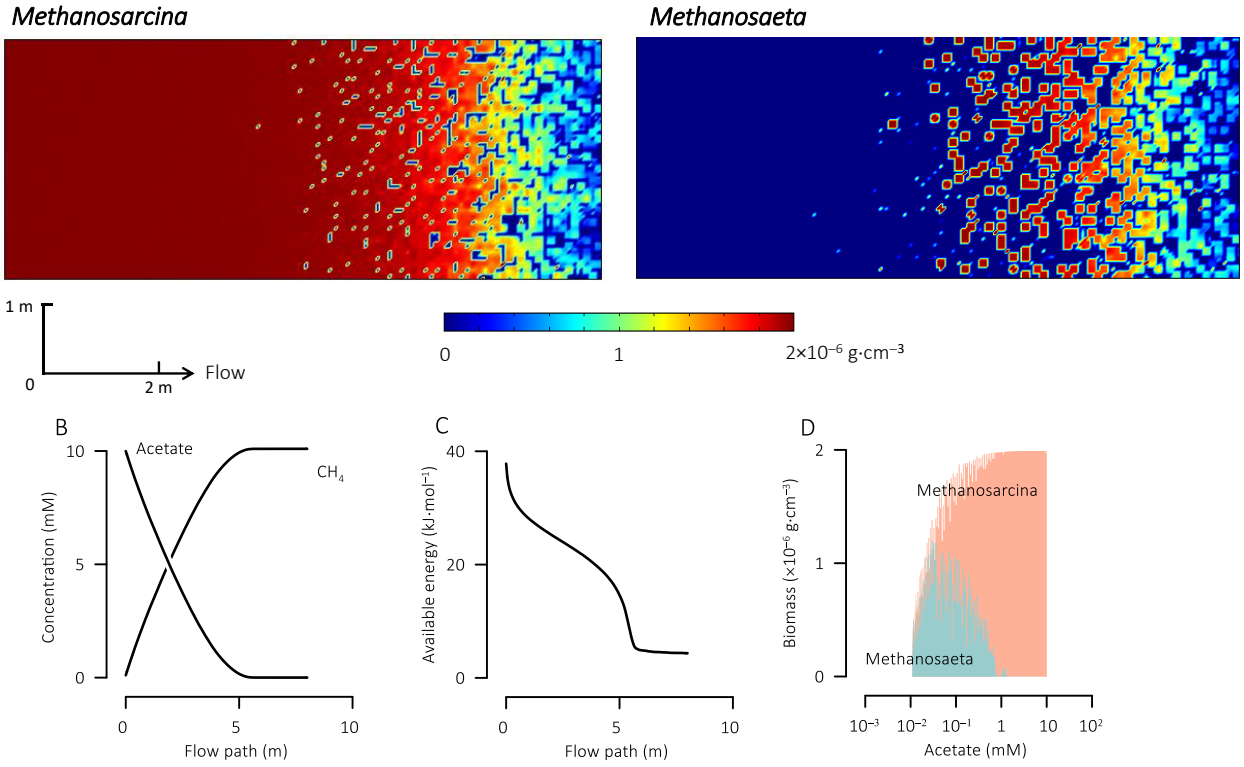

Figure 3. Results at steady state of a reactive transport model in which Methanosarcina and Methanosaeta grow and compete for acetate, showing trends predicted for the distribution of biomass (A), acetate and methane concentrations (B), the available energy (C) along the flow path, and the biomass concentrations across different acetate concentrations (D). Rates of methanogenesis and growth are calculated by evaluating equation 1 and 2 with the parameters of methanogen laboratory cultures. The carrying capacity of the environment is assumed at 2×10–6 g·cm^{-3}.

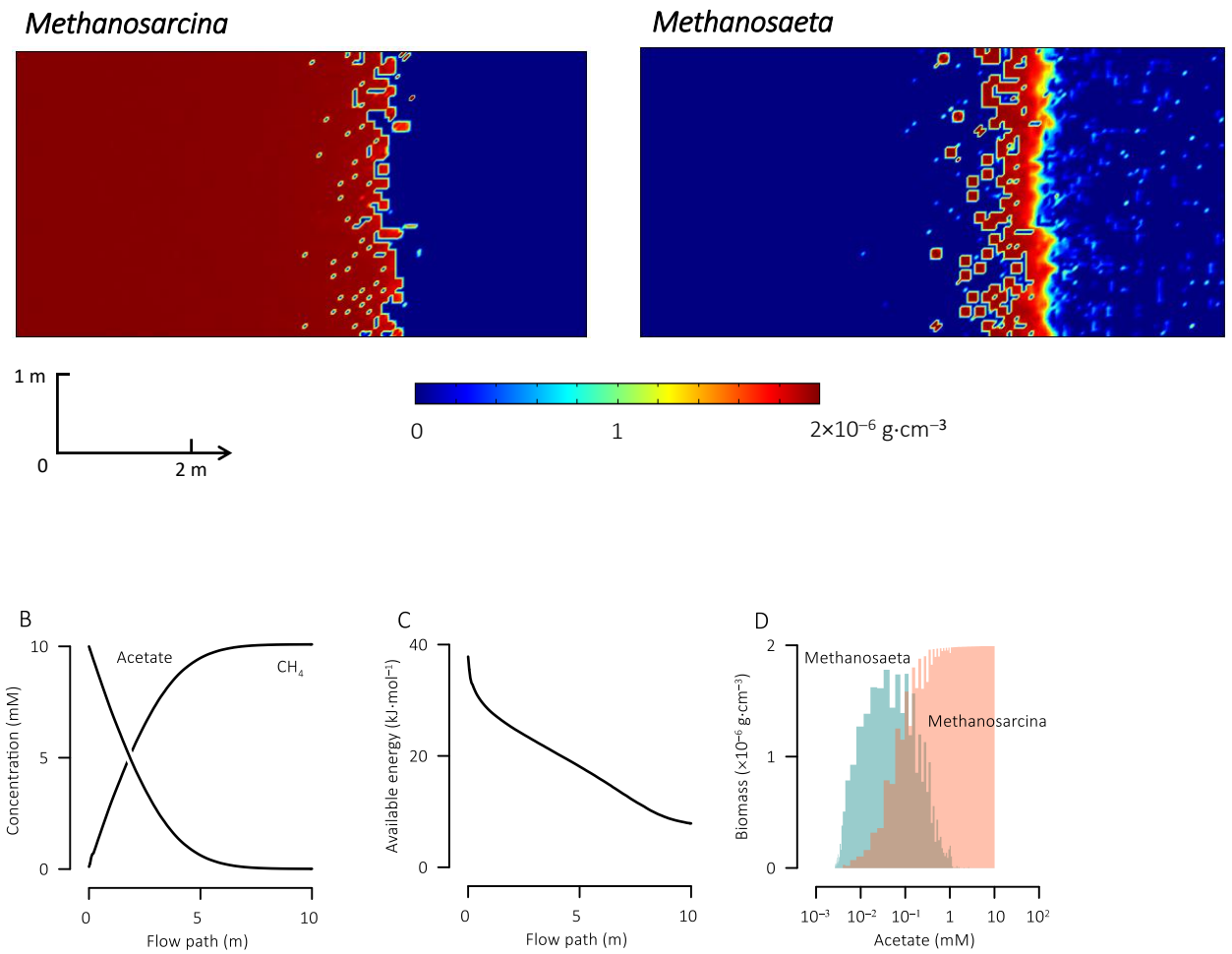

Figure 4. Results of a reactive transport simulation like that shown in figure 2, but this simulation evaluates methanogenesis and growth rates by combining the autocatalytic model (eqs 1 and 2) with the acclimation model (eqs 4, 6, 9 and 10).

The different simulation results underscore the importance of physiological acclimation in predicting the niche separation between the two methanogens. At low acetate concentrations, growth rates depend on the specific affinities and growth yields. Although *Methanosaeta* laboratory cultures have a specific affinity slightly larger than that of *Methanosarcina* cultures, their growth yield is only half of that of *Methanosarcina*. As a result, without acclimation, *Methanosarcina* always grow faster than *Methanosaeta* and our simulation failed to reproduce the dominance of *Methanosaeta* at low acetate

concentrations. However, as illustrated in the second simulation, by acclimating to low acetate concentrations, *Methanosaeta* raises specific affinity and hence growth rate to a greater extent than *Methanosarcina*. At <0.2 mM acetate, *Methanosaeta* grows faster than *Methanosarcina*, leading to the segregation of the two microbes.

4. Discussion

We constructed an acclimation model to describe the variations of methanogenesis parameters with substrate concentrations and thermodynamic conditions, as experienced by microbes in environments of different trophic status. We extrapolate the parameters of laboratory methanogen cultures to natural environments using this new model without introducing new parameters, and therefore overcomes the current technical challenges in analyzing microbial kinetics *in situ*. Such extrapolation is made possible by linking microbial parameters to metabolic resources and by assuming that microbes optimize resource allocation in order to maximize ATP synthesis rates.

In predicting methanogenesis rates, we should consider the extents to which physiological acclimation changes the parameters of methanogenesis (Litchman et al., 2015). Our model predicts that in the environment of low acetate concentrations, methanogens can lower their rate constants and half-saturation constants and raise their specific affinities by more than an order of magnitude relative to the values of laboratory cultures. To overcome the thermodynamic limitation, they also decrease ATP yields. Consequently, by directly applying laboratory observations to natural environments, we may underestimate methanogenesis rates by up to two orders of magnitude.

In predicting the competition between Methanosarcina and Methanosaeta, we should consider how physiological acclimation may shape competition outcome. The

current paradigm accounts for the dominance of Methanosaeta in low-acetate environments by using the kinetic properties of Methanosarcina and Methanosaeta laboratory cultures (Conklin et al., 2006; Min & Zinder, 1989), which does not stand up to scrutiny. Our acclimation model attributes the dominance to the different acclimation responses of the two methanogens. From this perspective, biogeochemical theories built on laboratory observations, such as microbial redox zonation and the dominance of ammonia-oxidizing Archaea in the marine nitrogen cycle (Bethke, 2008; Martens-Habbena et al., 2009), may also need to consider the effect of acclimation.

In summary, our results illustrate an important principle. Microbial kinetics depends on two factors: environmental conditions and physiological acclimation. The former is accounted for by standard microbial rate laws, and the latter factor requires additional models, such as the acclimation model presented here, that relate kinetic parameters to ambient environmental conditions. We focused on methanogenesis here, but the approach should be applicable to iron reduction, sulfate reduction, and other microbial processes. By doing so, we hope to bridge the gap in microbial kinetics between laboratory experiments and natural environments, and to improve the prediction and understanding of microbial processes of geochemical significance.

ACKNOWLEDGMENTS

This research was funded by National Aeronautics and Space Administration under Grant NNX16AJ59G and by the National Science Foundation under Award EAR-1636815 and 1753436.

CAHPTER IV LIMITATIONS OF THE Q10 COEFFICIENT FOR QUANTIFYING TEMPERATURE SENSITIVITY OF ANAEROBIC ORGANIC MATTER DECOMPOSITION: A MODELING BASED ASSESSMENT

1. Introduction

Soil organic matter (SOM) is one of the largest terrestrial carbon reservoirs, and its decomposition plays a key role in biogeochemical carbon cycling. At a global scale, organic matter decomposition drives annual fluxes of 210 Gt carbon dioxide (CO_2) and 0.6 Gt methane (CH_4) into the atmosphere, directly contributing to the CO_2 and CH_4 accumulation in the atmosphere and the resulting global warming by the greenhouse effect (Bardgett et al., 2008; Ciais et al., 2013; Jackson et al., 2020; Nazaries et al., 2013; Thauer et al., 2008). In return, surface warming speeds up the reactions of enzymes and microbes participating in organic matter decomposition, leading to a positive feedback (Gill et al., 2017; Hopple et al., 2020; Romero-Olivares et al., 2017; Wik et al., 2016). Therefore, computer models that predict how organic matter decomposition responds to temperature changes play an integral role in simulating the dynamics of soil carbon storage and the fluxes of carbon cycles, and for forecasting future climate (Allison et al., 2010; Todd-brown et al., 2018; Zheng et al., 2019).

To describe the temperature sensitivity of organic matter decomposition, most models have used versions of the van ′t Hoff's temperature coefficient Q_{10},

$$Q_{10} = \left(\frac{r_1}{r_o} \right)^{\frac{10}{\Delta T}}. \qquad (1)$$

Here r_o and r_1 are the rates of organic matter decomposition at temperature T_o and

T_1, respectively, and ΔT is the difference between the two temperatures (vant' Hoff, 1898). Most models also fix the Q_{10} coefficient at 1.5 or 2, assuming that decomposition rates increase by a factor of 1.5 or 2 per 10 ^{o}C increase, respectively (Foereid et al., 2014; von Lützow & Kögel-Knabner, 2009; Meyer et al., 2018; Peterson et al., 2014; Raich et al., 1991).

However, the Q_{10} approach has proven repeatedly to be inconsistent with laboratory and field observations. For example, the Q_{10} coefficients obtained from laboratory and field studies are not constant, but decrease from >300 at −10 ^{o}C to near 1 around 20 ^{o}C (Hamdi et al., 2013). The Q_{10} approach assumes that reaction rates increase exponentially with temperatures. This assumption originates from the transition state theory for elementary reactions (Eyring, 1935), but its application to complex processes, such as organic matter decomposition, is problematic. Specifically, organic matter decomposition consists of a series of reactions catalyzed by extracellular enzymes and fermenting and respiring microbes, and its rates are often assumed to be limited by the fermentative degradation of complex organic molecules (Allison et al., 2010; Herndon et al., 2015; D. R. Lovley & Klug, 1982; Zheng et al., 2019; Ziemiński & Frac, 2012). Like other microbially-catalyzed reactions, fermentative reactions respond to temperature variations by following unimodal functions (Finke & Jørgensen, 2008; Parashar et al., 1993). Therefore, rates of organic matter decomposition may not vary exponentially with temperatures (Fissore et al., 2008; Hagerty et al., 2014; Hopkins et al., 2014; Raich et al., 2006). Nevertheless, model practitioners continue to use constant Q_{10} coefficients routinely, perhaps because the uncertainty inherent in forecasting the progress of organic matter decomposition outweighs the error introduced by the Q_{10} approach.

The temperature response of organic matter decomposition can also be investigated by biogeochemical reaction modeling. This approach breaks organic matter decomposition into a reaction network that consists of enzymatic and microbial reactions, and simulates numerically the decomposition progress according to the rate laws of enzymatic and microbial reactions (Bethke, 2008). Typical network reactions include the conversion of soil organic matter (SOM) to dissolved organic carbon (DOC) by extracellular enzymes, fermentation reactions that consume DOC, and respiration reactions that oxidize fermentation products by reducing O_2, sulfate, and other electron acceptors (Allison et al., 2010; D. R. Lovley & Klug, 1982; Schink, 1997; Zheng et al., 2019). This modeling approach does not assume *a prior* how organic matter decomposition responds to variations in temperature. Instead, it uses rate laws to relate individual enzymatic and microbial rates to temperature, pH, nutrient concentrations, and other environmental conditions. By integrating the rate laws forward over time, the modeling approach simulates the temperature sensitivity of organic matter decomposition as a systems property that emerges from the interactions between enzymatic and microbial reactions under the constraints of the quality and availability of organic matter and other environmental conditions.

Here we examine the temperature sensitivity of anaerobic organic matter decomposition by comparing the results of the Q_{10} approach with those of biogeochemical reaction modeling. We use as an example anaerobic organic matter decomposition in peatlands in the Upper Peninsula of Michigan, USA (Ye et al., 2016). Unlike previous efforts, we focus not on Q_{10} estimation or the influences of physicochemical or biological conditions of the environment, but on how the choice of an approach for describing the temperature sensitivity might affect the rate predictions of organic matter decomposition,

and hence the fluxes of carbon cycling.

2 Methods

2.1 Q_{10} approach

The Q_{10} approach treats organic matter decomposition as a black box, and provides a simple means of quantifying temperature sensitivity of organic matter decomposition. At temperature T, reaction rate r can be related to the base rate r_o at base temperature T_o according to

$$r = r_o \cdot Q_{10}^{\left(\frac{T-T_o}{10}\right)}. \quad (2)$$

Therefore, its application requires the rate r_o and the Q_{10} coefficient determined at temperature T_o.

2.2. Biogeochemical reaction model

Anaerobic microbial decomposition of organic matter consists of a series of reactions catalyzed by extracellular enzymes and microbes. In the simplest possible configuration (Fig. 1), four reactions would be required to decompose organic matter to CO_2 and CH_4. The first is the degradation of SOM to DOC by extracellular enzymes, followed by the fermentation reaction that consumes DOC and produces acetate and dihydrogen (H_2), and by the methanogenesis reactions that consume acetate and H_2 (D. R. Lovley & Klug, 1982; Schink, 1997; Zheng et al., 2019). Additional reactions occur in the presence of O_2, ferric minerals, humic substances, sulfate, and others, where microbes can oxidize acetate and H_2 by reducing these electron acceptors.

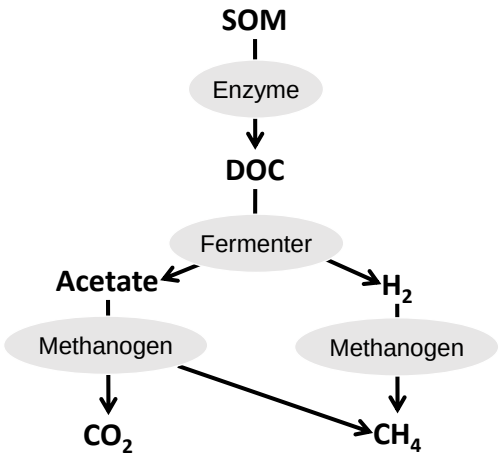

Figure 1. Anerobic organic matter decomposition to CO_2 and CH_4. SOM and DOC are soil organic matter and dissolved organic carbon, respectively; ovals indicate extracellular enzyme and microbial functional groups.

Rates of SOM degradation to DOC depend on the concentrations of SOM and extracellular enzymes and can be described according to the Michaelis-Menten equation. We assume that extracellular enzymes are produced primarily by fermenting microbes and that their production and decay are at steady state. We also assume that SOM degradation is inhibited by the accumulation of DOC. Based on these assumptions, we relate exoenzyme concentrations to the biomass concentrations of fermenting microbes [X_F] (see Text S1), and calculate the rates of SOM degradation according to the revised Michaelis-Menten equation,

$$r = k_{\mathrm{app}} \cdot [\mathrm{X_F}] \cdot \frac{m_{\mathrm{SOM}}}{m_{\mathrm{SOM}} + K_{\mathrm{m,SOM}}} \cdot \max\left(1 - \frac{m_{\mathrm{DOC}}}{m_{\mathrm{DOC,o}}}, 0\right). \quad (3)$$

Here k_{app} is the apparent rate constant (mol·g-biomass^{-1}·s^{-1}), m_{SOM} and m_{DOC} are the molal concentrations of SOM and DOC, respectively, $K_{\mathrm{m,SOM}}$ is the Michaelis constant, and $m_{\mathrm{DOC,o}}$ is the threshold DOC concentration above which the synthesis of the extracellular

enzymes stops. This equation simplifies to

$$r = k_{\text{app}} \cdot [\text{X}_\text{F}] \cdot \max\left(1 - \frac{m_{\text{DOC}}}{m_{\text{DOC,o}}}, 0\right), \quad (4)$$

where $m_{\text{SOM}} >> K_{\text{m,SOM}}$, or SOM concentrations remain nearly constant. Under these conditions, the effect of SOM concentrations can be safely neglected.

We represent microbial reactions using stoichiometric equations, and calculate their rates by using the modified Monod equation (Jin and Bethke, 2003, 2005). Specifically, the fermentation reaction is,

$$\text{DOC} \rightarrow a\text{Acetate} + b\text{H}_2 + c\text{CO}_2 + d\text{H}_2\text{O} + e\text{H}^+, \quad (5)$$

where DOC is represented using a generic chemical formula of $C_6H_{12}O_6$, and *a* and others are stoichiometric coefficients (Tang et al., 2016). Acetoclastic methanogenesis is

$$\text{Acetate} + \text{H}_2\text{O} \rightarrow \text{CO}_2 + \text{CH}_4. \quad (6)$$

Hydrogenotrophic methanogenesis is

$$4\text{H}_2 + \text{CO}_2 \rightarrow 2\text{H}_2\text{O} + \text{CH}_4. \quad (7)$$

Rates *r* of microbial reactions are calculated according to

$$r = k \cdot f_{\text{T}} \cdot [\text{X}] \cdot F_{\text{N}} \cdot F_{\text{T}}, \quad (8)$$

where *k* is the rate constant, or cell-specific maximum rate (mol·g-biomass^{-1}·s^{-1}), f_{T} is the dimensionless factor that describes the temperature response of the rate, [X] is the biomass concentration, F_{N} is the kinetic factor, and F_{T} is the thermodynamic potential factor. The kinetic factor accounts for nutrient concentration m_{N} (molal),

$$F_{\text{N}} = \frac{m_{\text{N}}}{m_{\text{N}} + K_{\text{N}}}, \quad (9)$$

where K_{N} is the half-saturation constant. The thermodynamic factor considers the

Gibbs free energy change ΔG (J·mol^{-1}) of microbial reactions,

$$F_{\mathrm{T}} = 1 - \exp\left(\frac{\Delta G + \nu_{\mathrm{P}} \cdot \Delta G_{\mathrm{P}}}{\chi RT}\right). \qquad (10)$$

Here ν_{P} is the ATP yield – the number of ATPs synthesized per microbial reaction, ΔG_{P} is the phosphorylation energy (the energy consumed by ATP synthesis in the cytoplasm with a value of 45 kJ·mol^{-1}), χ is the average stoichiometric number, which can be taken as the number of electrons transferred per reaction, R is the gas constant (8.3145 J·mol^{-1}·K^{-1}), and T is the absolute temperature. The Gibbs free energy change is calculated from the reaction quotient Q according to

$$\Delta G = RT \ln \frac{Q}{K}, \qquad (11)$$

where Q and K are the reaction quotient and equilibrium constant of the reaction. Variations in the equilibrium costants with temperature are shown in Figure S1.

Evaluating equation 8 requires biomass concentrations [X], which are calculated by using the modified logistic equation. Taking the biomass concentration [$\mathrm{X_F}$] of fermenting microbes as an example,

$$\frac{d[\mathrm{X_F}]}{dt} = Y \cdot r \cdot \left(1 - \frac{[\mathrm{X_F}]}{[\mathrm{X_F}]_{\max}}\right) - D \cdot [\mathrm{X_F}], \qquad (12)$$

where Y is the biomass yield (g·mol^{-1}) – the amount of biomass synthesized per reaction, $[\mathrm{X_F}]_{\max}$ is the maximum biomass concentration supported by the environment, and D is the maintenance rate (s^{-1}). Here the maintenance rate accounts for the decrease in growth rate due to cellular maintenance, metabolic processes that maintain the integrity and function of cellular components but do not contribute to the production of new cells (T. M. Hoehler & Jørgensen, 2013).

2.3. Temperature responses

Unimodal temperature responses are key features of enzymatic and microbial reactions. In general, enzymatic and microbial reaction rates first increase with increasing temperature and, after reaching maximum values at their optimal temperatures, the rates start to decrease. Such temperature responses have been described by both mechanistic and phenomenological models (Alster et al., 2016; DeLong et al., 2017; Rossol et al., 1993; Schipper et al., 2014).

We describe the temperature responses of extracellular enzymes according to the enzyme-assisted Arrhenius equation (DeLong et al., 2017). This equation differs from the standard Arrhenius equation by accounting for the temperature-dependent protein unfolding or denaturation. According to this equation, the apparent rate constant of extracellular enzymes is

$$k_{\mathrm{app}} = k_{\mathrm{app,o}} \cdot \exp\left[-\frac{E_b - E_{\Delta \mathrm{H}}\left(1 - \frac{T}{T_{\mathrm{m}}}\right) - E_{\Delta \mathrm{Cp}}\left(T - T_{\mathrm{m}} - T \ln \frac{T}{T_{\mathrm{m}}}\right)}{RT} \right]. \qquad (13)$$

Here $k_{\mathrm{app,o}}$ is the maximum apparent rate constant, E_{b}, $E_{\Delta \mathrm{H}}$, and $E_{\Delta \mathrm{Cp}}$ are the baseline activation energy ($\mathrm{J \cdot mol^{-1}}$), the change in the activation energy due to the enthalpy of enzyme folding, and the change from the change in heat capacity of the enzymes, respectively, and T_{m} is the melting temperature of the enzymes (K). The values of E_{b}, $E_{\Delta \mathrm{H}}$, and $E_{\Delta \mathrm{Cp}}$ delineate the temperature responses of enzyme reactions (Fig.2A), and are estimated based on laboratory observations of the enzymes harvested from mesophiles. Based on Feller (2010), we take T_{m}, $E_{\Delta \mathrm{H}}$, and $E_{\Delta \mathrm{Cp}}$ as 66 $^{\mathrm{o}}$C, 59 $\mathrm{kJ \cdot mol^{-1}}$ and 2 $\mathrm{kJ \cdot mol^{-1} \cdot K^{-1}}$, respectively. We estimate the E_{b} value by fitting equation 13 to temperature response of

extracellular enzymes reported by Stone et al. (2012). The best-fit E_b is 36.5±1.94 kJ·mol^{-1} (mean ±95% confidence interval). As shown in Figure 2A, the equation captures the temperature responses of the different extracellular enzymes. Figure 2B shows, according to eq 13, how relative rates of exoenzymes change with temperature.

We describe the temperature responses of fermentation and methanogenesis by using the cardinal temperature model – a phenomenological equation (Rossol et al., 1993). Although the Arrhenius equation and related models have also been applied to microbial reactions, our choice of a phenomenological model is based on the complexity of microbial reactions. Microbial reactions are catalyzed by tens to hundreds of enzymes and, according to metabolic control theory, their rates are not controlled by a single rate-limiting enzyme, but by multiple enzymes at the same time (Fell, 1992). Considering that different enzymes tend to display different activation energies and activity levels, and that interactions among enzymes are nonlinear, direct application of the Arrhenius equation to complex microbial reactions can be problematic. On the other hand, phenomenological models do not consider underlying catalytic mechanisms of microbial reactions, but they reproduce well the temperature responses of microbial reactions, which is adequate for our purpose – to predict the temperature sensitivity of organic matter decomposition from the temperature responses of individual reaction steps.

According to the cardinal temperature model (Rossol et al., 1993), the temperature factor f_T of microbial reactions can be calculated according to

$$f_T = \max\left[0,\ \frac{(T - T_{max})(T - T_{min})^2}{(T_{opt} - T_{min})[(T_{opt} - T_{min})(T - T_{opt}) - (T_{opt} - T_{max})(T_{opt} + T_{min} - 2T)]}\right]. \quad (14)$$

Here T_{min}, T_{opt}, and T_{max} are the minimum, optimal, and maximum temperature,

respectively. Compared to other phenomenological models (Heitzer et al., 1991; Ratkowsky et al., 1983; Rossol et al., 1993), the cardinal temperature model is unique in that it describes microbial temperature responses by taking cardinal temperatures as input, without the need of additional parameters. For mesophilic microbes, we set their minimum, optimal, and maximum temperature at 0, 37 and 50 ^{o}C, respectively (R. M. Flores, 2014; Hartel, 2005; Kolton et al., 2019; Singh & Das, 2019). Figure 2C shows, according to the cardinal temperature model, how the temperature factor f_T varies with temperature.

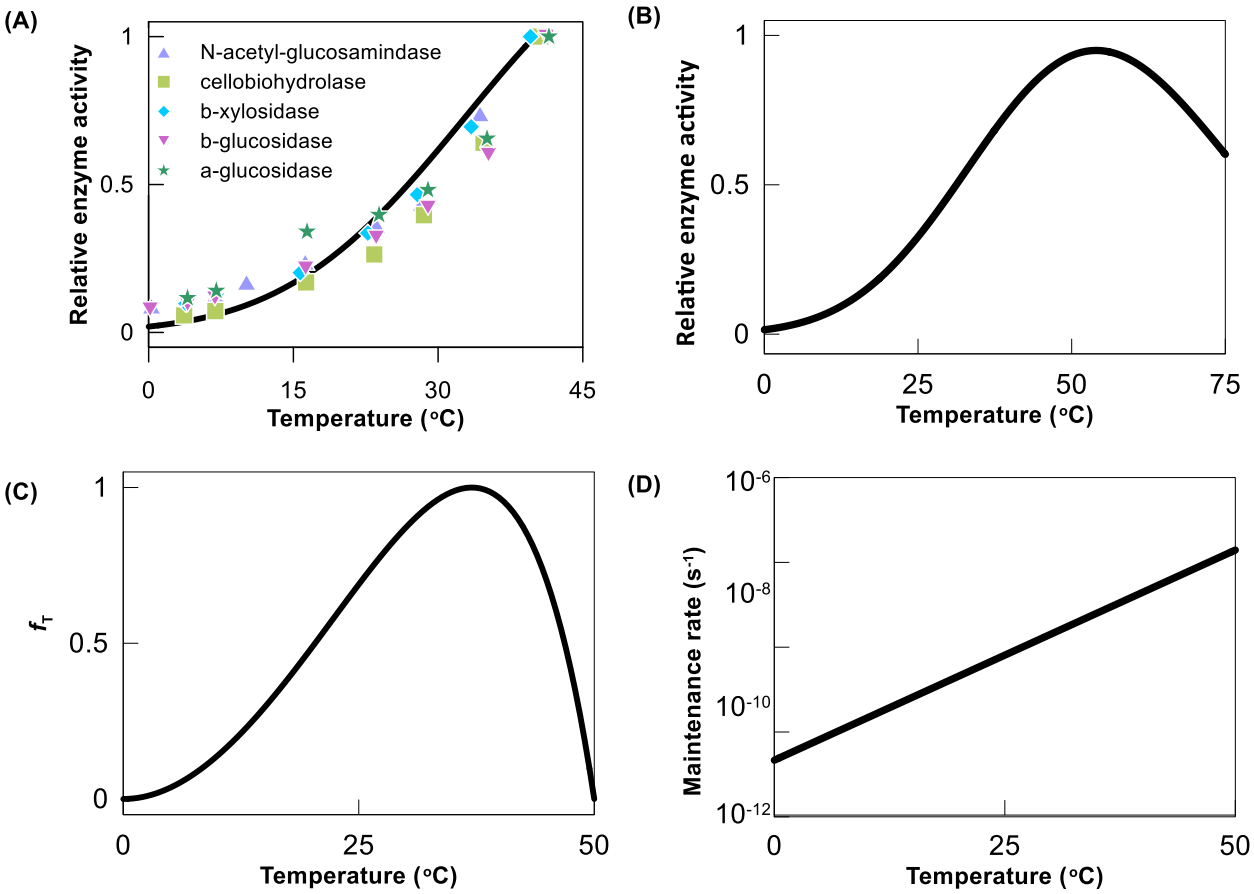

Figure 2. Variations with temperature in the relative activities of extracellular enzymes from soils reported by previous laboratory studies (A) and calculated according to equation 13 (B), the temperature factor f_T of microbial reactions (C), and maintenance rate (D). In panel A, data points are from Stone et al. (2012); relative enzyme activities are

calculated as the ratios of enzyme reaction rates to those determined at 40 ºC; line is the best-fit of equation 13. In panel B, relative enzyme activities are calculated as the ratios of enzyme reaction rates obtained from equation 13 to the maximal rate at 54 ºC.

No mechanistic or phenomenological model is available to calculate maintenance rate at different temperatures. According to the microbial maintenance rates at different temperatures compiled by Price and Sowers (2004), maintenance rates D vary exponentially with temperature, which can be described with the Arrhenius equation (Fig. 2D),

$$D = A_{\mathrm{D}} \cdot \exp\left(\frac{-E_{\mathrm{a,D}}}{RT}\right). \qquad (15)$$

Here A_{D} is the pre-exponential factor (s^{-1}), and $E_{\mathrm{a,D}}$ is the apparent activation energy ($J \cdot mol^{-1}$). Based on the data compiled by Price and Sowers (2004), we set A_{D} at 2.5×10^{10} s^{-1} and E_{D} at 1.02×10^{2} $kJ \cdot mol^{-1}$.

2.4 Sensitivity Analysis

Following the framework of metabolic control analysis (Fell, 1992), we conducted a sensitivity analysis to analyze the significance by which the kinetic parameters of extracellular enzymes and microbes control the rates of anaerobic organic matter decomposition. The scaled control coefficient ε_p^r of a kinetic parameter p on the rate r is the ratio of the fractional change in the rate to the fractional increase of the parameter,

$$\varepsilon_p^r = \frac{p}{r} \cdot \frac{\partial r}{\partial p}. \qquad (16)$$

A coefficient of 0 indicates that the rate of anaerobic organic matter decomposition

is insensitive to the parameter. A value of unity occurs where the rate varies proportionally to the changes of the parameter, indicating a strong control.

2.5. Model application

We implemented the biogeochemical reaction model with PHREEQC (version 3.0) – a software package for geochemical and biogeochemical reaction modeling (Charlton and Parkhurst, 2011). We amended its thermodynamic database by adding SOM and DOC. Table 1 lists the kinetic parameters and their values for computing microbial reaction rates. Some parameter values are taken directly from previous laboratory studies, whereas other parameters, including the maximum apparent rate constant $k_{app,o}$ of extracellular enzymes and the initial biomass concentrations of fermentative and methanogenic microbes, depend on the field site of interest and are determined based on previous experimental observations.

We built the biogeochemical reaction model on the basis of the methane production experiments conducted by Ye et al. (2016). Ye and his colleagues (2016) sampled peatlands from the Upper Peninsula of Michigan, USA (sampling site, rich fen), and incubated the peat slurries anaerobically for 45 days. They included six independent sets of experiments, with and without glucose amendment at 7, 15, and 25 ℃ in quadruplicate. They monitored the concentrations of both intermediate and final products of anaerobic organic matter decomposition, including DOC, acetate, H_2, CO_2, and CH_4 (Figs. 3 and 4). We calibrated and validated the model by comparing and fitting the modeling results to their experimental observations. The amended thermodynamic database and the input PHREEQC scripts are available at https://zenodo.org/record/4480176 (Wu et al., 2021a). Statistical analyses, including one-way ANOVA analysis and Spearman correlation, were

conducted by python 3.7.

Table 1. Kinetic and thermodynamic parameters of microbial reactions

Reaction (substrate)	Kinetic parameter					Thermodynamic parameter	
	Initial biomass ($mg \cdot kg^{-1}$)	Rate constant k ($mol \cdot g^{-1} \cdot s^{-1}$)	Half-saturation constant K_N (molal)	Growth yield Y ($g \cdot mol^{-1}$)	Maximum biomass ($mg \cdot kg^{-1}$)	Average stoichiometric number χ	ATP yield
Fermentation (DOC; glucose)	0.20±0.13[a]	5×10^{-6} (DOC); 2×10^{-5} (glucose)[b]	1×10^{-3} [c]	10.0	0.5±0.01 [a]	1 [d]	2 [e]
Methanogenesis (acetate)	1.85.±0.17[a]	2.9×10^{-6} [f]	1×10^{-5} [g]	1.0	20 [h]	2 [f]	0.2 [f]
Methanogenesis (H_2)	7.0±0.13[a]	7.4×10^{-6} [f]	1×10^{-7} [g]	1.25	20 [h]	2 [f]	0.25 [f]

Note: a. Determined by this study (mean ± 95% confidence interval);

b. Shiloach et al., 1996;

c. Kim et al., 2007;

d. Assuming that glucose uptake is the rate-determining step;

e. Lee et al., 2008;

f. Jin and Kirk, 2018;

g. Hungate, 1967; Stams et al., 2003;

h. Jiang et al., 2010.

3 Results and Discussion

3.1. Anaerobic organic matter decomposition

According to the experimental results of Ye et al. (2016), the SOM decomposition can be represented by a simple reaction network, including enzymatic reaction that hydrolyzes SOM to DOC, the fermentation reaction that consumes DOC and produces acetate and H_2, and the reactions of acetoclastic and hydrogenotrophic methanogenesis (Fig. 1). The fermentation reaction can be described by the stoichiometric equation,

$$DOC \rightarrow 2.7\,Acetate + 1.2H_2 + CO_2 + 0.6H_2O + 2.7H^+ .$$

(17)

At the end of their experiments, the amounts of SOM decomposed by microbes were relatively small, <1% of the SOM available at the beginning of the experiments (see Text S1). Therefore, we calculated the rates of SOM degradation by extracellular enzymes according to equation 4. Furthermore, the acetoclastic pathway dominates methanogenesis, contributing to ~90% of total methane production and leading to nearly equal production of CO_2 and CH_4. Therefore, we quantified the kinetics of anaerobic organic matter decomposition by using the rates of methane production.

3.2. Biogeochemical reaction modeling

To simulate the temperature sensitivity of anaerobic organic matter decomposition, we first constructed the biogeochemical reaction model to describe the progress of organic matter decomposition in the experiments of Ye et al. (2016). We achieved the possible ranges of the five unknown model parameters by least-squared fitting of the modeling results to the observations of the glucose-amended incubation experiments at 7, 15, and 25 ^{o}C. Specifically, the maximum apparent rate constant $k_{app,o}$ of enzymatic SOM degradation was estimated by fitting to the temporal variations of DOC concentrations, and the result was $1.0\pm0.1\times10^{-2}$ mol·g^{-1}·s^{-1}. The initial biomass concentration of fermenting microbes was obtained based on the variations in the concentrations of acetate and H_2. The initial biomass concentration of acetoclastic methanogens was estimated according to the concentrations of acetate, methane, and CO_2. The initial biomass concentration of hydrogenotrophic methanogens was determined from the concentrations of H_2. The maximum biomass concentration of fermenting microbes was determined by fitting to the concentrations of DOC, CO_2, and CH_4. The results are shown in Table 1. As illustrated in

Figure 3, the model simulation reproduces well the experimental results: DOC concentrations decrease during the first 10 days of the incubations, and then stabilize at ~0.22 mM; acetate and H_2 accumulate at the beginning of the experiments; CO_2 and CH_4 accumulate steadily over time.

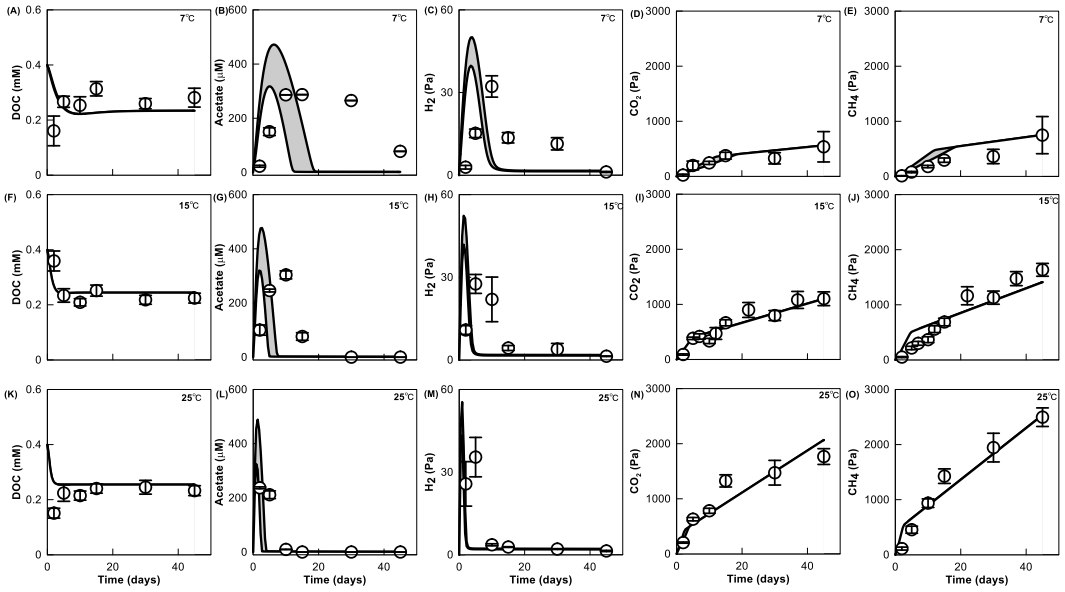

Figure 3. Parameter estimation by fitting the modeling results to the variations with time in the concentrations of DOC (A, F, K), acetate (B, G, L), H_2 (C, H, M), CO_2 (D, I, N), and CH_4 (E, J, O) in the experiments of organic matter decomposition with glucose amendment at 7, 15 and 25°C. Data points are the experimental observations of Ye et al. (2016); error bars show the 95% confidence interval of the observations; solid lines are the simulation results; shaded areas are the simulation results by using the minimum and maximum initial biomass concentrations (see Table 1).

We then validated the model by applying the biogeochemical reaction model, together with the best-fit model parameters (Table 1), to the glucose-free incubation experiments. As shown in Figure 4, without glucose amendment, DOC concentrations increase at the beginning of the experiments, and then stay constant at ~0.25 mM. Acetate

and H_2 do not accumulate significantly, and their concentrations are more than one order of magnitude smaller than those in the glucose-amended experiments. CO_2 and CH_4 accumulate with time at rates slightly smaller than those in the glucose-amended experiments. Simulation results from the 95% confidence intervals of the initial biomass concentrations can cover the majority of the experimental results, except the temporal variations of H_2. The mismatch between the simulated and observed H_2 concentrations is likely due to the technical challenge in analyzing low H_2 level and the incomplete consideration of microbial reactions that consume and produce H_2, such as syntrophic acetate oxidation (Schink & Stams, 2013). Moreover, acetoclastic methanogenesis accounts for approximately 90% of methane production, consistent with the laboratory assessment (Ye et al., 2012). These results suggest that our model captures the experimental observations across the different incubation temperatures and, therefore, can be applied to study the temperature sensitivity of anaerobic organic matter decomposition.

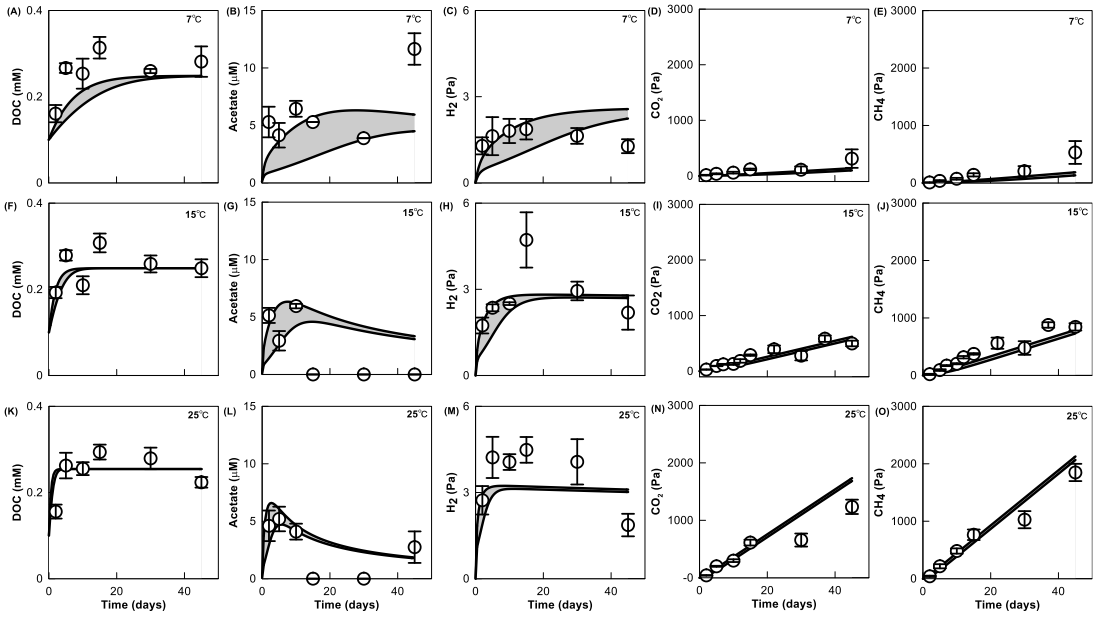

Figure 4. Application of the calibrated biogeochemical reaction model to the

experiments of organic matter decomposition without glucose amendment at 7, 15 and 25°C. Data points are the concentrations of DOC (A, F, K), acetate (B, G, L), H_2 (C, H, M), CO_2 (D, I, N), and CH_4 (E, J, O) reported by Ye et al. (2016); error bars show the 95% confidence interval of the observations; solid lines are the simulation results; shaded areas are the simulation results by using the minimum and maximum initial biomass concentrations (see Table 1).

The modeling results highlight the complexity of the organic matter decomposition even with our relatively simplified reaction network (Fig. 1). First, among the three microbial functional groups, acetoclastic methanogens grow most significantly. Their biomass concentrations increase linearly with time, and the growth rates increase from 6.0×10^{-3} mg·kg^{-1}·d^{-1} at 7 °C to 5.6×10^{-2} mg·kg^{-1}·d^{-1} at 25 °C (Fig. 5A-C). At 7 °C, the growth of fermenting microbes follows the same trend as those of acetoclastic methanogens. But at 15 and 25 °C, the growth is limited by the maximum biomass of 0.5 mg·kg^{-1} assumed in the model. In comparison, the biomass concentrations of hydrogenotrophic methanogens do not respond significantly. The growth limitation of hydrogenotrophs is due to the limited H_2 production, whereas the limitation of fermenters is due to the holding capacity of the environment – the maximum biomass concentration supported by the environment. At the field sites, how physical and chemical conditions, such as nutrient concentrations and the availability and connectivity of space, lead to the limitation requires further investigation.

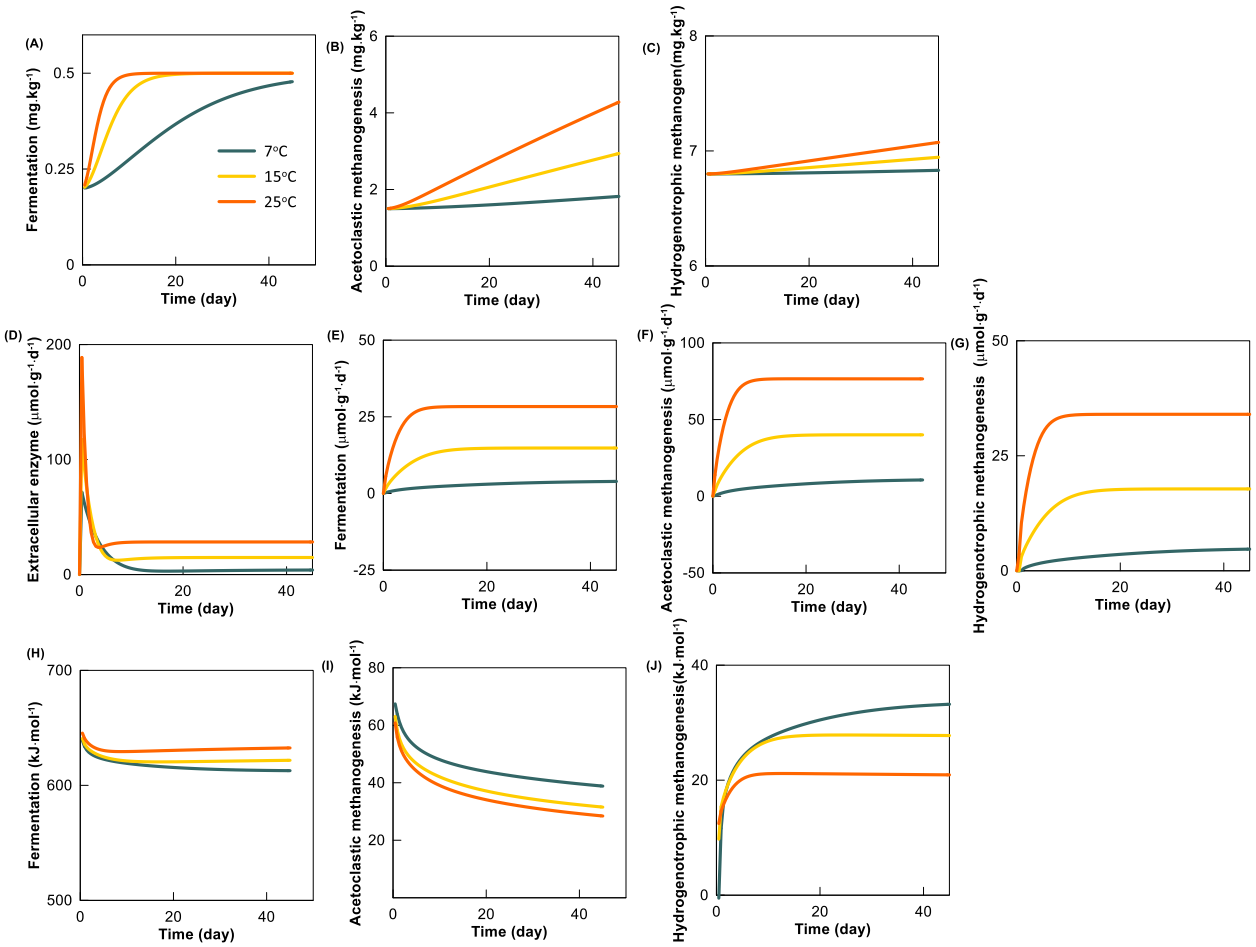

Figure 5. Variations with time in the biomass of fermenting microbes (A), acetoclastic (B) and hydrogenotrophic methanogens (C), reaction rates of extracellular enzymes (D), fermentation (E), acetoclastic (F) and hydrogenotrophic methanogenesis (G), and the Gibbs free energy change ΔG of fermentation reactions (eq 17, H), and acetoclastic (eq. 6, I) and hydrogenotrophic methanogenesis reaction (eq. 7, J) at 7, 15 and 25°C.

Second, the modeling results suggest that the organic matter decomposition can be separated into two phases – a dynamic phase followed by a stationary phase. In the dynamic phase, the enzymatic and microbial reaction rates and hence the rates of organic matter decomposition vary significantly. In the stationary phase, the rates remain nearly

constant (Fig. 5D-G). The time required for reaching the stationary phase depends on temperature, and is 40, 15, and 10 days at 7, 15, and 25 ^{o}C, respectively.

The variations in the reaction rates arise from changes in the environmental and biological factors. For example, variations in the enzymatic reaction rates result from the antagonistic effects of microbial growth and the accumulation of DOC. At the beginning of the experiments, the growth of fermenting microbes raises the rates (Fig. 5A), but later into the experiments, the DOC accumulation (Fig. 4A, F, K) slows the process down.

Variations in fermentation rates (Fig. 5E) match well with the variations in the biomass concentrations of fermenting microbes (Fig. 5A), reflecting the controlling effect of biomass. Acetoclastic methanogenesis rates first increase and then remain constant. Although acetoclastic methanogen continues to grow in the stationary phase, the stimulatory effect of microbial growth is offset by the decrease in acetate concentrations (Fig. 4B, G, L) – another controlling factor of the methanogenesis rate. Our model also considers the limitations of the Gibbs free energy changes. However, the free energies of the microbial reactions are much larger than the energies conserved by microbes (Fig. 5H-J), and hence have limited effect on microbial reactions rates.

We note that acetate accumulates throughout the incubation at 7 ℃ (Fig. 4B). At 15 and 25℃, acetate accumulation is limited to the beginning of the experiments, the first 10 and 5 days, respectively, with empirical results showing even greater acetate depletion (Fig. 4G, L). These results suggest that acetate production by fermentation is not fast enough to compensate for the consumption by acetoclastic methanogenesis at higher temperatures, consistent with the assumption that fermentation is the rate-determining step of anaerobic organic matter decomposition (Fey & Conrad, 2003; Kwietniewska & Tys, 2014).

3.3. Temperature sensitivity

We applied the biogeochemical reaction model and simulated anaerobic organic matter decomposition at temperatures from 0 to 50 ºC. Our simulation ran for 45 days, well past the duration of the initial dynamic phase, and methane production rates are calculated from methane concentrations at day 45. Figure 6 shows that, according to the modeling results, methane production responds to temperature variations by following an asymmetric unimodal curve, and can be described with the cardinal temperature model for mesophilic microbes (eq 14). In particular, the production rate increases almost linearly with increasing temperature from the minimum temperature of 0 ºC to the optimal temperature of 37 ºC, and between 37 and 50 ºC, the rate decreases relatively fast with temperature. These results differ from the exponential responses assumed by the Q_{10} approach, but similar responses have been widely observed in previous laboratory incubation studies (Blake et al., 2015; Morrissey et al., 2014; Sha et al., 2011; Svensson, 1984).

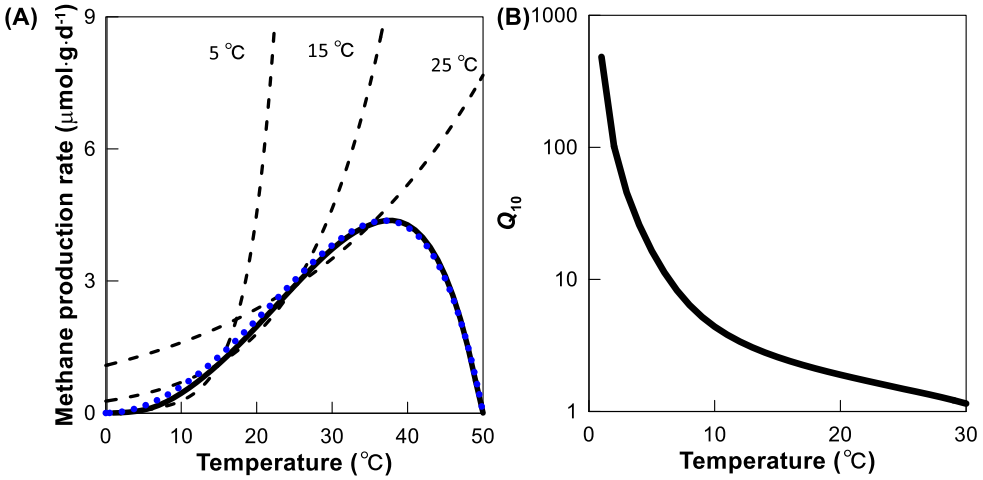

Figure 6. Variations with temperature in methane production rates (A) and Q_{10} coefficients (B). In panel A, the solid line is the results obtained from biogeochemical

modeling, the dashed lines are the predictions according to the constant Q_{10} coefficients obtained at 5, 15, and 25 ^{o}C, and the blue dotted line is calculated according to equation 14 and the maximum rate obtained from the modeling results; in panel B, the Q_{10} coefficients are calculated according to the modeling results in panel A and equation 1.

The temperature sensitivity of anaerobic organic matter decomposition between 0 and 37 ^{o}C is of particular interest, because the simulation results at higher temperatures are likely of limited practical applications for carbon cycling in most soils and sediments. Below 37 ^{o}C, the near-linear relationship can be approximated with a linear function of temperature (Figure 6),

$$r_{CH_4} = \alpha_{CH_4} \cdot T \,. \qquad (18)$$

Here r_{CH4} is the methane production rate, α_{CH_4} is the slope of the increase that characterizes the temperature sensitivity of SOM decomposition, and its value is 0.14 $\mu mol \cdot g^{-1} \cdot d^{-1} \cdot {}^{\circ}C^{-1}$. The near-linear relationship has been reported in peatlands (Avery et al., 2003; Bergman et al., 1998; Nykanen et al., 1998). Moreover, according to a meta-analysis of 376 laboratory incubation data sets, organic matter decomposition rates determined across different climate zones show a curvilinear relationship with incubation temperatures (Xu et al., 2016).

3.4. Q_{10} approach

To apply the Q_{10} approach, we first calculated the Q_{10} coefficient from the modeling results (Fig. 6B). Because methane production rates is 0 at 0 ^{o}C, we calculate the Q_{10} coefficient between 1 and 30 ^{o}C. The coefficient is at its largest value, 484, at 1 ^{o}C and decreases with increasing temperature. The initial decrease is fast – the Q_{10} coefficient

drops to 3 at 13 ^{o}C. Afterwards, the decrease is modest, and the coefficient reaches 1 at 30 ^{o}C. The decreasing Q_{10} coefficient with increasing temperature is consistent with the results of previous laboratory analyses. Hamdi et al. (2013) compiled the Q_{10} coefficients determined for aerobic CO_2 production (n = 317), and found that the Q_{10} values negatively correlate with temperatures, decreasing from >300 at –10 ℃ to 1.2 at 20 ℃.

To test whether the negative correlation between Q_{10} and temperature is also applicable to anaerobic organic matter decomposition, we compiled the Q_{10} values of CO_2 (n = 109) and CH_4 (n = 190) production from anaerobic laboratory incubations (see https://zenodo.org/record/4480176, (Wu et al., 2021b). Two patterns appear from the compilation. First, as shown in Figure 7A, methane production has a larger mean Q_{10} value (4.5) than anaerobic CO_2 production (3.7). Second, according to the results of one-way ANOVA analysis with post-hoc Turkey's test (see Table S1-S4), the Q_{10} values of CH_4 and CO_2 production differ significantly between different climate zones ($p<0.05$, Fig. 7 B and C). In addition, Spearman correlation analyses show that Q_{10} coefficients of anaerobic CO_2 production and CH_4 production correlate negatively with incubation temperatures (Fig. 7D and E, Spearman's coefficient: -0.25 and -0.51, respectively, $p<0.05$). A notable example of this pattern is the 22 Q_{10} values obtained along a 3,800 km long north–south transect of forests in China, with low Q_{10} values in subtropical forests and high Q_{10} values in temperate forests (Wang et al., 2018).

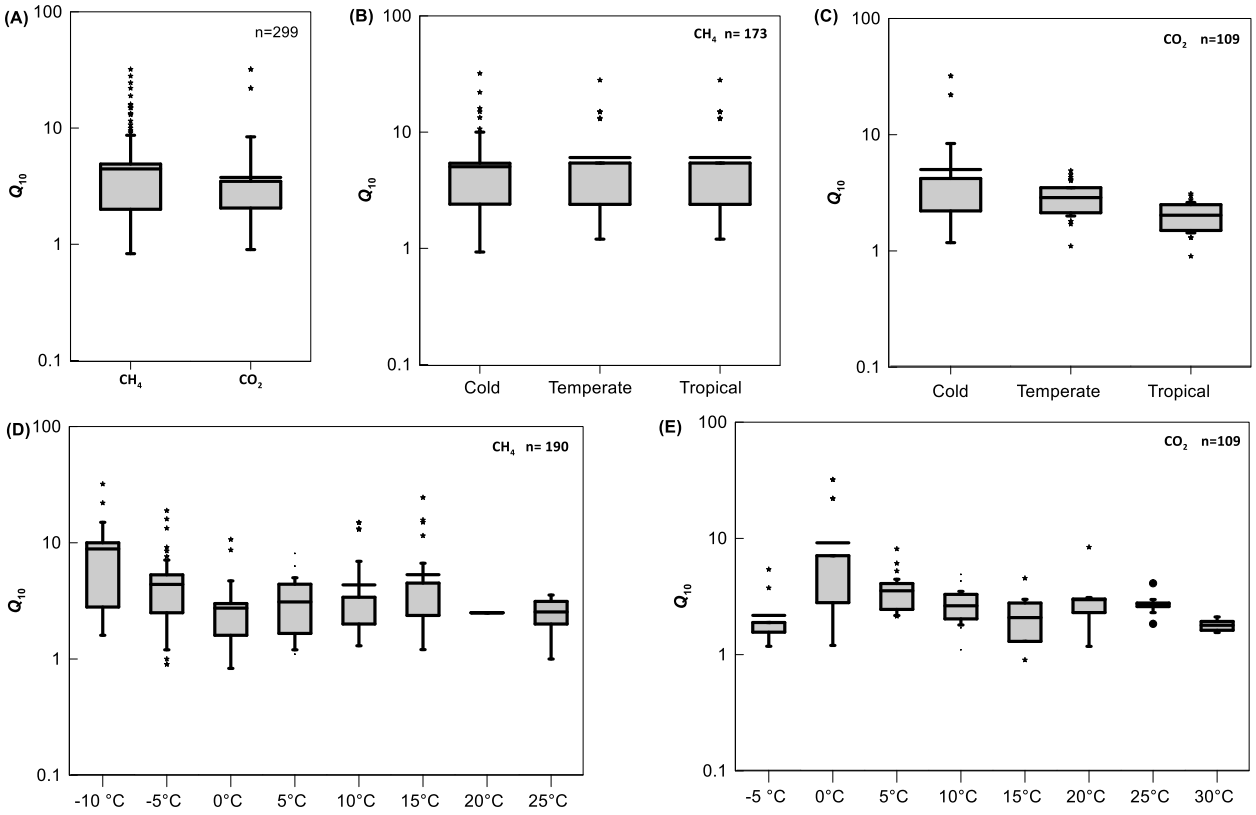

Figure 7. Q_{10} coefficients of anaerobic organic matter decomposition compiled from previous studies. (A) Q_{10} coefficients of CH_4 production and anaerobic CO_2 production. Boxes edges are the 25% and 75% percentiles of the data, horizontal center lines are the mean values, whisker bars show the standard deviation, and the star points are the outliers. Q_{10} coefficients of CH_4 production (B) and anaerobic CO_2 production (C) in different climate zones (only values with sampling locations are included). Q_{10} coefficients of CH_4 production (D) and anaerobic CO_2 production (E) show significantly negative correlation with incubation temperature (Spearman coefficients of -0.25 and -0.51, respectively; $p<0.05$).

The Q_{10} difference between anaerobic CO_2 and CH_4 production has been attributed to the availability of methanogenic substrates and alternative electron acceptors in the

environment (Van Hulzen et al., 1999; Megonigal et al., 2003; Mu et al., 2018). Higher temperatures promote the degradation of SOM and increase the availability of H_2, acetate, and other methanogenic substrates, which in turn raises the temperature sensitivity of CH_4 production (Inglett et al., 2012). At the same time, higher temperatures also speed up microbial CO_2 production coupled to the reduction of ferric minerals, sulfate, and other external electron acceptors. Where these electron acceptors are limited, the temperature responses of CO_2 production are also limited. In addition, changes in temperatures shift the structure and function of microbial communities, which further contributes to the Q_{10} difference between CO_2 and CH_4 production (Auffret et al., 2016; Kolton et al., 2019). In our study, we did not include competing respiring microbial groups and, as a result, the simulated Q_{10} values of CO_2 and CH_4 productions are the same at given temperatures (results not shown).

The inverse relationship between Q_{10} and temperature has been accounted for by the differences in carbon quality or activation energy. In general, recalcitrant carbon tends to have larger activation energies and hence large Q_{10} coefficients than labile carbon (Davidson & Janssens, 2006; Hilasvuori et al., 2013; J. Li et al., 2018). The availability of SOM also constrains the relationship. At high temperatures, SOM decomposition tends to be fast, which lowers the availability of SOM and therefore masks the intrinsic effect of temperature on decomposition rates, lowering the temperature sensitivity (AlMulla et al., 2018; Gershenson et al., 2009; Inglett et al., 2012).

In the biogeochemical reaction model, we fixed the quality and quantity of SOM, and therefore did not consider how SOM affects the Q_{10} values. Instead, the modeling results suggest that the inverse relationship may simply be a reflection of the linear

relationship between methane production rate and temperature. By substituting equation 18 to 1, we can express the Q_{10} coefficient as an inverse function of temperature,

$$Q_{10} = \left(1 + \frac{\Delta T}{T_{\text{base}}}\right)^{\frac{10}{\Delta T}}. \qquad (19)$$

In addition, this equation highlights temperature as the primary determinant of the Q_{10} coefficient. The biogeochemical reaction model considers the kinetic responses of enzymatic and microbial reactions to temperature variations. However, the near-linear relationship between methane production rate and temperature removes the temperature sensitivity of SOM decomposition (i.e., the slope α_{CH_4} of the rate increase in eq 18) from the Q_{10} evaluation (eq 1). As a result, the Q_{10} coefficient does not appear to bear much relevance to the reactions of extracellular enzymes or microbial reactions that drive SOM decomposition.

We apply the Q_{10} coefficients to predict the variations with temperature in the rates of organic matter decomposition. Figure 6A takes 5, 15, and 25 ^{o}C as examples and compares the predictions of the Q_{10} coefficients to the modeling results. The Q_{10} approach underestimates the rates within the temperature ranges where the Q_{10} values are determined, and overestimates the rates outside the temperature ranges. The most significant errors come from the application of the Q_{10} coefficient obtained at 5 ^{o}C. Between 5 and 15 ^{o}C, the Q_{10} approach underestimates the rate by up to 40%, and at 30 ^{o}C, the overestimation is about threefold.

3.5. Rate-determining Step

Discrepancy between predictions of the Q_{10} and the modeling approaches arises mainly from the treatment of the temperature sensitivity of organic matter decomposition.

The Q_{10} approach takes organic matter decomposition as a black box, and assumes that the decomposition rates vary with temperature according to the Arrhenius equation. This assumption does not hold according to the kinetics of enzymatic and microbial reactions. Both enzymatic and microbial reactions respond to temperature variations by following unimodal functions. As shown in Figure 2B and C, beyond the optimal temperatures for extracellular enzymes and microbes, the rates of enzymatic and microbial reactions no longer increase with increasing temperature.

Our modeling results support that the temperature response of anaerobic organic matter decomposition can be described according to the cardinal temperature model (Rossol et al., 1993). We account for this result with the limitation of anaerobic organic matter decomposition by the fermentation reactions that consume DOC (Fey & Conrad, 2003; Glissmann & Conrad, 2002; Kwietniewska & Tys, 2014; Morrissey et al., 2014). We carried out a sensitivity analysis of the biogeochemical reaction model to evaluate the controlling effects of enzymatic and microbial reactions. Figure 8 shows the scaled control coefficients computed for the model parameters at different temperatures. Across the different temperatures, the control coefficient of the cell-specific maximum rate k of fermentation is 106±8%, which indicates that the rate of organic matter decomposition varies proportionally with the rate constant of fermentation. The initial biomass concentration of fermenting microbes also has a relatively large control coefficient, ~80%, at <7 °C, and decreases gradually to 4% at 35 °C. The control coefficient of fermentation growth yield ranges from 10~30% from 5~15 °C, and decreases to 3% at 35°C. Other model parameters do not control significantly organic matter decomposition. For example, the control coefficient of the apparent rate constant $k_{app,o}$ of the enzymatic reaction ranges

from 14% at 5℃ to 3% at 35℃. These results confirm that the anaerobic organic matter decomposition is limited by the fermentation reaction of DOC to acetate and H_2. Because the fermentation reaction responds to temperature variations by following the cardinal temperature model, so does the decomposition of SOM.

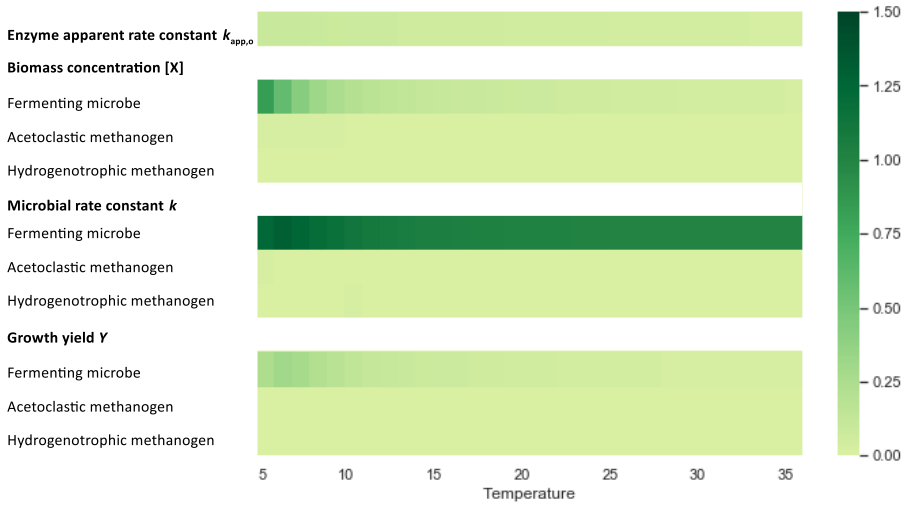

Figure 8. Scaled control coefficients of model parameters at different temperatures (°C). Control coefficients are calculated according to equation 16.

4 Concluding Comments

We explored the temperature sensitivity of anaerobic organic matter decomposition using biogeochemical reaction modeling and compared the modeling results to those obtained from the Q_{10} approach. The biogeochemical reaction model presented here was constructed based on the catalytic mechanism of organic matter decomposition, a network of enzymatic and microbial reactions, and how the kinetics of individual reactions responds to temperature variations. The modeling results captured the influence of individual network reactions on anaerobic organic matter decomposition, and how the decomposition

rates respond to the variations in temperature.

By applying both the biogeochemical modeling and the Q_{10} approach to the peatlands in the Upper Peninsula of Michigan, USA, a number of differences arise:

Whereas the Q_{10} approach treats organic matter decomposition as a black box, biogeochemical modeling accounts for the underlying mechanism of organic matter decomposition, including the reactions of extracellular enzymes, fermentative microbes, and methanogens.

The Q_{10} approach builds on the Arrhenius equation that calculates rates of organic matter decomposition as an exponential function of temperature. In the biogeochemical reaction model, enzymatic and microbial reactions respond to temperature variations by following different unimodal functions.

In contrast to the exponential relationship predicted by the Q_{10} approach, the modeling results show that the temperature response of anaerobic organic matter decomposition follows the same pattern assumed for microbial reactions. In particular, below the optimal temperature of microbial reactions, the decomposition rates vary almost linearly with temperature.

Our study helps make clear the extent to which the Q_{10} approach oversimplifies a complex biogeochemical process. As a result, the Q_{10} approach undermines the kinetic study of organic matter decomposition:

By neglecting the dynamics of organic matter decomposition. Most experimental studies determine Q_{10} coefficients from the accumulative CO_2 and CH_4 productions and the duration of the experiments are variable, from a couple of days to over months (Heslop et al., 2019; Lupascu et al., 2012). But because the rates of organic matter decomposition can

vary with time, the Q_{10} coefficients obtained by using different incubation times can also be different.

By complicating the rate-temperature relationship of organic matter decomposition. As demonstrated by the modeling study here and by previous experimental efforts, the rates of organic matter decomposition do not necessarily vary with temperature exponentially. As a result, Q_{10} coefficients are not a constant, and a series of Q_{10} coefficients would be required to describe the rate-temperature relationship over the temperature ranges of interest.

By failing to provide an accurate description of the temperature sensitivity. Based on the modeling results, the Q_{10} approach overestimates the rates of organic matter decomposition outside the temperature ranges where Q_{10} coefficients are determined. The errors are most significant in applying the Q_{10} coefficients determined near the minimum temperatures of microbial reactions.

By overestimating the rates of organic matter decomposition, the Q_{10} applications introduce errors into the flux predictions of carbon cycling and their potential feedbacks to global climate.

Reliable prediction of reaction kinetics should account for catalytic mechanisms. The biogeochemical reaction model presented here is limited in that it is constructed for a specific field site, and hence does not include reactions that are potentially significant at other environments, such as the respiration of external electron acceptors. It does not consider complicating physical and chemical factors (i.e., water content, organic matter accessibility, and so on) that influence the progress of organic matter decomposition (Gershenson et al., 2009, 2009; Wagai et al., 2013). Therefore, our results likely have

simplified the temperature response of anaerobic organic matter decomposition. Nevertheless, from the dramatic differences between the modeling results and those given by the Q_{10} approach, we can conclude that the Q_{10} coefficient may not be effective as a parameter for quantifying the temperature sensitivity of organic matter decomposition. We also suggest that biogeochemical modeling, combined with laboratory incubation experiments, can be applied to integrate more realistic description of reaction mechanisms into the kinetic study of organic matter decomposition and to uncover the relationship between organic matter decomposition rates and the temperature of the environment.

Data instruction

The amended thermodynamic database, the input PHREEQC scripts for this research, and the compiled dataset of temperature sensitivity of anaerobic CO_2 and CH_4 production are available from Zenodo at https://zenodo.org/record/4480176 (DOI: 10.5281/zenodo.4480066, and 10.5281/zenodo.4480221).

CHAPTER V ENERGY METABOLISM UNRAVELS THE TRADE-OFF BETWEEN ATP FLUX AND ATP YIELD

1. Introduction

Microbes can generate and utilize adenosine triphosphate (ATP) by catabolism and anabolism, respectively, which is also related with ATP flux and ATP yield. Many studies have explored the trade-off between rate and yield of microbial energy metabolism (Brown et al., 2018; Frank, 2010; Malik et al., 2020; Peña-Villalobos et al., 2020). From perspective of thermodynamics, the trade-off of ATP yield and ATP flux rate is caused by the application of net free energy, which is divided into biosysnthesis and driving the reaction pathway. Therefore, larger energies allocated to produce ATP would lead to smaller energies for driving the pathway (Pfeiffer and Bonhoeffer 2002). Specifically, under energetic limitation, the rate of cell growth and the biomass yield are determined by the allocation for anabolism and catabolism (Bauchop & Elsden, 1960; Dykhuizen et al., 1987; Helling, 2002). There might exist a universal principle for energy metabolism that due to the trade-off in thermodynamics, microbes can select a strategy conditions. For instance, Pfeiffer et al. (2001) hypothesized that *E coli* tended to use the fermentation pathway with high ATP yield and low rate when competing for limited energy resources. Du et al. (2018) reported that microbes like *E coli* prefer to choose thermodynamic-favorable or cofactor-use-efficient pathways (i.e. high ATP yield under anaerobic conditions).

Microbes harness energies from the ambient environment and utilize them to maintain their functions of biological molecules and structures (T. Hoehler et al., 2009).

Despite previous studies have noted a thermodynamic trade-off between the rate and efficiency of growth in heterotrophic organisms, these traits have never been found and analyzed from the mechanistic driven cell metabolism in Archaea. Methanogens are recognized as one of the earliest species on the planet, specifically acetoclastic methanogens is an important player, accounting for approximately two thirds of the total annual bio-methane production (Berghuis et al., 2019). Methanogens live close to the thermodynamic limit (Thauer et al., 2008). To cope with this problem, they have evolved elaborate mechanisms of energy conservation that use both protons and sodium as the coupling ions to produce proton motive force. Their energy metabolism help them be outcompeted by other microbial respiration processes. Currently, it is still not abundantly clearly how acetoclastic methanogens conserve enough energy under optimal laboratory conditions, let alone in competitive natural environments. The acetoclastic methanogenesis pathway is strictly anaerobic, the net free energy available for growth is small due to the consumption of 1 or 2 ATP for activation of acetate (Prakash et al., 2019). For the energy metabolism of methanogens, membrane bound enzymes play vital bioenergetic roles in serving on electron transport chains for generating proton/sodium motive forces (Chadwick et al., 2018). Therefore, it is necessary to explore and illustrate the underlying energy conservation mechanisms of acetoclastic methanogens from enzymatic levels.

Here, we took acetotrophic methanogen *Methanosarcina barkeri* as an example to study the energy metabolism via building an enzymatic kinetic model. We assume that methanogens optimize their enzyme concentrations and proton/sodium translocation nubmers to achieve the maximal growth rates. In addition, from an energetic perspective, we assume that the proton/sodium pump out numbers of membrane-bounded enzymes are

not integers but fractions. *Methanosarcina barkeri* can employ energy converting enzymes such as heterodisulfide reductase (HDR), F_{420} dehydrogenase (FPO), Methionine synthase (MTR), Acetyl-CoA synthetase (ACP), methanophenazine-dependent hydrogenase (VHT), energy-converting ferredoxin-dependent hydrogenases (ECH) to produce proton motive force to generate ATP. We accounted these enzymes into the kinetic model, and obtained the optimal ATP yield and enzyme concentrations by maximizing the growth rate. Model simulation results were validated with those results achieved *in vitro*. In addition, we analyzed the importance of each membrane-bound enzyme to growth rates, ATP flux as well as ATP yield. We also conducted a simulation to find out the variation trend in ATP yield with different available energy ranging from 8~70 $kJ \cdot mol^{-1}$.

2. Material and methods

2.1 Enzymatic kinetic model

In the enzymatic kinetic model, we firstly built the enzymatic reaction networks of methanogenesis. Here we only focus on the electron transport chain of methanogenesis, and do not consider the enzymatic reactions in the methyl-group chain. As shown in Figure 1, phosphotransacetylase (PTA) and acetate kinase (ACK) involve into the activation of acetate to acetyl coenzyme A in the first step of acetoclastic methanogenesis of *Methanosarcina barkeri* (Singh-Wissmann & Ferry, 1995). The activation of 1 acetate for *Methanosarcina* species consumes 1 ATP (Jetten et al., 1989). Acetyl-CoA is then split by acetyl-CoA decarbonylase/synthase (ACDS) into methyl group and producing CO_2, respectively. Oxidation of reduced ferredoxin (Fdred) ECH generates H_2 inside the cell, then H_2 diffuses across the cell membrane to the VHT active site, where it is oxidized and electrons are used to reduce methanophenazine (MP_{red}). Then the electron flows go through

HDR, MTR, coupled with MCR to produce CH_4. Portions of the methanogenic pathway that are not required for aceticlastic methanogenesis, including the use of Frh, but which can produce metabolites to support acetoclastic methanogenesis.

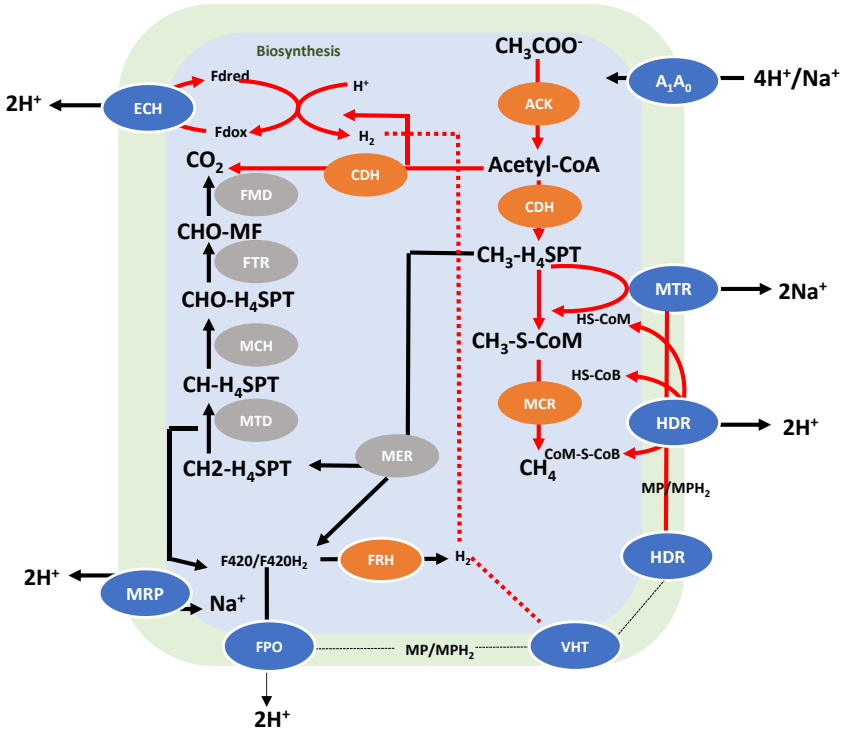

Figure 1 Acetoclastic methanogenesis network of Methanosarcina barkeri. Green frames represents the membrane, blue rectangular is the cell cytoplasm. Orange and blue oval are the methyl-group enzymes and membrane-bound enzymes, respectively.

In this study, we assume that membrane-bound enzymes are adjustable proton/sodium pump, it translocates 0~2 protons during acetoclastic methanogenesis. We split enzymatic reactions with electrons pumped out/in to two reactions. One reaction is without proton/sodium involved, the other reaction is written as full proton/sodium pumped out/in. Therefore, the coefficient of proton/sodium translocated per pair of electrons by membrane-bound enzymes are no longer fixed, but changed based on the fractions of

enzymes participated in the two reactions. The rates of enzymatic reactions are computed using reversible Michaelis-Menten equation.

$$r_i = k_{i+} \cdot [E_i] \cdot F_M \cdot F_T \tag{1}$$

where k_{i+} and $[E_i]$ are the maximum specific rate ($mol \cdot g^{-1} \cdot s^{-1}$) and the concentrations for enzyme *i* in the unit of percentage of proteins, respectively. F_M is the metabolite factor,

$$F_M = \prod_S \frac{m_S / K_S}{1 + m_S / K_S + m_P / K_P} \tag{2}$$

and F_T is the thermodynamic factor,

$$F_T = 1 - \exp\left(-\frac{f}{RT}\right) \tag{3}$$

f is the thermodynamic drive, which is calculated by using equation 4. The ATP yield is calculated using equation 7.

$$f = \Delta G_A - \Delta G_C \tag{4}$$

ΔG_A is calculated using eq 5 and eq 6 for redox reactions and non-redox reactions, respectively.

$$\Delta G_A = nF(E_a - E_d) \tag{5}$$

$$\Delta G_A = -RT \ln \frac{Q}{K_{eq}} \tag{6}$$

Where *n* is the moles of electrons transferred in the reaction. *F* is Faraday constant (96485 C mol^{-1}).

Conserved energy is shown in equation 7,

$$\Delta G_{\mathrm{C}} = \nu_p \cdot \Delta G_P \tag{7}$$

Where ν_p is the ATP yield number, which is determined by the ratio of net ATP flux with MCR flux. Here we take ΔG_P as the value of 45 kJ·mol^{-1}. This enzymatic kinetic model can provide the optimized enzyme concentrations of *Methanosarcina barkeri*. In addition, we also adjusted the number of proton/sodium produced by membrane-bound enzymes in acetoclasstic methanogesis ranging from 0 to 2 with 0.1 step, to find out the optimized proton translocation numbers where methanogens can achieve maximal growth rate.

2.2 Thermodynamic efficiency

Methanogens conserves energy by pumping out proton/sodium from membrane to generate proton motive forces. Part of energy is used for complex biosynthesis, the rest of energy drives the methanogenesis pathway. Adjusting the proton numbers will affect the ATP flux and yield at the same time.

The thermodynamic efficiency η can be represented as follows,

$$\eta = \frac{-J_a \cdot \Delta G_a}{J_c \cdot \Delta G_c} \tag{8}$$

Where J_a and J_c are the anabolic flux and catabolic flux, respectively. The rate of substrate consumption equals the sum of the rate of biomass formation and catabolic formation.

2.3 Data collection

The kinetic parameters including rate constant *k*, K_M of enzymes and corresponding metabolites are compiled from BRENDA database of *Methanosarcina barkeri* cultivated

with acetate, pH equals to 7, at temperature of 37℃. Enzyme kinetic models is implemented by using COPASI 4.27.

3. Results

3.1 Model simulation and validation

We validated the metabolic model by simulating the methanogenesis of *M. barkeri* under typical laboratory culturing conditions (i.e.50 mM acetate, 37 ºC, and pH = 7). The optimized enzyme concentrations are shown in Figure 2A. For enzymes in the cytoplasm, MCR is the most abundant with concentrations around 12% of the total protein. Other enzyme concentrations of ACK, PTA and ACDH and most membrane-bound enzymes are about 1~2% of the total protein. Compared with the enzyme concentrations obtained from laboratory results, our model simulation results can capture the distribution of enzymes of actoclastic methanogenesis of *Methanosarcina barkeri* (Figure 2B).

The simulated acetoclastic methanogenesis rate is 1.74×10^{-6} mol·g^{-1}·s^{-1}, which is close to the methane production rate of *Methanosarcina barkeri* using acetate *in vitro* (Clarens & Moletta, 1990; Rajoka et al., 1999). Production of H_2 concentrations at steady state of acetoclastic methanogenesis is approximately 7.05×10^{-7} mol·L^{-1}, within the range of laboratory results (i.e. 1.23×10^{-7} ~7.09×10^{-7} mol·L^{-1}, Lovley and Ferry, 1985).

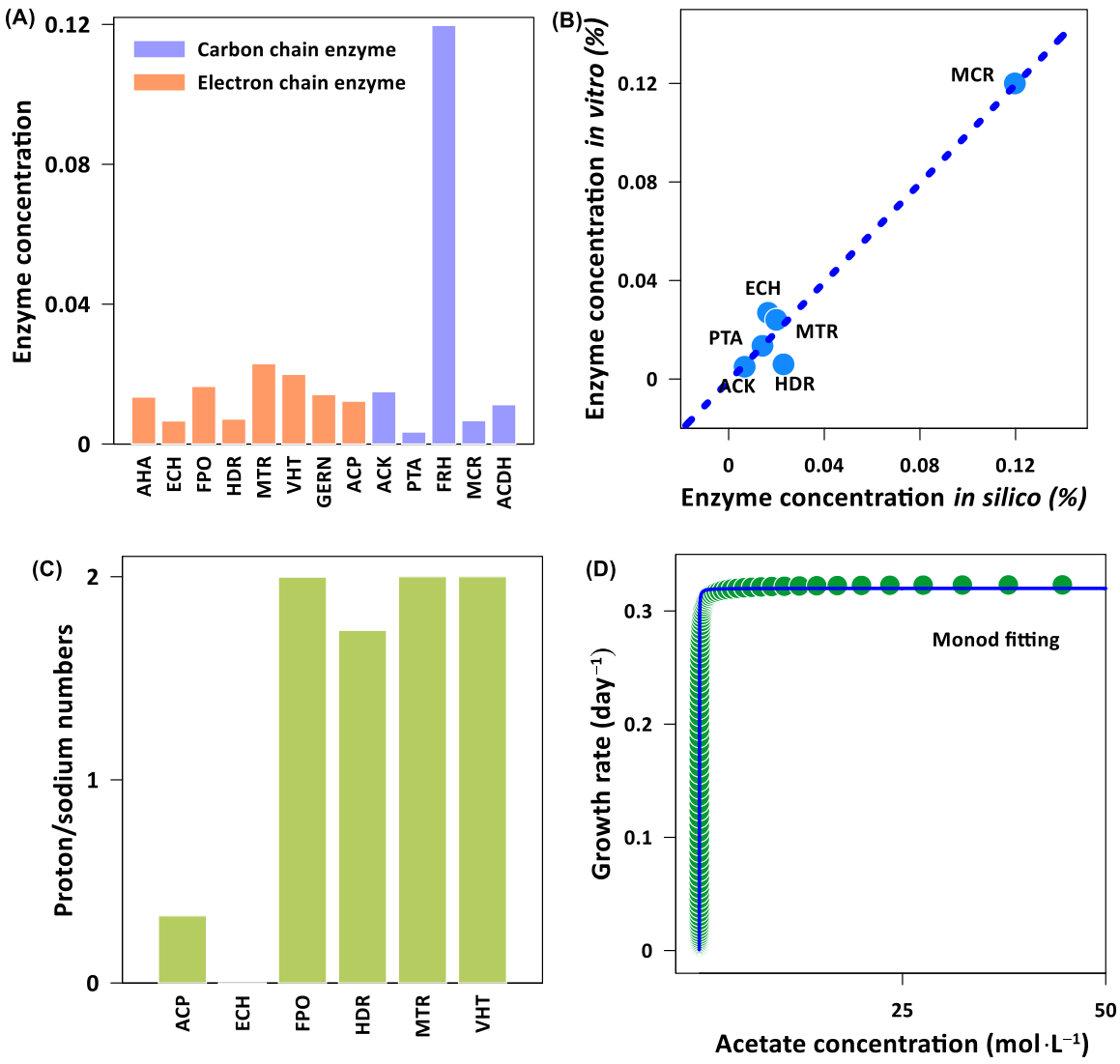

Figure 2 Simulated enzyme concentrations (A), comparison with enzyme concentrations in vitro (B) and proton/sodium numbers translocated by membrane bound enzymes (C), as well as monod fitted growth rate against acetate concentrations. In panel A, the orange and purple bars are the enzyme in electron transport chain and carbon chain, respectively. In panel B, the blue dotted line is the 1:1 ration slope.

3.2 Proton translocation numbers of energy converting enzymes

The model simulation results also gave the optimized proton/sodium translocation numbers of membrane-bound enzymes (Figure 2C) when *Methaosarcina barkeri* achieving the maximal growth rate. Figure 2C shows that energy-conserving membrane-associated

enzymes including FPO, HDR, MTR and VHT can function at their full efficiency with pumping out 2 protons/sodiums. Whereas, ACP can only pump in 0.3 protons due to that ACP reaction consumes the proton motive force. ECH, a H_2-evolving enzyme, belongs to the group of [NiFe] hydrogenase (Schoelmerich & Müller, 2019) that catalyzes the oxidation/reduction of ferredoxin coupled to H_2 reduction/oxidation. The optimized translocation number of ECH for the first time is about 0.3; meanwhile H_2 concentration is $1\times10^{-8}\,mol\cdot L^{-1}$, which is relative lower than the laboratory results. Thus we sweep the proton translocation numbers of ECH to find the best value where H_2 concentration is close to the laboratory results. Figure 2C shows that the ideal proton translocation number of ECH is 0, indicating ECH reaction does not pump out protons.

When we adjusted the proton translocation numbers, the results show that all membrane-bounded energy converting enzymes can function to produce proton motive force. Despite the individual proton/sodium numbers may change a little, the total proton/sodium translocation numbers keeps constant of 7.5 per methane produced.

3.3 The influence of proton/sodium translocation numbers on ATP flux and yield

To explore at what extent proton/sodium translocation numbers affect the growth rate of *Methanosarcina barkeri*, we sweep the proton/sodium numbers of each membrane-associated enzyme. As shown in Figure 3, increased proton/sodium translocation numbers by all enzymes except ACP can enhance the ATP yield. On the contrary, elevated proton/sodium translocation numbers of ACP results in decreased ATP yield and increased ATP flux. This is possibly caused by ACP reaction is endergonic, which invests the electrochemical potential by translocating protons into the cytoplasm (Welte et al., 2010). In addition, increases in the proton/sodium translocation numbers of ECH, MTR, HDR,

and VHT reduce the ATP flux (Figure 3). The opposite trends for ATP flux and ATP yield suggest a trade-off between rate and yield in energy metabolism of methanogen. For FPO reaction, the variation trends in ATP flux and MCR flux are not significant. This is possibly due to that FPO reaction is not directly contribute to the MCR reactions or redox potential chains. As we mentioned in Chapter II, MCR reaction is the last and key step for methane production in all methanogenesis pathways. Therefore, reactions affecting the MCR reactions are potentially important factors in energy metabolism of methanogenesis.

Figure 3 also shows that variations in proton translocation numbers of ECH highly affect the ATP yield, increasing from 0.4 to 0.9. At the same time, ATP flux shows highest value with changes in sodium translocation numbers of MTR. Metabolic control analysis also suggests that ECH and MTR enzyme reactions are dominating in determining the growth rate. MTR transfers the methyl group from the CH_3-H_4SPT to coenzyme M, then establishes a sodium-motive force across the membrane. MCR then reduces methyl-coenzyme M to produce methane through using coenzyme B as an electron donor. The established disulfide bond between these coenzymes is then broken again by HDR and VHT (Berghuis et al., 2019). Thus, MTR reaction can directly affect the metabolites of MCR reaction, further affecting the growth rates. ECH reaction affects the growth rates by influencing the redox potential through the electron transport chain.

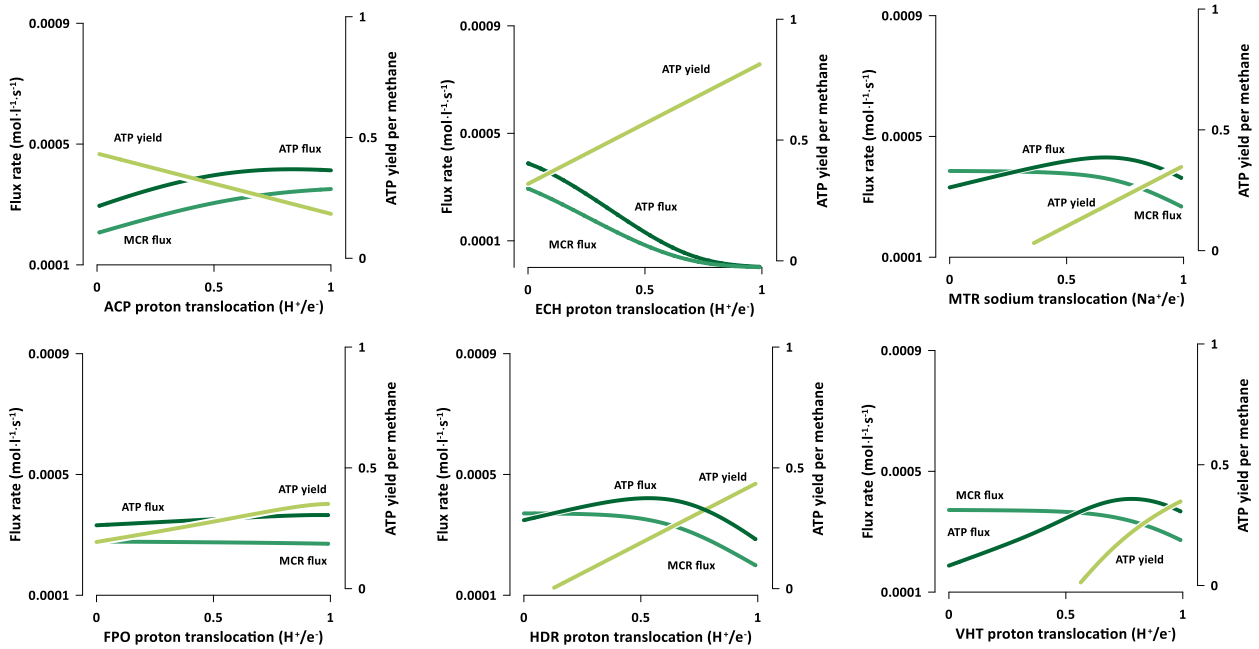

Figure 3 Impact of proton/sodium translocation numbers on ATP flux rate and ATP yield of ACP, ECH, MTR, FPO, HDR, and VHT enzymes.

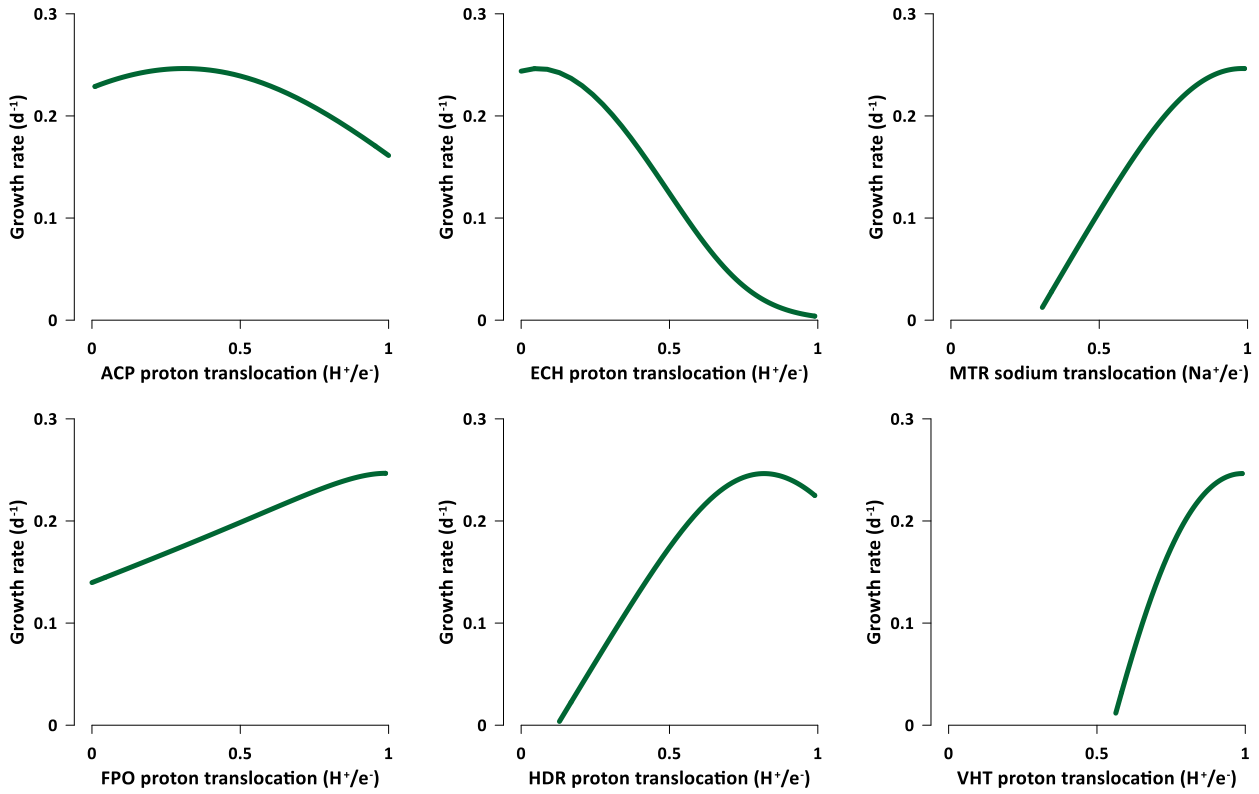

Figure 4 Impact of proton/sodium translocation numbers of ACP, ECH, MTR, FPO, HDR, and ECH on growth rates of Methanosarcina barkeri

Growth rate of *Methanosarcina barkeri* is determined by the difference between total ATP flux and (acetate kinase) ACK enzymatic flux, i.e the net ATP flux. Therefore, the growth rate did now show exactly the same pattern with ATP flux or MCR flux with variations in proton/sodium translocation numbers. Consistent with Figure 2C, Figure 4 shows the maximal growth rate at specific proton/sodium translocation numbers. Different with other energy conserving enzymes, growth rates decreased with proton numbers pumped by ECH. This can be explained by the maximal redox potential of H_2/H^+ without pumping out protons.

3.4 Adaptation of ATP yield to different ranges of available Gibbs energies

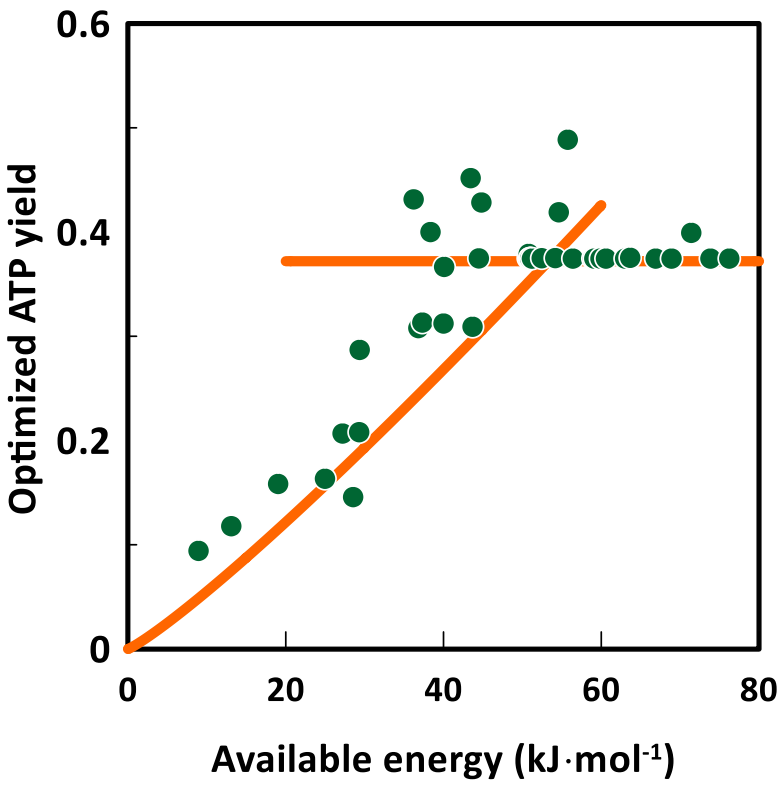

Figure 5 Variations in ATP yield of Methanosarcina barkeri against with ambient available energies.

We assume that methanogens adapt to limited energy resources by lowering their

ATP yield to larger the thermodynamic drives to boost the methanogenesis. We randomly select the concentrations of chemical compounds including acetate, bicarbonate and methane to obtain different available energy in the environment ranging from 8 to 80 $kJ \cdot mol^{-1}$. Then we ran the optimization model of acetoclastic methanogenesis to find the optimized ATP yield. As shown in Figure 5, changes of optimized ATP yield shows a similar trend in equation 9 of Chapter III, further proving the hypothesis in perspective of cell metabolism. This results demonstrates that at thermodynamic limitation environment, microbes tend to lower the anabolism flux and contribute more to catabolism to get a maximal growth rate. When the available energy can support the growth of microbes, the ATP yield will be a constant.

4. Discussion

The simulation in our study challenges the current paradigm of energy conservation by *Methanosarcina* via chemiosmosis. Chemiosmosis conserves energy by translocating ions across the membrane and building electrochemical potential. Current models often fix the stoichiometry of proton/sodium translocation as integers. Specifically for the study on methanogenesis, many studies have reported that the proton translocation number of ECH is 2 protons per pair of electrons (Buckel & Thauer, 2013; Kaster et al., 2011; Thauer et al., 2008). However, these values are not always fixed constants. For example, Welte et al., (2010) reported that the ECH participates energy conservation of methanogenesis by the translocating1 proton from their inhibitor studies. Previous simulation model of *Methanosarcina barkeri* (iAF692) also applied 1 proton per pair of electrons to enable the model to generate consistent simulation results with experimental data for methanogen growing on substrates such as methanol and acetate (Feist et al., 2006; Thor et al., 2017).

The stoichiometry of ECH reaction was later updated in iMG746 to 2 protons/$2e^-$ (Gonnerman et al., 2013; Thor et al., 2017). Similar with ECH, the translocation stoichiometry of other membrane associated enzymes also changes. Results of *Methanosarcina Mazei* showed that FPO exhibited a stoichiometry of 0.9 H^+ translocated per two electrons transferred (Bäumer et al., 2000). Benedict et al. (2012) tested their hypothesis of proton pumping out numbers of rhodobacter nitrogen fixation (RNF) and MRP of Methanosarcina acetivorans by conducting sensitivity analysis of proton/sodium translocation numbers in light of experimental data. Their results showed that the best match occurred when RNF was set to pump 3 Na+/2 e- and when MRP was set to pump 1 H^+/Na^+.

Methanogens, like all living organisms, use energy derived from metabolic processes to drive growth and maintain cellular functions. They require ion gradient-dependent ATP generation as their principal energy conservation mechanism. The energy metabolism analysis of acetotrophic methanogenesis in our study unravels that methanogens adapt to the ambient environment by adjusting the ATP yield to drive the methanogenesis pathways. This adjustment is highly dependent on the ambient available energy. When the environment energy is high enough for supporting the microbial growth, ATP yield will be a constant. Despite we focus on acetoclastic methanogenesis, we can also apply this approach to other microbes to test if the trade-off between ATP flux and ATP yield existed in other methanogenesis pathways or other microbial reactions under different thermodynamic conditions.

Understanding how microbes conserve energy at different thermodynamic environment is a fundamental open question in field of biogeochemistry. To systematically

explore how energy flows distribute to catabolism and anabolism as well as the strategies for methanogens to conserve energy under different available energy conditions, we applied advanced optimization algorithms and enzymatic kinetic parameters to acetoclastic methanogenesis metabolism. Specifically, we searched for the detailed proton/sodium translocation numbers by individual membrane-bound enzymes, and analyzed their corresponding contributions. Our results suggest that the stoichiometry of proton/sodium translocation per pair of electrons can be adjusted to achieve maximal growth rate. The model simulation results also show that variations in ATP yield increase with elevated available Gibbs energy. In addition to helping understand energy metabolism of methanogens, our approach could assist in explaining the species evolution under limited energy.

APPENDICES

APPENDIX A

CHAPTER II SUPPLEMENTARY INFORMATION AND FIGURES

Appendix A is the supplementary data and information for Chapter II. There are five supporting figures and data.

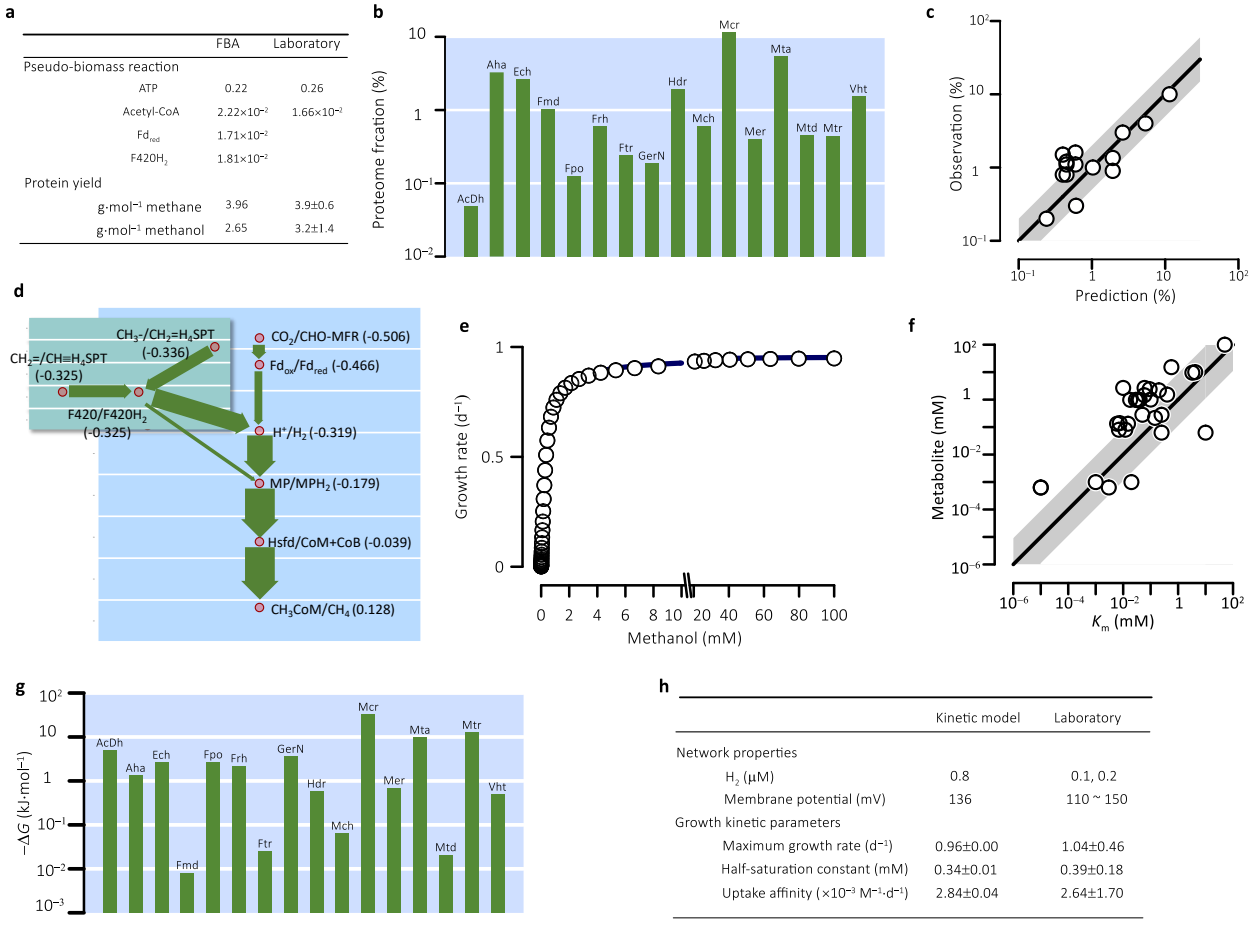

a

	FBA	Laboratory
Pseudo-biomass reaction		
ATP	0.22	0.26
Acetyl-CoA	2.22×10^{-2}	1.66×10^{-2}
Fd_{red}	1.71×10^{-2}	
$F420H_2$	1.81×10^{-2}	
Protein yield		
g·mol⁻¹ methane	3.96	3.9±0.6
g·mol⁻¹ methanol	2.65	3.2±1.4

h

	Kinetic model	Laboratory
Network properties		
H_2 (μM)	0.8	0.1, 0.2
Membrane potential (mV)	136	110 ~ 150
Growth kinetic parameters		
Maximum growth rate (d^{-1})	0.96±0.00	1.04±0.46
Half-saturation constant (mM)	0.34±0.01	0.39±0.18
Uptake affinity ($\times10^{-3}$ $M^{-1}\cdot d^{-1}$)	2.84±0.04	2.64±1.70

Figure S1 The kinetic model reproduces independent experimental observations of M. barkeri laboratory cultures. a. Stoichiometric coefficients of pseudo-biomass reaction

derived by performing FBA with the M. barkeri iMG746 genome-scale metabolic model and from laboratory observations. b. Optimized proteome fractions of methanogenesis enzymes. c. Optimized proteome fractions of methanogenesis enzymes are in agreement with those determined from in vitro cell-free lysates. Solid line shows the 1:1 ratio; shaded area covers up to 2-fold deviations from the 1:1 ratio. Pearson correlation is rp[15] = 0.97 ($p<0.01$). d. Electron fluxes from the oxidation to the reduction of methyl-group in methanol. The electron flux via the redox couple of H+/H2 accounts for 86.4% of the total electron fluxes, while the redox couple F420/F420H2 accounts for the remaining 13.6%, consistent with the dominant role of hydrogen cycling detected by laboratory experiments. Values in parentheses show the reduction potentials (V); arrow widths indicate the magnitudes of the fluxes relative to the flux to the reduction of methyl-coenzyme M to methane (i.e., 1.74×10^{-18} mol·s–1). The similar reduction potential of H^+/H^2 and $F_{420}/F_{420}H_2$ agrees with laboratory observations. e. Specific growth rates vary hyperbolically with ambient methanol concentrations. Data points are the modeling results; solid line represents the results of the least-square fitting to the Monod equation; the mean square error of the fitting is 1.8×10^{-5}. f. ~84% of metabolites have concentrations greater than the respective Michaelis constants Km, a pattern that has been detected in E. coli. Solid line shows the 1:1 ratio; shaded area covers up to tenfold deviations from the 1:1 ratio. g. Gibbs free energy ΔG is unevenly distributed among enzyme reactions, another pattern detected in E. coli. h. Comparison of H_2 concentration, membrane potential, and growth kinetic parameters predicted by the kinetic model to those determined by laboratory experiments. Laboratory data are compiled in Supplementary Table.

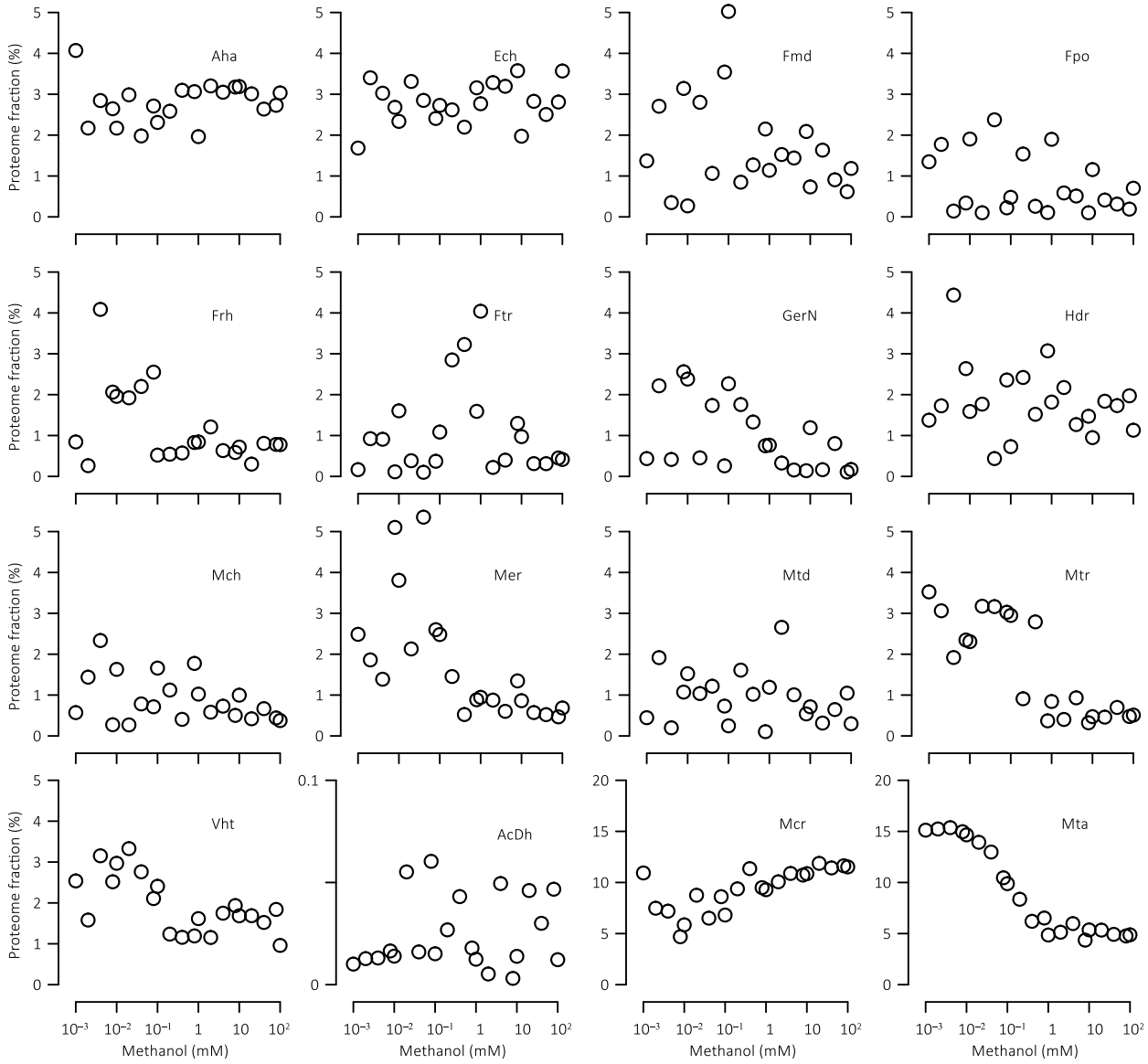

Figure S2 Optimal proteome fractions of methanogenesis enzymes at different methanol concentrations of acclimation.

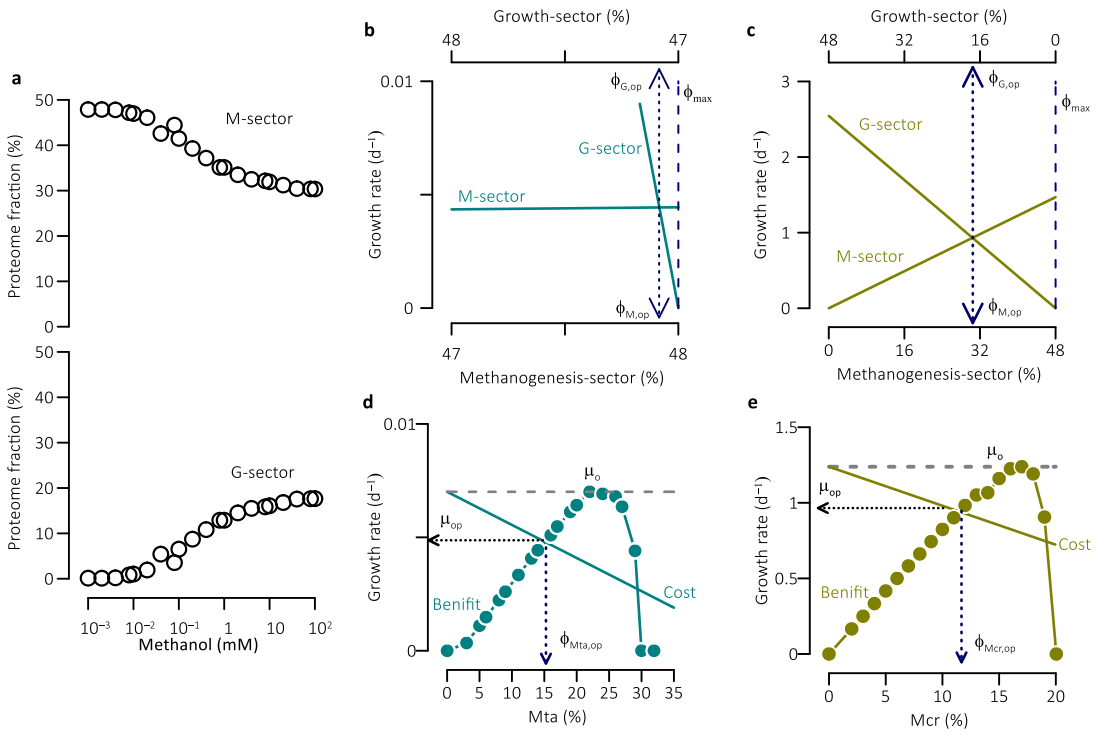

Figure S3 Expressions of methanogenesis enzymes are subject to the constraints of proteome partition and ribosome allocation. a. Variations with methanol concentration of acclimation in the optimal proteome fractions of the methanogenesis (M) and growth-related (G) sectors. b. Tug-of-war between the M and G sectors at acclimation concentration of 1 μM. Lines are calculated according to equation 15 and 16; ϕ_{max} is the sum of the proteome fractions of the M and G sectors; $\phi_{M,op}$ and $\phi_{G,op}$ represent the optimal proteome fractions of the M and G sectors, respectively; at these optimal fractions, growth rate is maximized and the fluxes through the enzyme reactions of methanogenesis balance those through biomass synthesis. c. Tug-of-war between the M and G sectors at acclimation concentration of 100 mM. d. Trade-off between the cost and benefit of ribosome allocation at 1 μM methanol of acclimation. The benefit function is constructed by sweeping the proteome fraction of Mta and then optimizing the rest methanogenesis enzymes. The cost function is calculated according to equation 19. $\phi_{Mta,op}$ is the optimal proteome fraction of Mta that balances the cost and benefit of ribosome allocation; ϕ_{op}

and ϕ_o represent the optimal growth rates with and without balancing the cost and benefit; e. Trade-off between the cost and benefit of allocating ribosomes to the synthesis of Mcr at 100 mM methanol of acclimation. $\phi_{Mcr,op}$ is the optimal proteome fraction of Mcr.

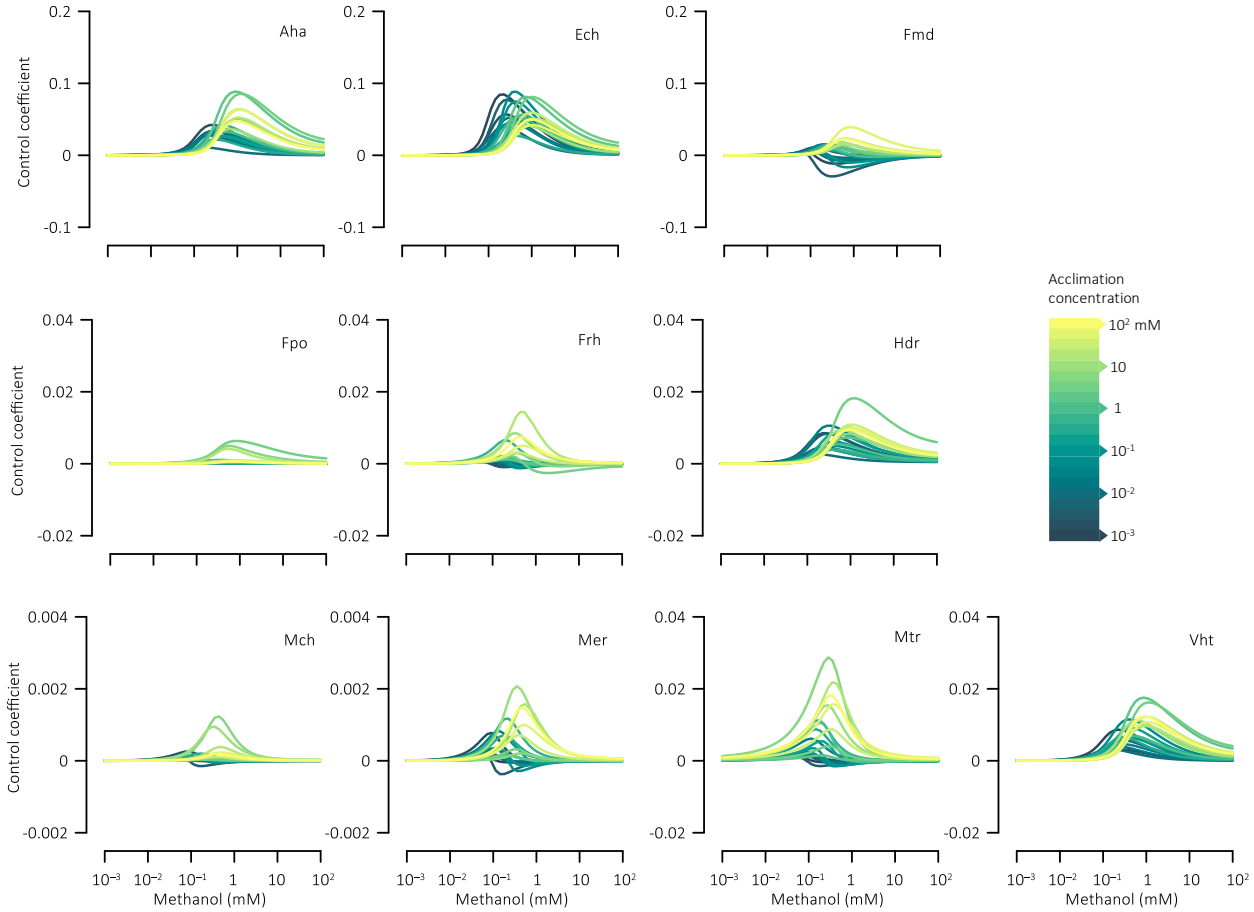

Figure S4 Variations with ambient methanol concentration in scaled control coefficients of methanogenesis enzymes. Lines are the results of performing MCA with the kinetic models constructed for different methanol concentrations of acclimation; the coefficients of Mcr and Mta are shown in figure 3; the coefficients of AcDh, Ftr, GerN, Mtd are within the range of $\pm 10^{-3}$ and are not shown.

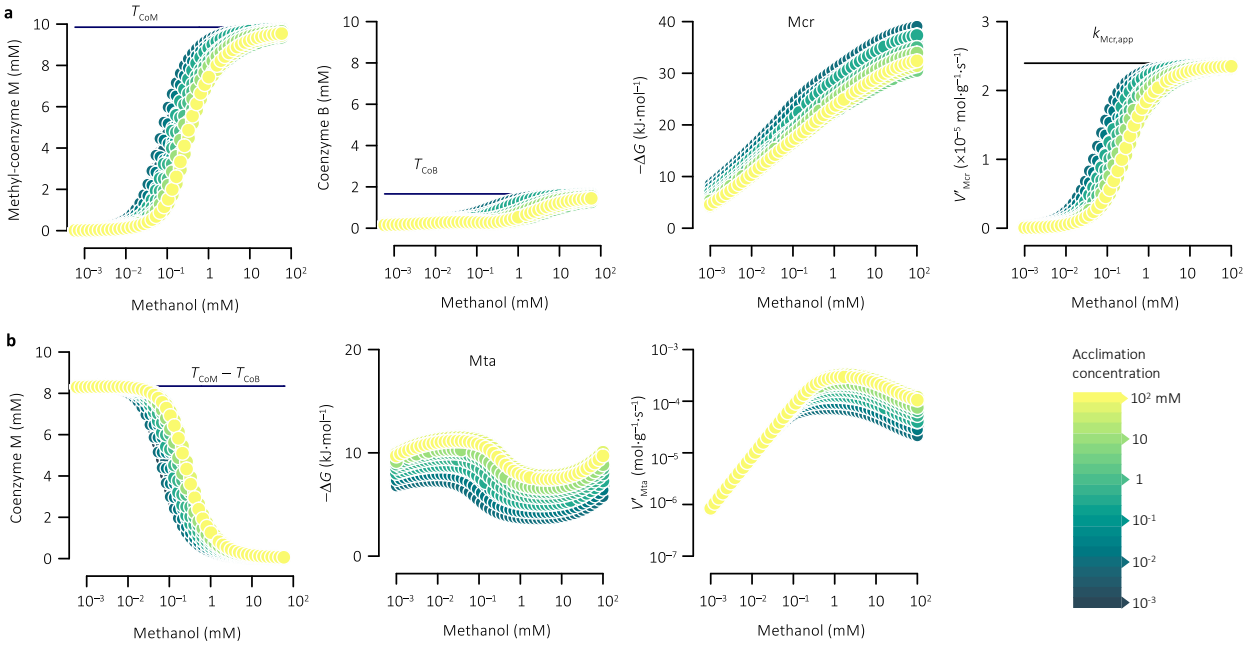
a
T_{CoM}
Methyl-coenzyme M (mM)
Methanol (mM)
T_{CoB}
Coenzyme B (mM)
Mcr
$-\Delta G$ (kJ·mol^{-1})
$k_{Mcr,app}$
V'_{Mcr} (×10^{-5} mol·g^{-1}·s^{-1})
b
$T_{CoM} - T_{CoB}$
Coenzyme M (mM)
Mta
V'_{Mta} (mol·g^{-1}·s^{-1})
Acclimation concentration
10^2 mM
10
1
10^{-1}
10^{-2}
10^{-3}

Figue S5 The reaction of Mcr displays zero-order kinetics at very high methanol concentrations, whereas Mta reaction shows first-order kinetics at very low methanol concentrations. a. Variations in the concentrations of methyl-coenzyme M and coenzyme B, the Gibbs free energy change of Mcr reaction, and the reaction velocity V'_{Mcr} per g Mcr. At very high methanol concentrations, Mcr reaction is zero-order with respect to methanol concentration; $k_{Mcr,app}$ is the apparent zero-order rate constant. b. Variations with methanol concentrations in coenzyme M concentration, the Gibbs free energy change of Mta reaction, and the reaction velocity V'_{Mta} per g Mta. At very low methanol concentrations, Mta reaction is first-order with respect to methanol concentration. The data points are the modeling results of the kinetic models calibrated for the different methanol concentrations of the acclimation; T_{coM} and T_{cob} are the intracellular concentrations of coenzyme M and B moieties, respectively.

APPENDIX B

CHAPTER III SUPPLEMENTARY INFORMATION AND FIGURES

This document describes the assumptions made in constructing the numerical model of reactive transport in sediments shown in Figure 4 of Wu, Guthrie, and Jin, "Bridging the gap: predicting microbial reaction rates in natural environments from laboratory observations."

The transport of a reacting component *A* — which might be acetate, bicarbonate, and methane — can be described by the equation

$$\frac{dC_A}{dt} = D_A\left(\frac{\partial^2 C_A}{\partial x^2} + \frac{\partial^2 C_A}{\partial y^2}\right) - V\frac{\partial C_A}{\partial x} + \frac{r_A}{\phi} \quad (1)$$

Here, concentration C_A is carried in mol per cm^{-3} fluid, D_A is the diffusion coefficient ($cm^2\ s^{-1}$), x and y is the length and width of the sediment bed (cm), r_A is the rate (mol $cm^{-3}\ s^{-1}$) at which A is added to (positive) or removed from (negative) the pore fluid by methanogenesis reactions, expressed per cm^3 of fluid-saturated sediment, and ϕ is sediment porosity.

We considered a sediment bed of 40 cm wide and 80 cm long, divided into 300×800 nodal blocks. Fluid containing 10 mmolal acetate, 20 mmolal bicarbonate, and 0.2 μmolal methane flows from the left to the right of the sediment bed at a velocity of 0.125 m d^{-1}. We took temperature in the sediments to be 25°C, set porosity to 0.9, and fixed pH to 7. We set a diffusion coefficient of $6\times10^{-6}\ cm^2\ s^{-1}$. We seeded each nodal block with an initial biomass concentration of $1.0\pm0.5\times10^{-8}$ g cm^{-3} for both *Methanosarcina* and *Methanosaeta*. To account for the variations in the reported kinetic parameters, we assign

the parameter values by sampling randomly from the 95% confidence intervals of the laboratory values. We set the initial concentrations for the reacting species same as those in the fluid that recharge the sediment bed from the left, including. Table X lists the values assumed in the simulation for the kinetic parameters.

APPENDIX C

CHAPTER IV SUPPLEMENTARY INFORMATION AND FIGURES

Introduction

[This supporting information contains one text, 14 figure, and 4 tables as well as a dataset, which will upload separately as ds01. The dataset is a collection of reported temperature sensitivity of anoxic methane (sheet1) and carbon dioxide production (sheet2); corresponding references are listed in sheet 3.]

Text S1. Rate equation of extracellular enzymes

Following the Michaelis-Menten equation, the reaction rate r_E of extracellular enzymes [mol·(kg water)$^{-1}$·s^{-1}, or simply mol·kg^{-1}·s^{-1}] is

$$r_E = k_E \cdot [E] \cdot \frac{m_{SOM}}{m_{SOM} + K_{SOM}} \quad \textbf{(1)}$$

where k_E is the rate constant (s^{-1}), [E] is enzyme concentration (the weight (g) of extracellular enzyme per kg water (g·kg^{-1})), m_{SOM} is the mole amount of SOM per kg water (or mol·kg^{-1}), and K_{SOM} is the Michaelis constant. Extracellular enzymes are synthesized by fermenting microbes. We assume that the rates r_E^+ of enzyme synthesis depend linearly on the biomass concentrations of fermenting microbes, but are inhibited by the accumulation of DOC. Accordingly, we calculate the enzyme synthesis rates according to

$$r_E^+ = k_{XE} \cdot [X_F] \cdot \max\left(1 - \frac{m_{DOC}}{m_{DOC}^o}, 0\right) \quad \textbf{(2)}$$

where k_{XE} is the rate constant, $[X_F]$ and m_{DOC} are the concentrations of fermenter biomass and DOC, respectively, and m^{o}_{DOC} is the concentration of DOC above which fermenters stop synthesizing extracellular enzyme. At the same time, enzymes undergo degradation and spontaneous decay, which reduces the concentrations,

$$r_E^- = D_E \cdot [E] \quad \textbf{(3)}$$

Here r_E^- is the rate of decay, and D_E is the decay coefficient. We assume the synthesis and decay balance each other, or the rate of enzyme synthesis takes the same value as the rate of enzyme attrition. As a result, enzyme concentration [E] can be calculated according to

$$[E] = c \cdot [X_F] \cdot \max\left(1 - \frac{m_{DOC}}{m^{o}_{DOC}}, 0\right), \quad \textbf{(4)}$$

where $c = k_{XE} \cdot D_E^{-1}$, a dimensionless coefficient that represents the turnover rate of extracellular enzyme.

In the laboratory experiments of Ye et al. (2016), the amount of SOM decomposed by microbes was relatively small, <1%, compared to the total SOM. In their reactors, they added 0.7 g dry soil to make 24 g slurries. Assuming an organic carbon content of 42% (Bridgham et al., 1998), the concentration of SOM in the slurry is approximately 1.68 molal. During the incubation, microbes consumed about 0.3 mM SOM, which amount to ~1‰ of SOM at the beginning of the incubations. Therefore changes in SOM concentrations are relatively insignificant.

Substituting equation 4 to 1 and by neglecting the impact of SOM concentrations,

$$r_E = k_{app} \cdot [X_F] \cdot \max\left(1 - \frac{m_{DOC}}{m^{o}_{DOC}}, 0\right) \quad \textbf{(5)}$$

where k_{app} is the apparent rate constant,

$$k_{app} = k_E \cdot c \cdot \frac{m_{SOM}}{m_{SOM} + K_{SOM}}. \quad (6)$$

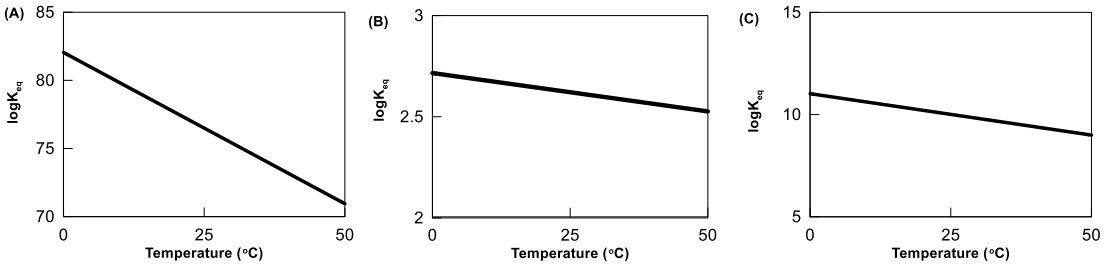

Figure S1. Variations with temperature in the logarithm of equilibrium constant (log K) of fermentation (eq. 17), acetoclastic (eq. 6) and hydrogenotrophic methanogenesis reaction (eq. 7). The log K values are calculated using software package Supcrt92 (Johnson et al., 1992).

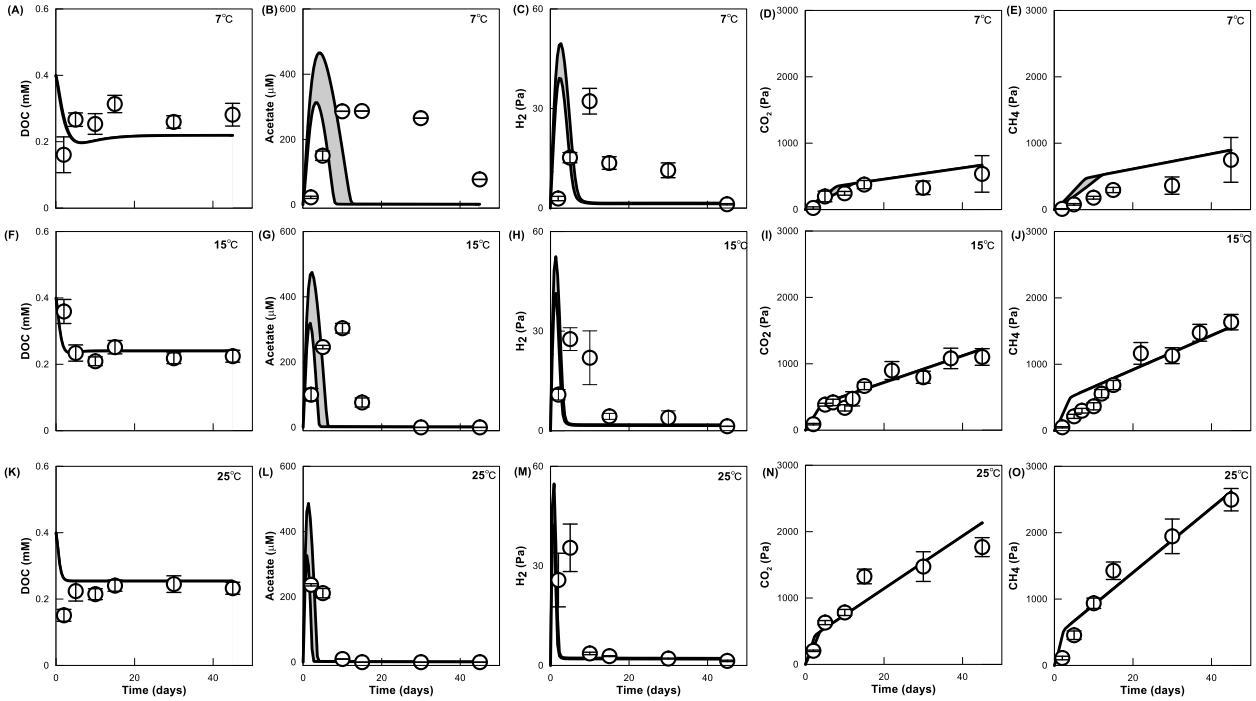

Figure S2 T_{min} = -10°C, parameter estimation by fitting the modeling results to the variations with time in the concentrations of DOC (A, F, K), acetate (B, G, L), H_2 (C, H,

M), CO_2 (D, I, N), and CH_4 (E, J, O) in the experiments of organic matter decomposition with glucose amendment at 7, 15 and 25℃. Data points are the experimental observations of Ye et al. (2016); error bars show the 95% confidence interval of the observations; solid lines are the simulation results; shaded areas are the simulation results by using the minimum and maximum initial biomass concentrations.

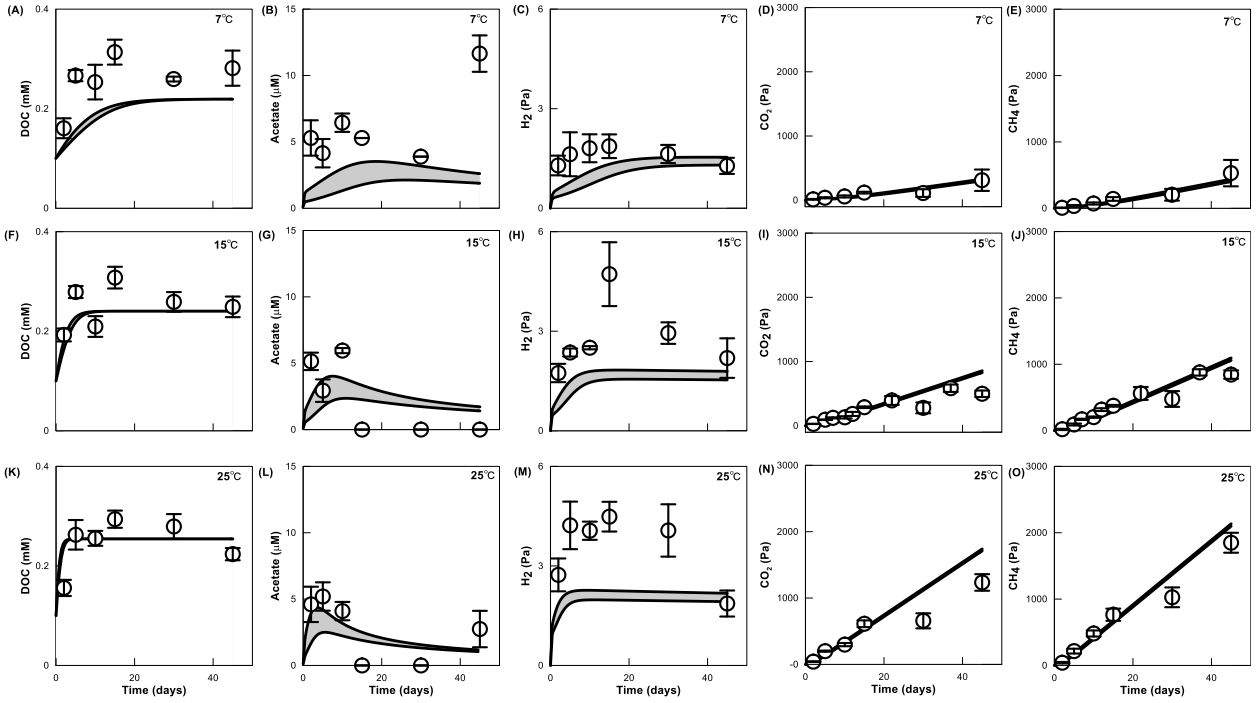

Figure S3 Application of the calibrated biogeochemical reaction model where T_{min} = -10℃ to the experiments of organic matter decomposition without glucose amendment at 7, 15 and 25℃. Data points are the concentrations of DOC (A, F, K), acetate (B, G, L), H_2 (C, H, M), CO_2 (D, I, N), and CH_4 (E, J, O) reported by Ye et al. (2016); error bars show the 95% confidence interval of the observations; solid lines are the simulation results; shaded areas are the simulation results by using the minimum and maximum initial biomass

concentrations..

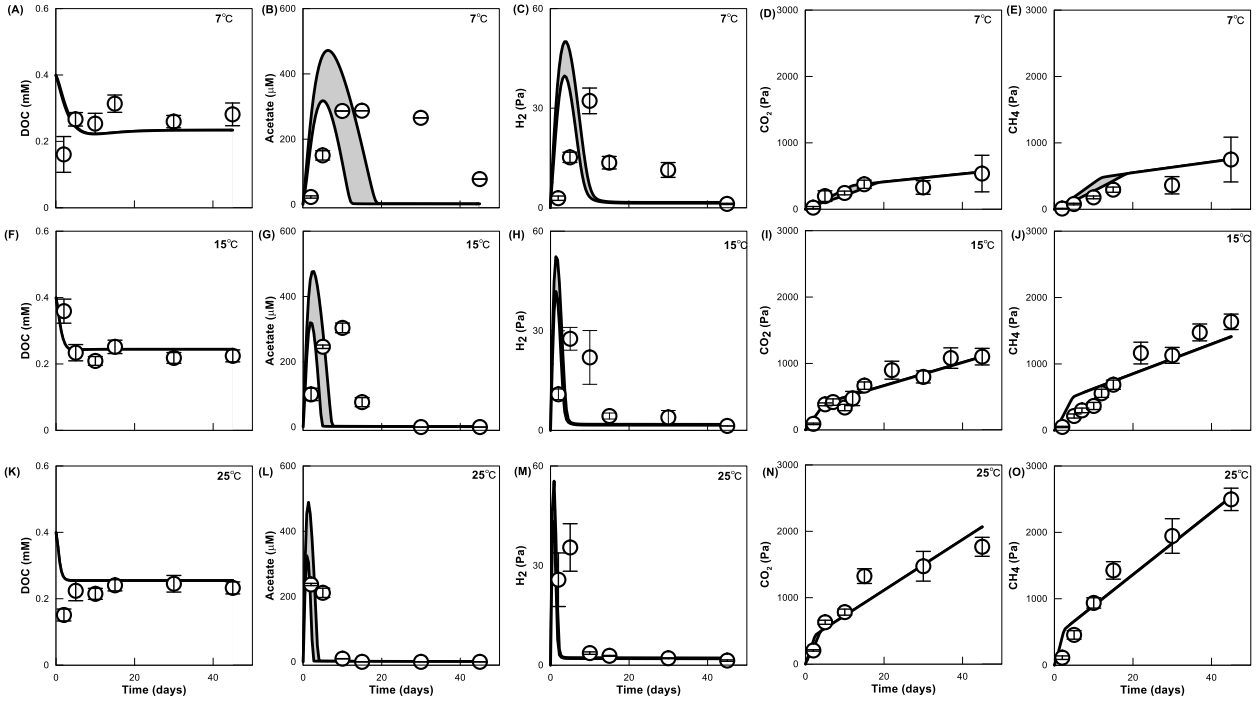

Figure S4 T_{min} = -5℃, parameter estimation by fitting the modeling results to the variations with time in the concentrations of DOC (A, F, K), acetate (B, G, L), H_2 (C, H, M), CO_2 (D, I, N), and CH_4 (E, J, O) in the experiments of organic matter decomposition with glucose amendment at 7, 15 and 25℃. Data points are the experimental observations of Ye et al. (2016); error bars show the 95% confidence interval of the observations; solid lines are the simulation results; shaded areas are the simulation results by using the minimum and maximum initial biomass concentrations.

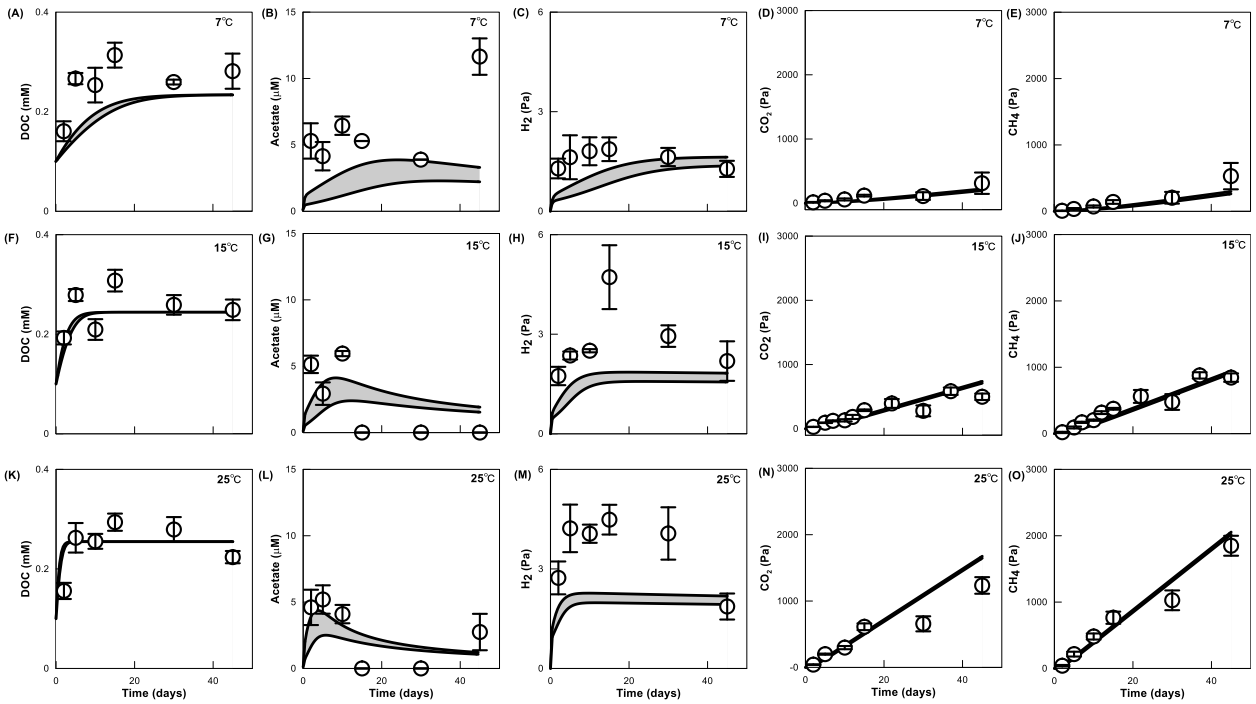

Figure S5 Application of the calibrated biogeochemical reaction model where T_{min} = -5°C to the experiments of organic matter decomposition without glucose amendment at 7, 15 and 25°C. Data points are the concentrations of DOC (A, F, K), acetate (B, G, L), H_2 (C, H, M), CO_2 (D, I, N), and CH_4 (E, J, O) reported by Ye et al. (2016); error bars show the 95% confidence interval of the observations; solid lines are the simulation results; shaded areas are the simulation results by using the minimum and maximum initial biomass concentrations.

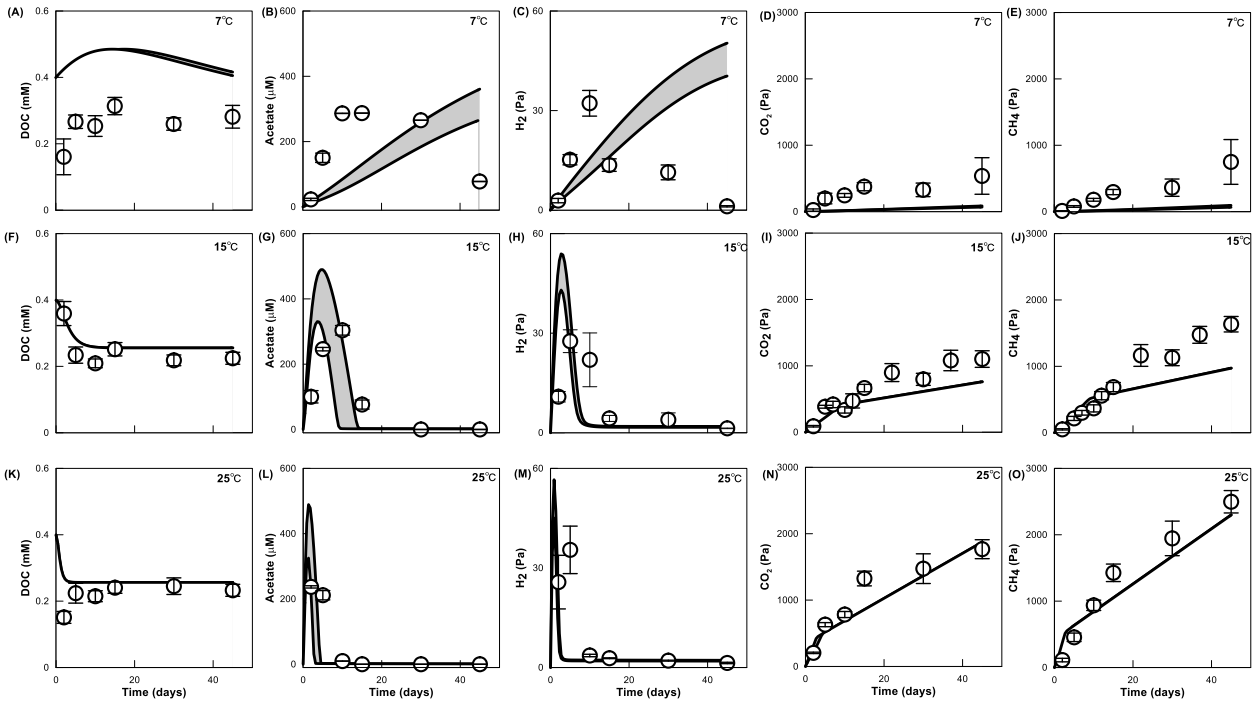

Figure S6 T_{min} = 5°C, parameter estimation by fitting the modeling results to the variations with time in the concentrations of DOC (A, F, K), acetate (B, G, L), H_2 (C, H, M), CO_2 (D, I, N), and CH_4 (E, J, O) in the experiments of organic matter decomposition with glucose amendment at 7, 15 and 25°C. Data points are the experimental observations of Ye et al. (2016); error bars show the 95% confidence interval of the observations; solid lines are the simulation results; shaded areas are the simulation results by using the minimum and maximum initial biomass concentrations.

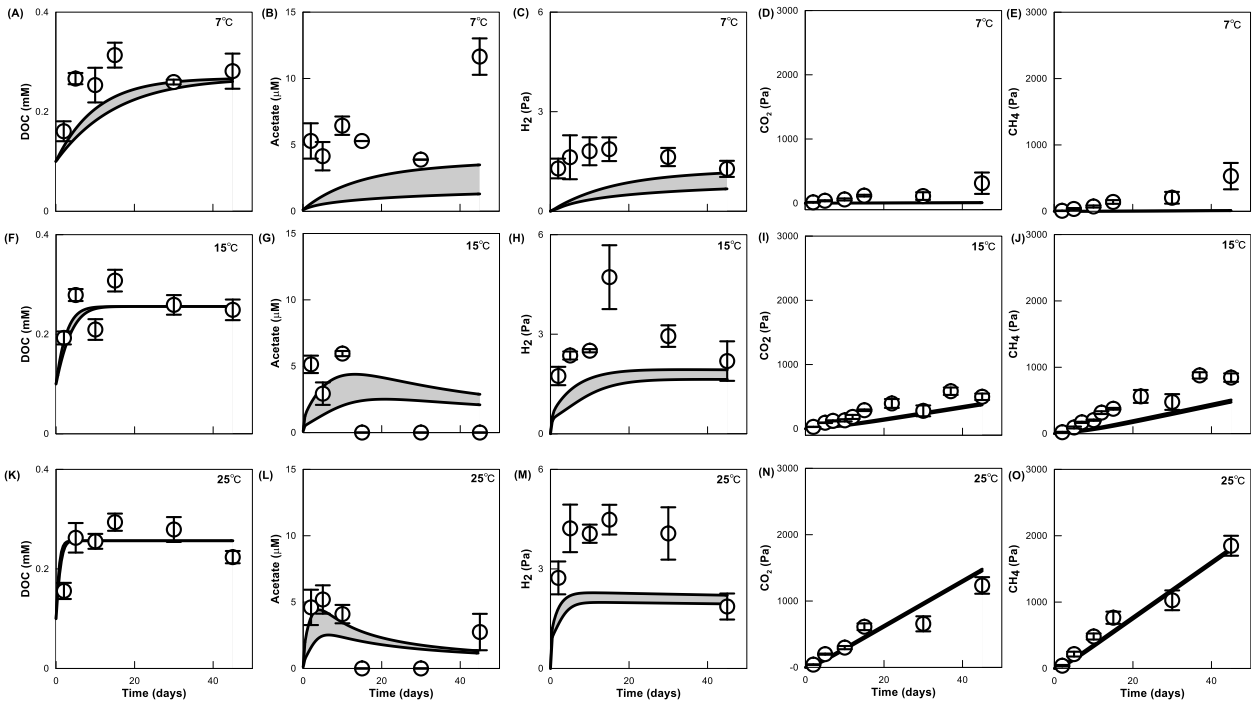

Figure S7 Application of the calibrated biogeochemical reaction model where T_{min} = 5℃ to the experiments of organic matter decomposition without glucose amendment at 7, 15 and 25℃. Data points are the concentrations of DOC (A, F, K), acetate (B, G, L), H_2 (C, H, M), CO_2 (D, I, N), and CH_4 (E, J, O) reported by Ye et al. (2016); error bars show the 95% confidence interval of the observations; solid lines are the simulation results; shaded areas are the simulation results by using the minimum and maximum initial biomass concentrations.

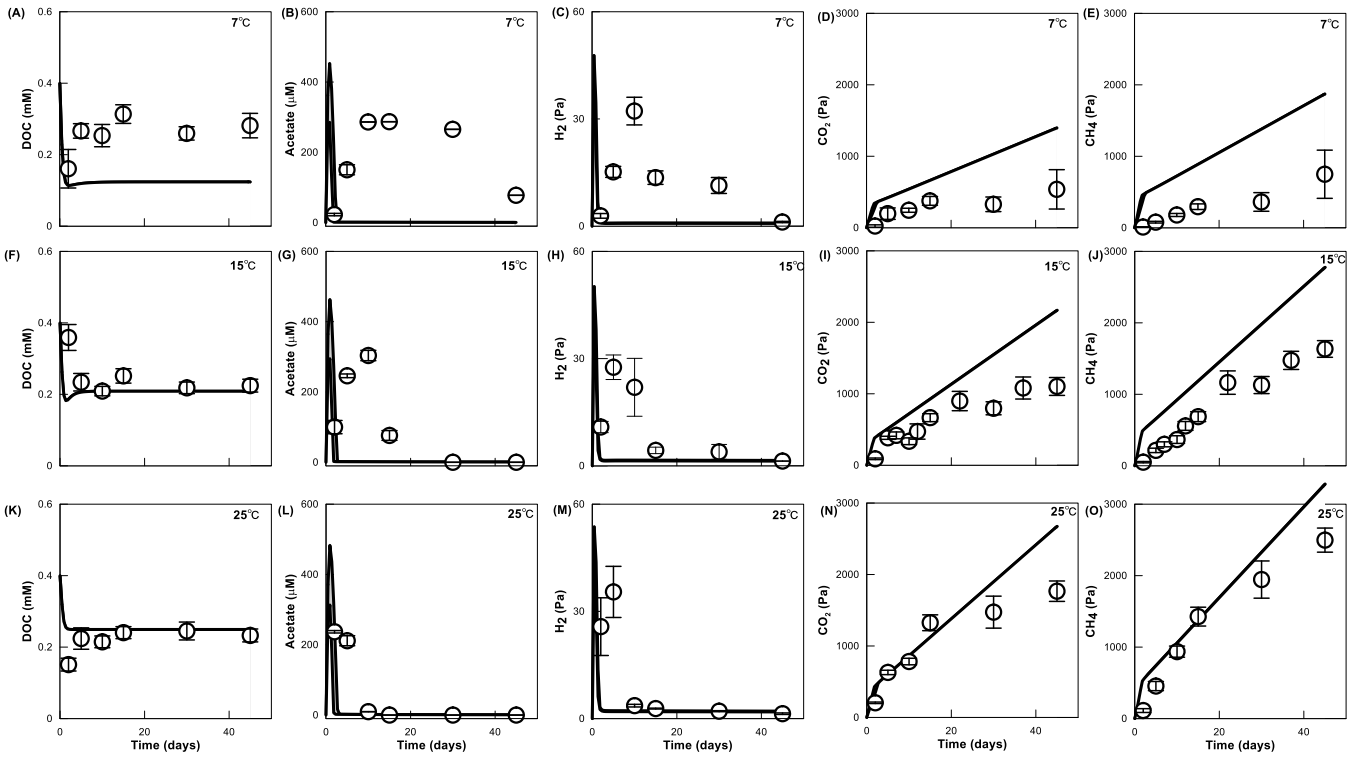

Figure S8 T_{opt}= 30°C, parameter estimation by fitting the modeling results to the variations with time in the concentrations of DOC (A, F, K), acetate (B, G, L), H_2 (C, H, M), CO_2 (D, I, N), and CH_4 (E, J, O) in the experiments of organic matter decomposition with glucose amendment at 7, 15 and 25°C. Data points are the experimental observations of Ye et al. (2016); error bars show the 95% confidence interval of the observations; solid lines are the simulation results.

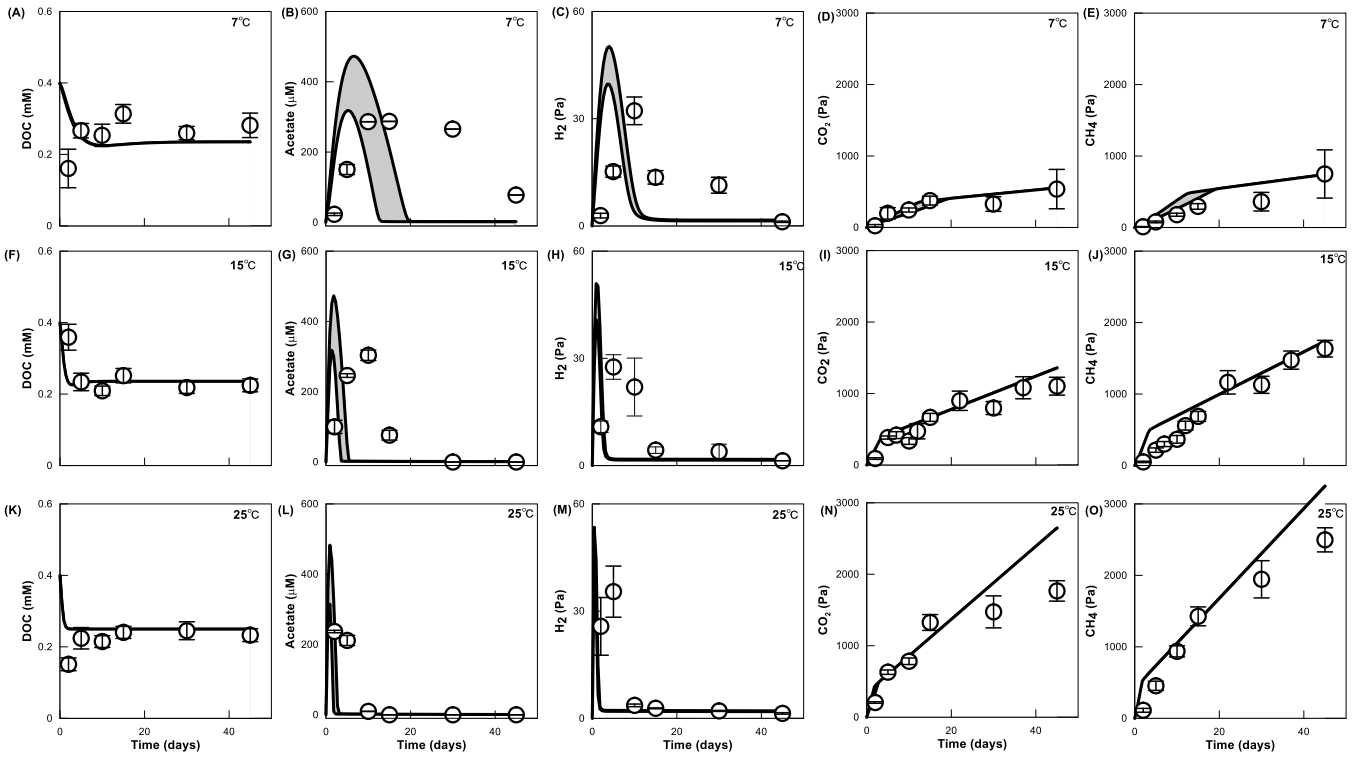

Figure S9 T_{opt}= 33℃, parameter estimation by fitting the modeling results to the variations with time in the concentrations of DOC (A, F, K), acetate (B, G, L), H_2 (C, H, M), CO_2 (D, I, N), and CH_4 (E, J, O) in the experiments of organic matter decomposition with glucose amendment at 7, 15 and 25℃. Data points are the experimental observations of Ye et al. (2016); error bars show the 95% confidence interval of the observations; solid lines are the simulation results.

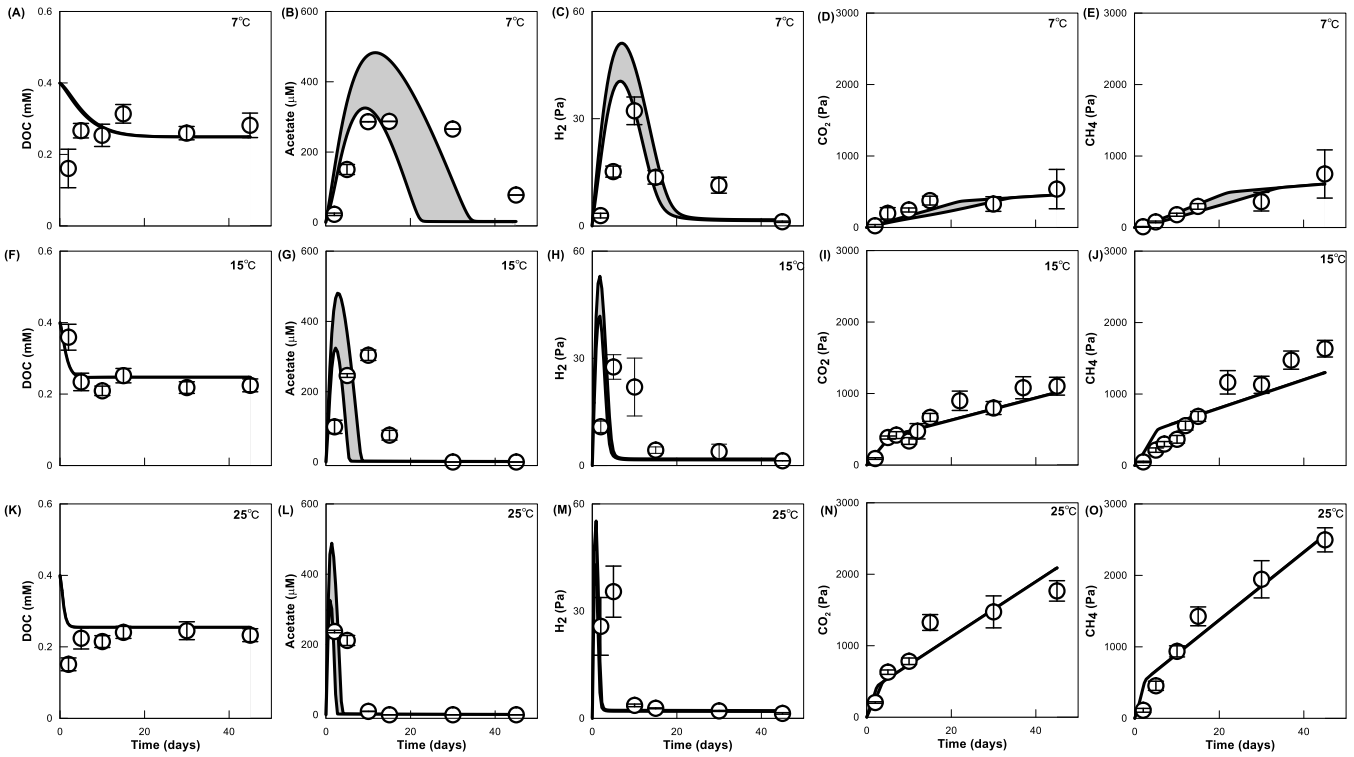

Figure S10 T_{opt}= 36℃, parameter estimation by fitting the modeling results to the variations with time in the concentrations of DOC (A, F, K), acetate (B, G, L), H_2 (C, H, M), CO_2 (D, I, N), and CH_4 (E, J, O) in the experiments of organic matter decomposition with glucose amendment at 7, 15 and 25℃. Data points are the experimental observations of Ye et al. (2016); error bars show the 95% confidence interval of the observations; solid lines are the simulation results.

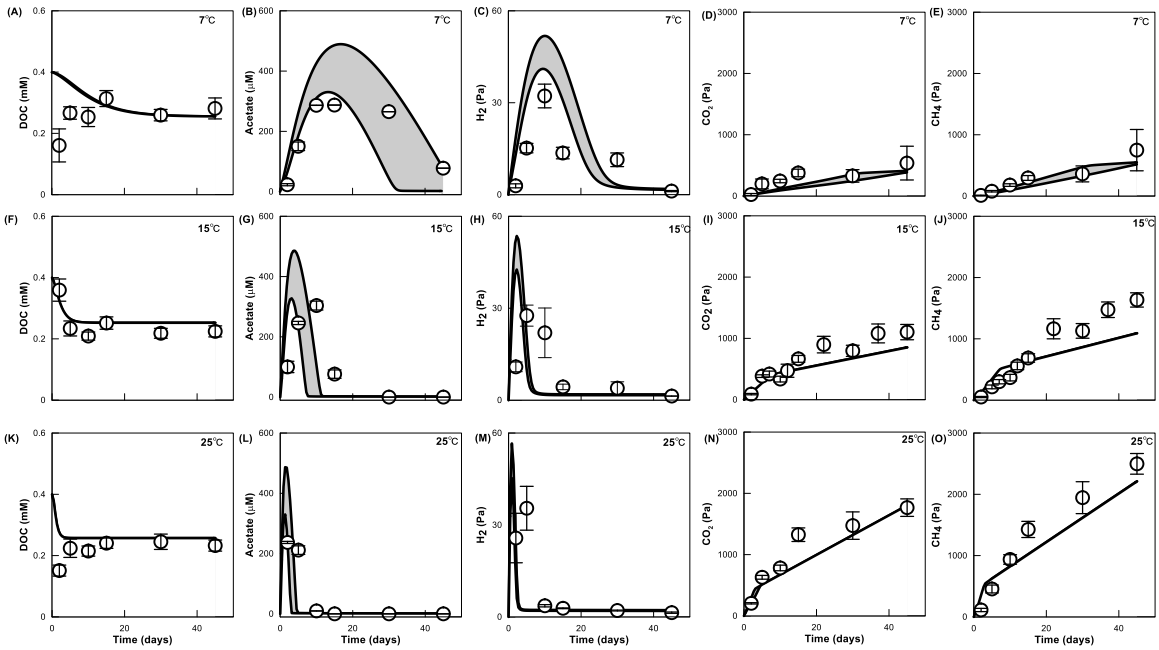

Figure S11 T_{opt}= 39℃, parameter estimation by fitting the modeling results to the variations with time in the concentrations of DOC (A, F, K), acetate (B, G, L), H_2 (C, H, M), CO_2 (D, I, N), and CH_4 (E, J, O) in the experiments of organic matter decomposition with glucose amendment at 7, 15 and 25℃. Data points are the experimental observations of Ye et al. (2016); error bars show the 95% confidence interval of the observations; solid lines are the simulation results.

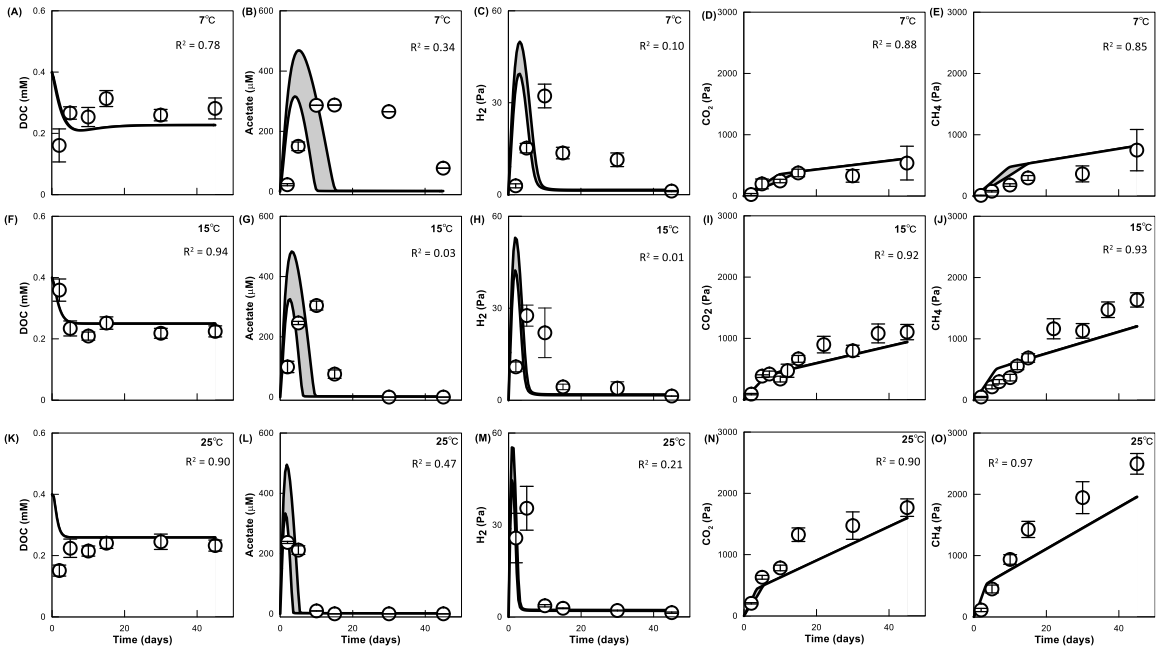

Figure S12 Parameter estimation by fitting the Arrhenius equation of microbial reactions to the variations with time in the concentrations of DOC (A, F, K), acetate (B, G, L), H_2 (C, H, M), CO_2 (D, I, N), and CH_4 (E, J, O) in the experiments of organic matter decomposition with glucose amendment at 7, 15 and 25°C. Data points are the experimental observations of Ye et al. (2016); error bars show the 95% confidence interval of the observations; solid lines are the simulation results; shaded areas are the simulation results by using the minimum and maximum initial biomass concentrations.

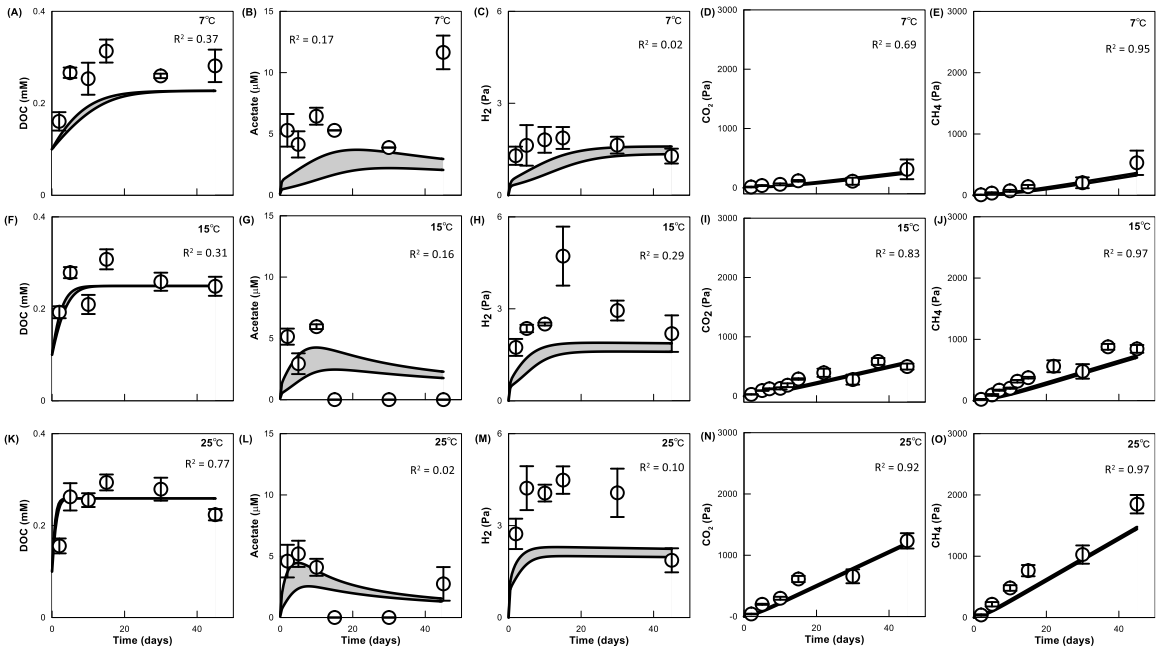

Figure S13 Application of the calibrated biogeochemical reaction model from Arrhenius equation to the experiments of organic matter decomposition without glucose amendment at 7, 15 and 25°C. Data points are the concentrations of DOC (A, F, K), acetate (B, G, L), H_2 (C, H, M), CO_2 (D, I, N), and CH_4 (E, J, O) reported by Ye et al. (2016); error bars show the 95% confidence interval of the observations; solid lines are the simulation results; shaded areas are the simulation results by using the minimum and maximum initial biomass concentrations.

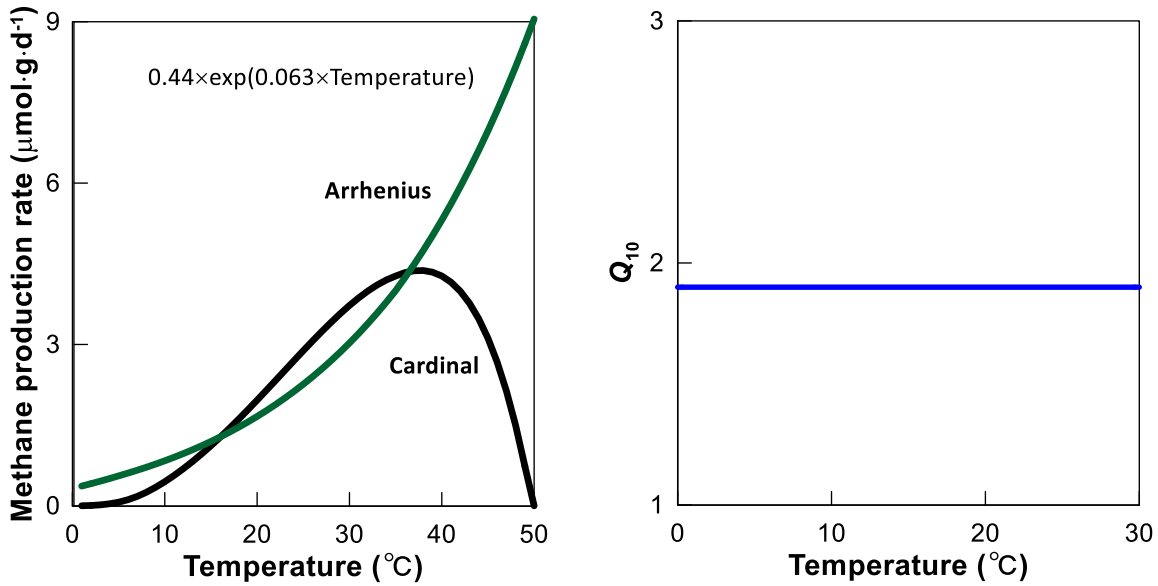

Figure S14 Variations in methane production rate with temperature (A) and changes of Q10 from simulation results from Arrhenius equation with temperature (B). In panel A , the green line is simulation result from Arrhenius equation, and black line is the simulation result from Cardinal temperature equation.

Table S1. One-way ANOVA analysis of the effect of climate zones on the Q_{10} of methane production

	df	sum_sq	mean_sq	F	PR(>F)
treatments	2	156.6137	78.30686	3.637274	0.028393
Residual	170	3659.929	21.52899	-	-

Table S2. Pairwise comparison of the Q10 of methane production across climate zones

	A	B	mean(A)	T	p-tukey	hedges
0	cold_ch4	temperate_ch4	5.037931	1.908315	0.136901	0.319672
1	cold_ch4	warm_ch4	5.037931	-0.90592	0.647247	-0.21473
2	temperate_ch4	warm_ch4	3.547	-2.38001	0.046074	-0.53449

Table S3. One-ANOVA analysis of the effect of climate zones on the Q10 of anaerobic CO2 production

	df	sum_sq	mean_sq	F	PR(>F)

treatments	2	176.023	88.01149	3.899577	0.023248
Residual	105	2369.797	22.5695	-	-

Table S4. Pairwise comparison of the Q10 of anaerobic CO2 production across climate zones

	A	B	mean(A)	T	p-tukey	hedges
0	cold_co2	temperate_co2	5.01537	2.018352	0.108836	0.446239
1	cold_co2	warm_co2	5.01537	2.485633	0.035235	0.622295
2	temperate_co2	warm_co2	2.87625	0.644209	0.77507	0.175832

REFERENCES CITED

Allison, S. D., Wallenstein, M. D., & Bradford, M. A. (2010). Soil-carbon response to warming dependent on microbial physiology. *Nature Geoscience*, *3*(5), 336–340. https://doi.org/10.1038/ngeo846

AlMulla, A., Jones, D., & Roberts, P. (2018). Substrate influences temperature sensitivity of dissolved organic carbon (DOC) and nitrogen (DON) mineralization in arid agricultural soils. *Soil Systems*, *2*(2), 28. https://doi.org/10.3390/soilsystems2020028

Alster, C. J., Baas, P., Wallenstein, M. D., Johnson, N. G., & von Fischer, J. C. (2016). Temperature sensitivity as a microbial trait using parameters from macromolecular rate theory. *Frontiers in Microbiology*, *7*(NOV), 1–10. https://doi.org/10.3389/fmicb.2016.01821

Auffret, M. D., Karhu, K., Khachane, A., Dungait, J. A. J., Fraser, F., Hopkins, D. W., et al. (2016). The Role of Microbial Community Composition in Controlling Soil Respiration Responses to Temperature. *PLoS ONE*, *11*(10), 1–19. https://doi.org/10.1371/journal.pone.0165448

Avery, G. B., Shannon, R. D., White, J. R., Christopher, S., Alperin, M. J., Jr, G. B. A., & Jeffrey, R. (2003). Production via acetate fermentation and CO2 reduction controls on methane production in a tidal freshwater estuary and a peatland : methane production via acetate fermentation and CO, reduction. *Production*, *62*(1), 19–37. Retrieved from https://link.springer.com/article/10.1023/A:1021128400602

Bakker, B. M., Walsh, M. C., Ter Kuile, B. H., C Mensonides, F. I., M Michels, P. A., Opperdoes, F. R., & Westerhoff, H. V. (1999). *Contribution of glucose transport to the control of the glycolytic flux in Trypanosoma brucei*. *Biochemistry* (Vol. 96). Retrieved from www.pnas.org.

Bardgett, R. D., Freeman, C., & Ostle, N. J. (2008). Microbial contributions to climate change through carbon cycle feedbacks. *ISME Journal*, *2*(8), 805–814. https://doi.org/10.1038/ismej.2008.58

Bauchop, T., & Elsden, S. R. (1960). The growth of micro-organisms in relation to their energy supply. *Journal of General Microbiology*, *23*, 457–469. https://doi.org/10.1099/00221287-23-3-457

Bäumer, S., Ide, T., Jacobi, C., Johann, A., Gottschalk, G., & Deppenmeier, U. (2000). The F420H2 dehydrogenase from Methanosarcina mazei is a redox-driven proton pump closely related to NADH dehydrogenases. *Journal of Biological Chemistry*, *275*(24), 17968–17973. https://doi.org/10.1074/jbc.M000650200

Benedict, M. N., Gonnerman, M. C., Metcalf, W. W., & Price, N. D. (2012). Genome-scale metabolic reconstruction and hypothesis testing in the methanogenic archaeon Methanosarcina acetivorans C2A. *Journal of Bacteriology*, *194*(4), 855–865. https://doi.org/10.1128/JB.06040-11

Bennett, B. D., Kimball, E. H., Gao, M., Osterhout, R., Van Dien, S. J., & Rabinowitz, J. D. (2009). Absolute metabolite concentrations and implied enzyme active site occupancy in Escherichia coli. *Nature Chemical Biology*, *5*(8), 593–599. https://doi.org/10.1038/nchembio.186

Berghuis, B. A., Yu, F. B., Schulz, F., Blainey, P. C., Woyke, T., & Quake, S. R. (2019). Hydrogenotrophic methanogenesis in archaeal phylum Verstraetearchaeota reveals the shared ancestry of all methanogens. *Proceedings of the National Academy of Sciences of the United States of America*, *116*(11), 5037–5044. https://doi.org/10.1073/pnas.1815631116

Bergman, I., Svensson, B. H., & Nilsson, M. (1998). Regulation of methane production in a swedish acid mire by pH, temperature and substrate. *Soil Biology and Biochemistry*, *30*(6), 729–741. https://doi.org/10.1016/S0038-0717(97)00181-8

Berkhout, J., Bosdriesz, E., Nikerel, E., Molenaar, D., Dick De Ridder, †, Teusink, B., & Bruggeman, F. J. (2013). How Biochemical Constraints of Cellular Growth Shape Evolutionary Adaptations in Metabolism. *Genetics*, *194*, 505–512. https://doi.org/10.1534/genetics.113.150631

Bethke, C. M. (2008). *Geochemical and biogeochemical reaction modeling*. Cambridge University Press.

Blake, L. I., Tveit, A., Øvreås, L., Head, I. M., & Gray, N. D. (2015). Response of methanogens in arctic sediments to temperature and methanogenic substrate availability. *PLoS ONE*, *10*(6), 1–18. https://doi.org/10.1371/journal.pone.0129733

Blaut, M., & Gottschalk, G. (1984). Coupling of ATP synthesis and methane formation from methanol and molecular hydrogen in, *222*, 217–222.

Bomberg, M., Montonen, L., Münster, U., & Jurgens, G. (2008). Diversity and function of archaea in freshwater habitats. *Current Trends in Microbiology*, *4*(July 2014), 1–89. Retrieved from http://www.researchtrends.net/tia/abstract.asp?in=0&vn=4&tid=41&aid=2693&pub=2008&type=3

Bridgham, S. D., Updegraff, K., & Pastor, J. (1998). Carbon, nitrogen, and phosphorus mineralization in northern wetlands. *Ecology*, *79*(5), 1545–1561. https://doi.org/10.1890/0012-9658(1998)079[1545:CNAPMI]2.0.CO;2

Brown, J. H., Gillooly, J. F., Allen, A. P., Savage, V. M., & West, G. B. (2004). *TOWARD A METABOLIC THEORY OF ECOLOGY*. *Ecology* (Vol. 85).

Brown, J. H., Hall, C. A. S., & Sibly, R. M. (2018). Equal fitness paradigm explained by a trade-off between generation time and energy production rate. *Nature Ecology and Evolution*, *2*(2), 262–268. https://doi.org/10.1038/s41559-017-0430-1

Buckel, W., & Thauer, R. K. (2013). Energy conservation via electron bifurcating ferredoxin reduction and proton/Na+ translocating ferredoxin oxidation. *Biochimica et Biophysica Acta - Bioenergetics*, *1827*(2), 94–113. https://doi.org/10.1016/j.bbabio.2012.07.002

Button, D. K. (1998). Nutrient Uptake by Microorganisms according to Kinetic Parameters from Theory as Related to Cytoarchitecture. *Microbiology and Molecular Biology Reviews*, *62*(3), 636–645. https://doi.org/10.1128/mmbr.62.3.636-645.1998

Chadwick, G. L., Hemp, J., Fischer, W. W., & Orphan, V. J. (2018). Convergent evolution of unusual complex I homologs with increased proton pumping capacity: energetic and ecological implications. *ISME Journal*, *12*(11), 2668–2680. https://doi.org/10.1038/s41396-018-0210-1

Charlton, S. R., & Parkhurst, D. L. (2011). Modules based on the geochemical model PHREEQC for use in scripting and programming languages. *Computers and Geosciences*, *37*(10), 1653–1663. https://doi.org/10.1016/j.cageo.2011.02.005

Ciais, P., Sabine, C., Bala, G., Bopp, L., Brovkin, V., Canadell, J., et al. (2013). The physical science basis. Contribution of working group I to the fifth assessment report of the intergovernmental panel on climate change. *Change, IPCC Climate*, 465–570. https://doi.org/10.1017/CBO9781107415324.015

Clarens, M., & Moletta, R. (1990). Kinetic studies of acetate fermentation by Methanosarcina sp. MSTA-1. *Applied Microbiology and Biotechnology*, *33*, 239–244.

Conklin, A., Stensel, H. D., & Ferguson, J. (2006). Growth Kinetics and Competition Between Methanosarcina and Methanosaeta in Mesophilic Anaerobic Digestion. *Water Environment Research*, *78*(5), 486–496. https://doi.org/10.2175/106143006x95393

Davidi, D., Noor, E., Liebermeister, W., Bar-Even, A., Flamholz, A., Tummler, K., et al. (2016). Global characterization of in vivo enzyme catalytic rates and their correspondence to in vitro k cat measurements. *PNAS*, *113*(12), 3401–3406. https://doi.org/10.1073/pnas.1514240113

Davidson, E. A., & Janssens, I. A. (2006). Temperature sensitivity of soil carbon decomposition and feedbacks to climate change. *Nature*, *440*(7081), 165–173. https://doi.org/10.1177/014662168400800309

Dekel, E., & Alon, U. (2005). Optimality and evolutionary tuning of the expression level of a protein. https://doi.org/10.1038/nature03842

DeLong, J. P., Gibert, J. P., Luhring, T. M., Bachman, G., Reed, B., Neyer, A., & Montooth, K. L. (2017). The combined effects of reactant kinetics and enzyme stability explain the temperature dependence of metabolic rates. *Ecology and Evolution*, *7*(11), 3940–3950. https://doi.org/10.1002/ece3.2955

Du, B., Zielinski, D. C., Monk, J. M., & Palsson, B. O. (2018). Thermodynamic favorability and pathway yield as evolutionary tradeoffs in biosynthetic pathway choice. *Proceedings of the National Academy of Sciences of the United States of America*, *115*(44), 11339–11344. https://doi.org/10.1073/pnas.1805367115

Dunfield, P. F., & Conrad, R. (2000). Starvation alters the apparent half-saturation constant for methane in the type II methanotroph Methylocystis strain LR1. *Applied and Environmental Microbiology*, *66*(9), 4136–4138. https://doi.org/10.1128/AEM.66.9.4136-4138.2000

Dykhuizen, D. E., Dean, A. M., & Hartl, D. L. (1987). Metabolic flux and fitness. *Genetics*, *115*(1), 25–31. https://doi.org/10.1093/genetics/115.1.25

Enoki, M., Shinzato, N., Sato, H., Nakamura, K., & Kamagata, Y. (2011). Comparative Proteomic Analysis of Methanothermobacter themautotrophicus DH in Pure Culture and in Co-Culture with a Butyrate-Oxidizing Bacterium. *PLoS ONE*, *6*(8), 24309. https://doi.org/10.1371/journal.pone.0024309

van Eunen, K., Kiewiet, J. A. L., Westerhoff, H. V., & Bakker, B. M. (2012). Testing biochemistry revisited: How in vivo metabolism can be understood from in vitro enzyme kinetics. *PLoS Computational Biology*, *8*(4). https://doi.org/10.1371/journal.pcbi.1002483

Ewald, J., Bartl, M., & Kaleta, C. (2017). Deciphering the regulation of metabolism with dynamic optimization: an overview of recent advances. *Biochemical Society Transactions*, *45*(4), 1035–1043.

Eyring, H. (1935). The Activated Complex in Chemical Reactions, *3(2)*(November 1934), 107–115.

Feist, A. M., Scholten, J. C. M., Palsson, B., Brockman, F. J., & Ideker, T. (2006). Modeling methanogenesis with a genome-scale metabolic reconstruction of Methanosarcina barkeri. *Molecular Systems Biology*, *2*, 1–14. https://doi.org/10.1038/msb4100046

Fell, D. A. (1992). Metabolic control analysis: A survey of its theoretical and experimental development. *Biochemical Journal*. https://doi.org/10.1042/bj2860313

Feller, G. (2010). Protein stability and enzyme activity at extreme biological temperatures. *Journal of Physics Condensed Matter*, *22*(32). https://doi.org/10.1088/0953-8984/22/32/323101

Ferenci, T. (1999, September 1). "Growth of bacterial cultures" 50 years on: Towards an uncertainty principle instead of constants in bacterial growth kinetics. *Research in Microbiology*. Elsevier Masson SAS. https://doi.org/10.1016/S0923-2508(99)00114-X

Fey, A., & Conrad, R. (2003). Effect of temperature on the rate limiting step in the methanogenic degradation pathway in rice field soil. *Soil Biology and Biochemistry*, *35*(1), 1–8. https://doi.org/10.1016/S0038-0717(02)00175-X

Fiksen, Ø., Follows, M. J., & Aksnes, D. L. (2013). Trait-based models of nutrient uptake in microbes extend the Michaelis-Menten framework. *Limnology and Oceanography*, *58*(1), 193–202. https://doi.org/10.4319/lo.2013.58.1.0193

Finke, N., & Jørgensen, B. B. (2008). Response of fermentation and sulfate reduction to experimental temperature changes in temperate and Arctic marine sediments. *ISME Journal*, *2*(8), 815–829. https://doi.org/10.1038/ismej.2008.20

Fissore, C., Giardina, C. P., Kolka, R. K., Trettin, C. C., King, G. M., Jurgensen, M. F., et al. (2008). Temperature and vegetation effects on soil organic carbon quality along a forested mean annual temperature gradient in North America. *Global Change Biology*, *14*(1), 193–205. https://doi.org/10.1111/j.1365-2486.2007.01478.x

Flores, R. M. (2014). Chapter 4 - Coalification, Gasification, and Gas Storage. In R. M. B. T.-C. and C. G. Flores (Ed.) (pp. 167–233). Boston: Elsevier. https://doi.org/https://doi.org/10.1016/B978-0-12-396972-9.00004-5

Foereid, B., Ward, D. S., Mahowald, N., Paterson, E., & Lehmann, J. (2014). The sensitivity of carbon turnover in the community land model to modified assumptions about soil processes. *Earth System Dynamics*, *5*(1), 211–221. https://doi.org/10.5194/esd-5-211-2014

Frank, S. A. (2010). The trade-off between rate and yield in the design of microbial metabolism. *Journal of Evolutionary Biology*, *23*(3), 609–613. https://doi.org/10.1111/j.1420-9101.2010.01930.x

Fredrickson, A. G., & Stephanopoulos, G. (1981). Microbial competition. *Science*, *213*(4511), 972–979.

Friedrich, M., Takács, I., & Tränckner, J. (2015). Physiological adaptation of growth kinetics in activated sludge. *Water Research*, *85*, 22–30. https://doi.org/10.1016/j.watres.2015.08.010

Gershenson, A., Bader, N. E., & Cheng, W. (2009). Effects of substrate availability on the temperature sensitivity of soil organic matter decomposition. *Global Change Biology*, *15*(1), 176–183. https://doi.org/10.1111/j.1365-2486.2008.01827.x

Gill, A. L., Giasson, M. A., Yu, R., & Finzi, A. C. (2017). Deep peat warming increases surface methane and carbon dioxide emissions in a black spruce-dominated ombrotrophic bog. *Global Change Biology*, *23*(12), 5398–5411. https://doi.org/10.1111/gcb.13806

Glissmann, K., & Conrad, R. (2002). Saccharolytic activity and its role as a limiting step in methane formation during the anaerobic degradation of rice straw in rice paddy soil. *Biology and Fertility of Soils*, *35*(1), 62–67. https://doi.org/10.1007/s00374-002-0442-z

Goelzer, A., & Fromion, V. (2011). Bacterial growth rate reflects a bottleneck in resource allocation. *Biochimica et Biophysica Acta - General Subjects*, *1810*(10), 978–988. https://doi.org/10.1016/j.bbagen.2011.05.014

Gonnerman, M. C., Benedict, M. N., Feist, A. M., Metcalf, W. W., & Price, N. D. (2013). Genomically and biochemically accurate metabolic reconstruction of Methanosarcina barkeri Fusaro, iMG746. *Biotechnology Journal*, *8*(9), 1070–1079.

Hagerty, S. B., Van Groenigen, K. J., Allison, S. D., Hungate, B. A., Schwartz, E., Koch, G. W., et al. (2014). Accelerated microbial turnover but constant growth efficiency with warming in soil. *Nature Climate Change*, *4*(10), 903–906. https://doi.org/10.1038/nclimate2361

Hamdi, S., Moyano, F., Sall, S., Bernoux, M., & Chevallier, T. (2013). Synthesis analysis of the temperature sensitivity of soil respiration from laboratory studies in relation to incubation methods and soil conditions. *Soil Biology and Biochemistry*, *58*, 115–126. https://doi.org/10.1016/j.soilbio.2012.11.012

Hansen, L. K., Jakobsen, R., & Postma, D. (2001). Methagnogenesis in a shallow sandy aquifer, Rømø, Denmark. *Geochimica et Cosmochimica Acta*, *65*(17), 2925–2935. https://doi.org/10.1016/S0016-7037(01)00653-6

Hartel, P. G. (2005). Microbial processes | Environmental factors. In D. B. T.-E. of S. in the E. Hillel (Ed.) (pp. 448–455). Oxford: Elsevier. https://doi.org/https://doi.org/10.1016/B0-12-348530-4/00155-7

Healey, F. P. (1980). Slope of the Monod equation as an indicator of advantage in nutrient competition. *Microbial Ecology*, *5*(4), 281–286.

Heinrich, R., Schuster, S., & Holzhütter, H.-G. (1991). Mathematical analysis of enzymic reaction systems using optimization principles. *EJB Reviews 1991*, 167–187.

Heirendt, L., Arreckx, S., Pfau, T., Mendoza, S. N., Richelle, A., Heinken, A., et al. (2011). Creation and analysis of biochemical constraint-based models using the COBRA Toolbox v.3.0. *Nat. Protoc*, *6*, 1290–1307. https://doi.org/10.1038/nprot.2007.99

Heitzer, A., Kohler, H. P. E., Reichert, P., & Hamer, G. (1991). Utility of phenomenological models for describing temperature dependence of bacterial growth. *Applied and Environmental Microbiology*, *57*(9), 2656–2665. https://doi.org/10.1128/aem.57.9.2656-2665.1991

Helling, R. B. (2002). Speed versus efficiency in microbial growth and the role of parallel pathways. *Journal of Bacteriology*, *184*(4), 1041–1045. https://doi.org/10.1128/jb.184.4.1041-1045.2002

Herndon, E. M., Mann, B. F., Roy Chowdhury, T., Yang, Z., Wullschleger, S. D., Graham, D., et al. (2015). Pathways of anaerobic organic matter decomposition in tundra soils from Barrow, Alaska. *Journal of Geophysical Research G: Biogeosciences*, *120*(11), 2345–2359. https://doi.org/10.1002/2015JG003147

Heslop, J. K., Walter Anthony, K. M., Grosse, G., Liebner, S., & Winkel, M. (2019). Century-scale time since permafrost thaw affects temperature sensitivity of net methane production in thermokarst-lake and talik sediments. *Science of the Total Environment*, *691*, 124–134. https://doi.org/10.1016/j.scitotenv.2019.06.402

Hilasvuori, E., Akujärvi, A., Fritze, H., Karhu, K., Laiho, R., Mäkiranta, P., et al. (2013). Temperature sensitivity of decomposition in a peat profile. *Soil Biology and Biochemistry*, *67*, 47–54. https://doi.org/10.1016/j.soilbio.2013.08.009

Hoehler, T., Losey, A, N., Robert, G. P., & McInerney, J. M. (2009). Environmental constraints that limit methanogenesis. *Asuhan Kebidanan Ibu Hamil*, *53*(9), 1689–1699. https://doi.org/10.1017/CBO9781107415324.004

Hoehler, T. M., & Jørgensen, B. B. (2013). Microbial life under extreme energy limitation. *Nature Reviews Microbiology*. Nature Publishing Group. https://doi.org/10.1038/nrmicro2939

Hoff, J. H. van't. (1898). *Lectures in theoretical and physical chemistry : part I : chemical dynamics LK - https://UOLibraries.on.worldcat.org/oclc/220605730*. *Edward Arnold, London*. London SE - 254 pages ; 23 cm: Edward Arnold.

Holmes, D. E., Giloteaux, L., Barlett, M., Chavan, M. A., Smith, J. A., Williams, K. H., et al. (2013). Molecular analysis of the In situ growth rates of subsurface geobacter species. *Applied and Environmental Microbiology*, *79*(5), 1646–1653. https://doi.org/10.1128/AEM.03263-12

Hopkins, F. M., Filley, T. R., Gleixner, G., Lange, M., Top, S. M., & Trumbore, S. E. (2014). Increased belowground carbon inputs and warming promote loss ofsoil organic carbon through complementary microbial responses. *Soil Biology and Biochemistry*, *76*, 57–69. https://doi.org/10.1016/j.soilbio.2014.04.028

Hopple, A. M., Wilson, R. M., Kolton, M., Zalman, C. A., Chanton, J. P., Kostka, J., et al. (2020). Massive peatland carbon banks vulnerable to rising temperatures. *Nature Communications*, *11*(1), 4–10. https://doi.org/10.1038/s41467-020-16311-8

Hui, S., Silverman, J. M., Chen, S. S., Erickson, D. W., Basan, M., Wang, J., et al. (2015). Quantitative proteomic analysis reveals a simple strategy of global resource allocation in bacteria. *Molecular Systems Biology*, *11*(2), 784. https://doi.org/10.15252/msb.20145697

Van Hulzen, J. B., Segers, R., Van Bodegom, P. M., & Leffelaar, P. A. (1999). Temperature effects on soil methane production: An explanation for observed variability. *Soil Biology and Biochemistry*, *31*(14), 1919–1929. https://doi.org/10.1016/S0038-0717(99)00109-1

Hungate, R. E. (1967). Hydrogen as an intermediate in the rumen fermentation. *Archiv Für Mikrobiologie*, *59*(1–3), 158–164.

Inglett, K. S., Inglett, P. W., Reddy, K. R., & Osborne, T. Z. (2012). Temperature sensitivity of greenhouse gas production in wetland soils of different vegetation. *Biogeochemistry*, *108*(1–3), 77–90. https://doi.org/10.1007/s10533-011-9573-3

Jackson, R. B., Saunois, M., Bousquet, P., Canadell, J. G., Poulter, B., Stavert, A. R., et al. (2020). Increasing anthropogenic methane emissions arise equally from agricultural and fossil fuel sources. *Environmental Research Letters*, *15*(7). https://doi.org/10.1088/1748-9326/ab9ed2

Jetten, M. S. M., Stams, A. J. M., & Zehnder, A. J. B. (1989). Isolation and characterization of acetyl-coenzyme A synthetase from Methanothrix soehngenii. *Journal of Bacteriology*, *171*(10), 5430–5435. https://doi.org/10.1128/jb.171.10.5430-5435.1989

Jiang, N., Wang, Y., & Dong, X. (2010). Methanol as the primary methanogenic and acetogenic precursor in the cold Zoige wetland at Tibetan Plateau. *Microbial Ecology*, *60*(1), 206–213.

Jin, Q. (2012). Energy conservation of anaerobic respiration. *American Journal of Science*, *312*(6), 573–628. https://doi.org/10.2475/06.2012.01

Jin, Q., & Bethke, C. M. (2003). A new rate law describing microbial respiration. *Applied and Environmental Microbiology*, *69*(4), 2340–2348. https://doi.org/10.1128/AEM.69.4.2340-2348.2003

Jin, Q., & Bethke, C. M. (2005). Predicting the rate of microbial respiration in geochemical environments. *Geochimica et Cosmochimica Acta*, *69*(5), 1133–1143. https://doi.org/10.1016/j.gca.2004.08.010

Jin, Q., & Kirk, M. F. (2018). pH as a Primary Control in Environmental Microbiology: 2. Kinetic Perspective. *Frontiers in Environmental Science*, *6*(September), 1–16. https://doi.org/10.3389/fenvs.2018.00101

Jin, Q., Roden, E. E., & Giska, J. R. (2013a). Geomicrobial Kinetics: Extrapolating Laboratory Studies to Natural Environments. *Geomicrobiology Journal*, *30*(2), 173–185. https://doi.org/10.1080/01490451.2011.653084

Jin, Q., Roden, E. E., & Giska, J. R. (2013b). Geomicrobial Kinetics: Extrapolating Laboratory Studies to Natural Environments. *Geomicrobiology Journal*, *30*(2), 173–185. https://doi.org/10.1080/01490451.2011.653084

Johnson, J. W., Oelkers, E. H., & Helgeson, H. C. (1992). *SUPCRT92: A software package for calculating the standard molal thermodynamic properties of minerals, gases, aqueous species, and reactions from 1 to 5000 bar and 0 to 1000°C*. *Computers and Geosciences* (Vol. 18). https://doi.org/10.1016/0098-3004(92)90029-Q

Kacser, H., Burns, J. A., Kacser, H., & Fell, D. A. (1995). The control of flux. *Biochemical Society Transactions*, *23*(2), 341–366.

Kaster, A.-K., Moll, J., Parey, K., & Thauer, R. K. (2011). Coupling of ferredoxin and heterodisulfide reduction via electron bifurcation in hydrogenotrophic methanogenic archaea. *Proceedings of the National Academy of Sciences*, *108*(7), 2981–2986. https://doi.org/10.1073/PNAS.1016761108

Kilham, P., & Hecky, R. E. (1988). Comparative ecology of marine and freshwater phytoplankton. *Limnology and Oceanography*, *33*(4part2), 776–795. https://doi.org/10.4319/lo.1988.33.4part2.0776

Kim, Y., Ingram, L. O., & Shanmugam, K. T. (2007). Construction of an Escherichia coli K-12 mutant for homoethanologenic fermentation of glucose or xylose without foreign genes. *Applied and Environmental Microbiology*, *73*(6), 1766–1771. https://doi.org/10.1128/AEM.02456-06

Klipp, E., & Heinrich, R. (1999). *Competition for enzymes in metabolic pathways: Implications for optimal distributions of enzyme concentrations and for the distribution of flux control*. *BioSystems* (Vol. 54). Retrieved from www.elsevier.com

Kolton, M., Marks, A., Wilson, R. M., Chanton, J. P., & Kostka, J. E. (2019). Impact of warming on greenhouse gas production and microbial diversity in anoxic peat from a Sphagnum-dominated bog (Grand Rapids, Minnesota, United States). *Frontiers in Microbiology*, *10*(APR), 1–13. https://doi.org/10.3389/fmicb.2019.00870

Kotelnikova, S. (2002). Microbial production and oxidation of methane in deep subsurface. *Earth-Science Reviews*, *58*(3–4), 367–395. https://doi.org/10.1016/S0012-8252(01)00082-4

Kovárová-Kovar, K., & Egli, T. (1998). Growth Kinetics of Suspended Microbial Cells: From Single-Substrate-Controlled Growth to Mixed-Substrate Kinetics. *Microbiology and Molecular Biology Reviews*, *62*(3), 646–666. https://doi.org/10.1128/mmbr.62.3.646-666.1998

Kulkarni, G., Mand, T. D., & Metcalf, W. W. (2018). Energy conservation via hydrogen cycling in the methanogenic archaeon Methanosarcina barkeri. *MBio*, *9*(4), 1–10. https://doi.org/10.1128/mBio.01256-18

Kwietniewska, E., & Tys, J. (2014). Process characteristics, inhibition factors and methane yields of anaerobic digestion process, with particular focus on microalgal biomass fermentation. *Renewable and Sustainable Energy Reviews*, *34*, 491–500. https://doi.org/10.1016/j.rser.2014.03.041

Lashof, D. A., & Ahujah, D. R. (n.d.). *Relative contributions of greenhouse gas emissions to global warming*.

Lee, H. S., Salerno, M. B., & Rittmann, B. E. (2008). Thermodynamic evaluation on H2 production in glucose fermentation. *Environmental Science and Technology*, *42*(7), 2401–2407. https://doi.org/10.1021/es702610v

Leroi, A. M., Bennett, A. F., & Lenski, R. E. (1994). *Temperature acclimation and competitive fitness: An experimental test of the beneficial acclimation assumption (physiologcal ecology/thermotolerance/heat shock response/bacteria/Eschenckia colt)* (Vol. 91).

Li, G. W., Burkhardt, D., Gross, C., & Weissman, J. S. (2014). Quantifying absolute protein synthesis rates reveals principles underlying allocation of cellular resources. *Cell*, *157*(3), 624–635. https://doi.org/10.1016/j.cell.2014.02.033

Li, J., Yan, D., Pendall, E., Pei, J., Noh, N. J., He, J. S., et al. (2018). Depth dependence of soil carbon temperature sensitivity across Tibetan permafrost regions. *Soil Biology and Biochemistry*, *126*(August), 82–90.

Litchman, E., Klausmeier, C. A., Schofield, O. M., & Falkowski, P. G. (2007). The role of functional traits and trade-offs in structuring phytoplankton communities: Scaling from cellular to ecosystem level. *Ecology Letters*, *10*(12), 1170–1181. https://doi.org/10.1111/j.1461-0248.2007.01117.x

Litchman, E., Edwards, K. F., & Klausmeier, C. A. (2015). Microbial resource utilization traits and trade-offs: Implications for community structure, functioning, and biogeochemical impacts at present and in the future. *Frontiers in Microbiology*. https://doi.org/10.3389/fmicb.2015.00254

Liu, Y. (2007). Overview of some theoretical approaches for derivation of the Monod equation. *Applied Microbiology and Biotechnology*, *73*(6), 1241–1250. https://doi.org/10.1007/s00253-006-0717-7

Lovley, D. R., & Ferry, J. G. (1985). Production and consumption of H2 during growth of Methanosarcina spp. on acetate. *Applied and Environmental Microbiology*, *49*(1), 247–249. https://doi.org/10.1128/aem.49.1.247-249.1985

Lovley, D. R., & Klug, M. J. (1982). Intermediary metabolism of organic matter in the sediments of a eutrophic lake. *Applied and Environmental Microbiology*, *43*(3), 552–560. https://doi.org/10.1128/aem.43.3.552-560.1982

Lovley, D. R., Dwyer, D. F., & Klug, M. J. (1982). Kinetic analysiis of competition between sulfate reducers and methanogens for hydrogen in sediments. *Applied and Environmental Microbiology*, *43*(6), 1373–1379. https://doi.org/10.1128/aem.43.6.1373-1379.1982

Lovley, Derek R, & Klug, M. J. (1986). Model for the distribution of sulfate reduction and methanogenesis in freshwater sediments. *Geochim. Cosmochim. Acta*, *50*(1), 11–18.

Lupascu, M., Wadham, J., Hornibrook, E., & Pancost, R. (2012). Temperature sensitivity of methane production in the permafrost active layer at Stordalen, Sweden: A comparison with non-permafrost Northern Wetlands. *Arctic, Antarctic, and Alpine Research*, *44*(4), 469–482. https://doi.org/10.1657/1938-4246-44.4.469

von Lützow, M., & Kögel-Knabner, I. (2009). Temperature sensitivity of soil organic matter decomposition-what do we know? *Biology and Fertility of Soils*, *46*(1), 1–15. https://doi.org/10.1007/s00374-009-0413-8

Malik, A. A., Martiny, J. B. H., Brodie, E. L., Martiny, A. C., Treseder, K. K., & Allison, S. D. (2020). Defining trait-based microbial strategies with consequences for soil carbon cycling under climate change. *ISME Journal*, *14*(1), 1–9. https://doi.org/10.1038/s41396-019-0510-0

Martens-Habbena, W., Berube, P. M., Urakawa, H., De La Torre, J. R., & Stahl, D. A. (2009). Ammonia oxidation kinetics determine niche separation of nitrifying Archaea and Bacteria. *Nature*, *461*(7266), 976–979. https://doi.org/10.1038/nature08465

Megonigal, J. P., Hines, M. E., & Visscher, P. T. (2003). Anaerobic metabolism: linkages to trace gases and aerobic processes. In H. D. Holland & K. K. B. T. Turekian (Eds.) (pp. 317–424). Oxford: Pergamon. https://doi.org/https://doi.org/10.1016/B0-08-043751-6/08132-9

Meyer, N., Meyer, H., Welp, G., & Amelung, W. (2018). Soil respiration and its temperature sensitivity (Q10): Rapid acquisition using mid-infrared spectroscopy. *Geoderma*, *323*(March), 31–40. https://doi.org/10.1016/j.geoderma.2018.02.031

Millard, P., Smallbone, K., & Mendes, P. (2017). Metabolic regulation is sufficient for global and robust coordination of glucose uptake, catabolism, energy production and growth in Escherichia coli. https://doi.org/10.1371/journal.pcbi.1005396

Min, H., & Zinder, S. H. (1989). Kinetics of Acetate Utilization by Two Thermophilic Acetotrophic Methanogens: Methanosarcina sp. Strain CALS-1 and Methanothrix sp. Strain CALS-1. *Applied and Environmental Microbiology*, *55*(2), 488–491. https://doi.org/10.1128/aem.55.2.488-491.1989

Molenaar, D., Van Berlo, R., De Ridder, D., & Teusink, B. (2009). Shifts in growth strategies reflect tradeoffs in cellular economics. *Molecular Systems Biology*, *5*(323), 1–10. https://doi.org/10.1038/msb.2009.82

Mori, M., Hwa, T., Martin, O. C., De Martino, A., & Marinari, E. (2016a). Constrained Allocation Flux Balance Analysis. *PLoS Computational Biology*, *12*(6), 1–24. https://doi.org/10.1371/journal.pcbi.1004913

Mori, M., Hwa, T., Martin, O. C., De Martino, A., & Marinari, E. (2016b). Constrained Allocation Flux Balance Analysis. *Balance Analysis. PLoS Comput Biol*, *12*(6), 1004913. https://doi.org/10.1371/journal.pcbi.1004913

Morrissey, E. M., Berrier, D. J., Neubauer, S. C., & Franklin, R. B. (2014). Using microbial communities and extracellular enzymes to link soil organic matter characteristics to greenhouse gas production in a tidal freshwater wetland. *Biogeochemistry*, *117*(2–3), 473–490. https://doi.org/10.1007/s10533-013-9894-5

Mouser, P. J., Borton, M., Darrah, T. H., Hartsock, A., & Wrighton, K. C. (2016). Hydraulic fracturing offers view of microbial life in the deep terrestrial subsurface AN OVERVIEW OF BLACK SHALE GEOLOGY AND THE HYDRAULIC FRACTURING PROCESS. *FEMS Microbiology Ecology*, *92*, 166. https://doi.org/10.1093/femsec/fiw166

Mu, C., Li, L., Wu, X., Zhang, F., Jia, L., Zhao, Q., & Zhang, T. (2018). Greenhouse gas released from the deep permafrost in the northern Qinghai-Tibetan Plateau. *Scientific Reports*, *8*(1), 1–9. https://doi.org/10.1038/s41598-018-22530-3

Nazaries, L., Murrell, J. C., Millard, P., Baggs, L., & Singh, B. K. (2013). Methane, microbes and models: Fundamental understanding of the soil methane cycle for future predictions. *Environmental Microbiology*, *15*(9), 2395–2417. https://doi.org/10.1111/1462-2920.12149

Nirody, J. A., Budin, I., & Rangamani, P. (2020). ATP synthase: Evolution, energetics, and membrane interactions. *ArXiv*, *152*(11), 1–18.

Nisbet, E. G., Dlugokencky, E. J., Manning, M. R., Lowry, D., Fisher, R. E., France, J. L., et al. (2016). Global Biogeochemical Cycles, 1356–1370. https://doi.org/10.1002/2016GB005406.Received

Noor, E., Flamholz, A., Liebermeister, W., Bar-Even, A., & Milo, R. (2013). A note on the kinetics of enzyme action: A decomposition that highlights thermodynamic effects. *FEBS Letters*. Federation of European Biochemical Societies. https://doi.org/10.1016/j.febslet.2013.07.028

Northrop, D. B. (1998). On the meaning of Km and V/K in enzyme kinetics. *Journal of Chemical Education*, *75*(9), 1153–1157. https://doi.org/10.1021/ed075p1153

Nykanen, H., Alm, J., Silvola, J., Tolonen, K., & Martikainen, P. J. (1998). Methane fluxes on boreal peatlands of different fertility and the effect of long-term experimental lowering of the water table on flux rates. *Global Biogeochemical Cycles*, *12*(1), 53–69. https://doi.org/10.1029/97GB02732

Pahlow, M. (2005). Linking chlorophyll-nutrient dynamics to the Redfield N:C ratio with a model of optimal phytoplankton growth. *Marine Ecology Progress Series*, *287*, 33–43.

Pallud, C., & Van Cappellen, P. (2006). Kinetics of microbial sulfate reduction in estuarine sediments. *Geochimica et Cosmochimica Acta*, *70*(5), 1148–1162. https://doi.org/10.1016/j.gca.2005.11.002

Pancost, R. D., Sinninghe Damsté, J. S., De Lint, S., Van Der Maarel, M. J. E. C., & Gottschal, J. C. (2000). Biomarker evidence for widespread anaerobic methane oxidation in Mediterranean sediments by a consortium of methanogenic archaea and bacteria. *Applied and Environmental Microbiology*, *66*(3), 1126–1132. https://doi.org/10.1128/AEM.66.3.1126-1132.2000

Panikov, N. S. (1995). Microbial growth kinetics.

Parashar, C. D., Gupta, K. P., Rai, J., Sharma, C. R., & Singh, N. (1993). Effect of soil temperature on methane emission from paddy fields. *Chemosphere*, *26*(1–3), 247–250.

Park, J. O., Rubin, S. A., Xu, Y. F., Amador-Noguez, D., Fan, J., Shlomi, T., & Rabinowitz, J. D. (2016). Metabolite concentrations, fluxes and free energies imply efficient enzyme usage. *Nature Chemical Biology*, *12*(7), 482–489. https://doi.org/10.1038/nchembio.2077

Peña-Villalobos, I., Casanova-Maldonado, I., Lois, P., Palma, V., & Sabat, P. (2020). Costs of exploratory behavior: the energy trade-off hypothesis and the allocation model tested under caloric restriction. *Scientific Reports*, *10*(1), 1–13. https://doi.org/10.1038/s41598-020-61102-2

Peterson, J. R., Labhsetwar, P., Ellermeier, J. R., Kohler, P. R. A., Jain, A., Ha, T., et al. (2014). Towards a computational model of a methane producing archaeum. *Archaea*, *2014*. https://doi.org/10.1155/2014/898453

Pfeiffer, T., Schuster, S., & Bonhoeffer, S. (2001). Cooperation and Competition in the Evolution of ATP-Producing Pathways. *Science*, *292*(5516), 504–507. https://doi.org/10.1126/science.1058079

de Poorter, L. M. I., Geerts, W. J., & Keltjens, J. T. (2005). Hydrogen concentrations in methane-forming cells probed by the ratios of reduced and oxidized coenzyme F420. *Microbiology*, *151*(5), 1697–1705. https://doi.org/10.1099/mic.0.27679-0

Prakash, D., Chauhan, S. S., & Ferry, J. G. (2019). Life on the thermodynamic edge: Respiratory growth of an acetotrophic methanogen. *Science Advances*, *5*(8), 1–7. https://doi.org/10.1126/sciadv.aaw9059

Price, P. B., & Sowers, T. (2004). Temperature dependence of metabolic rates for microbial growth, maintenance, and survival. *Proceedings of the National Academy of Sciences*, *101*(13), 4631–4636. https://doi.org/10.1073/pnas.0400522101

Raich, J. W., Rastetter, E. B., Melillo, J. M., Kicklighter, D. W., Steudler, P. A., Peterson, B. J., et al. (1991). Potential net primary productivity in South America : application of a global model. *Ecological Application*, (1(4)), 399–429.

Raich, J. W., Russell, E. A., Kitayama, K., Parton, J. W., & Vitousek, M. P. (2006). Temperature influences carbon accumlation in moist tropical forests. *Ecology*, *87(1)*, 76–87.

Rajoka, M. I., Tabassum, R., & Malik, K. A. (1999). methane in batch cultures using Methanosarcina mazei, *67*, 305–311.

Ratkowsky, D. A., Lowry, R. K., McMeekin, T. A., Stokes, A. N., & Chandler, R. E. (1983). Model for bacterial culture growth rate throughout the entire biokinetic temperature range. *Journal of Bacteriology*, *154*(3), 1222–1226. https://doi.org/10.1128/jb.154.3.1222-1226.1983

Risso, C., Methé, B. A., Elifantz, H., & Holmes, D. E. (2008). Highly conserved genes in geobacter species with expression patterns indicative of acetate limitation. *Microbiology*, *154*(9), 2589–2599. https://doi.org/10.1099/mic.0.2008/017244-0

Roden, E. E., & Wetzel, R. G. (2003). Competition between Fe(III)-reducing and methanogenic bacteria for acetate in iron-rich freshwater sediments. *Microbial Ecology*, *45*(3), 252–258. https://doi.org/10.1007/s00248-002-1037-9

Romero-Olivares, A. L., Allison, S. D., & Treseder, K. K. (2017). Soil microbes and their response to experimental warming over time: A meta-analysis of field studies. *Soil Biology and Biochemistry*, *107*, 32–40. https://doi.org/10.1016/j.soilbio.2016.12.026

Rosenberg, E., DeLong, E. F., Lory, S., Stackebrandt, E., & Thompson, F. (2014). The prokaryotes: other major lineages of bacteria and the archaea.

Rosso, L., Lobry, J. R., Bajard, S., & Flandrois, J. P. (1995). Convenient model to describe the combined effects of temperature and pH on microbial growth. *Applied and Environmental Microbiology*, *61*(2), 610–616. https://doi.org/10.1128/aem.61.2.610-616.1995

Rossol, L., Lobry, J. R., & Flandrois, J. P. (1993). An unexpected correlation between cardinal temperatures of microbial growth highlighted by a new model. *Journal of Theoretical Biology*, *162*, 447–463.

Schaefer, H., Fletcher, S. E. M., Veidt, C., Lassey, K. R., Brailsford, G. W., Bromley, T. M., et al. (2016). A 21st-century shift from fossil-fuel to biogenic methane emissions indicated by 13CH4. *Science*, *352*(6281), 80–84. https://doi.org/10.1126/science.aad2705

Schink, B. (1997). Energetics of syntrophic cooperation in methanogenic degradation. *Microbiology and Molecular Biology Reviews : MMBR*, *61*(2), 262–280. https://doi.org/10.1128/.61.2.262-280.1997

Schink, B., & Stams, A. (2013). Syntrophism among prokaryotes In The Prokaryotes. *Rosenberg E., Editor*, 471–493.

Schipper, L. A., Hobbs, J. K., Rutledge, S., & Arcus, V. L. (2014). Thermodynamic theory explains the temperature optima of soil microbial processes and high Q10 values at low temperatures. *Global Change Biology*, *20*(11), 3578–3586. https://doi.org/10.1111/gcb.12596

Schoelmerich, M. C., & Müller, V. (2019). Energy conservation by a hydrogenase-dependent chemiosmotic mechanism in an ancient metabolic pathway. *Proceedings of the National Academy of Sciences of the United States of America*, *116*(13), 6329–6334. https://doi.org/10.1073/pnas.1818580116

Scott, M., Gunderson, C. W., Mateescu, E. M., Zhang, Z., & Hwa, T. (2010). Interdependence of Cell Growth. *Science*, *330*(6007), 1099–1102. Retrieved from http://www.ncbi.nlm.nih.gov/pubmed/21097934

Sha, C., Mitsch, W. J., Mander, Ü., Lu, J., Batson, J., Zhang, L., & He, W. (2011). Methane emissions from freshwater riverine wetlands. *Ecological Engineering*, *37*(1), 16–24. https://doi.org/10.1016/j.ecoleng.2010.07.022

Shapiro, B., Hoehler, T. M., & Jin, Q. (2018). Integrating genome-scale metabolic models into the prediction of microbial kinetics in natural environments. *Geochimica et Cosmochimica Acta*, *242*, 102–122. https://doi.org/10.1016/j.gca.2018.08.047

Shiloach, J., Kaufman, J., Guillard, A. S., & Fass, R. (1996). Effect of glucose supply strategy on acetate accumulation, growth, and recombinant protein production by Escherichia coli BL21 (λDE3) and Escherichia coli JM109. *Biotechnology and Bioengineering*, *49*(4), 421–428. https://doi.org/10.1002/(SICI)1097-0290(19960220)49:4<421::AID-BIT9>3.0.CO;2-R

Singh-Wissmann, K., & Ferry, J. G. (1995). Transcriptional regulation of the phosphotransacetylase-encoding and acetate kinase-encoding genes (pta and ack) from Methanosarcina thermophila. *Journal of Bacteriology*, *177*(7), 1699–1702. https://doi.org/10.1128/jb.177.7.1699-1702.1995

Singh, V., & Das, D. (2019). Chapter 3 - Potential of Hydrogen Production From Biomass. In P. E. V. B. T.-S. and E. of H.-B. E. T. de Miranda (Ed.) (pp. 123–164). Academic Press. https://doi.org/https://doi.org/10.1016/B978-0-12-814251-6.00003-4

Smith, K. S., & Ingram-Smith, C. (2007). Methanosaeta, the forgotten methanogen? *Trends in Microbiology*, *15*(4), 150–155. https://doi.org/10.1016/j.tim.2007.02.002

Smith, S. L., & Yamanaka, Y. (2007). Optimization-based model of multinutrient uptake kinetics. *Limnology and Oceanography*, *52*(4), 1545–1558. https://doi.org/10.4319/lo.2007.52.4.1545

Smith, S. L., Merico, A., Wirtz, K. W., & Pahlow, M. (2014). Leaving misleading legacies behind in plankton ecosystem modelling. *Journal of Plankton Research*, *36*(3), 613–620. https://doi.org/10.1093/plankt/fbu011

Stams, A. J. M., Elferink, S. J. W. H. O., & Westermann, P. (2003). Metabolic Interactions Between Methanogenic Consortia and Anaerobic Respiring Bacteria. In B. K. Ahring, I. Angelidaki, E. C. de Macario, H. N. Gavala, J. Hofman-Bang, A. J. L. Macario, et al. (Eds.), *Biomethanation I* (pp. 31–56). Berlin, Heidelberg: Springer Berlin Heidelberg. https://doi.org/10.1007/3-540-45839-5_2

Stone, M. M., Weiss, M. S., Goodale, C. L., Adams, M. B., Fernandez, I. J., German, D. P., & Allison, S. D. (2012). Temperature sensitivity of soil enzyme kinetics under N-fertilization in two temperate forests. *Global Change Biology*, *18*(3), 1173–1184. https://doi.org/10.1111/j.1365-2486.2011.02545.x

Svensson, B. H. (1984). Different temperature optima for methane formation when enrichments from acid peat are supplemented with acetate or hydrogen. *Applied and Environmental Microbiology*, *48*(2), 389–394. https://doi.org/10.1128/aem.48.2.389-394.1984

Tang, G., Zheng, J., Xu, X., Yang, Z., Graham, D. E., Gu, B., et al. (2016). Biogeochemical modeling of CO2 and CH4 production in anoxic Arctic soil microcosms. *Biogeosciences*, *13*(17), 5021–5041. https://doi.org/10.5194/bg-13-5021-2016

Teusink, B., Passarge, J., Reijenga, C. A., Esgalhado, E., Weijden, C. C. Van Der, Schepper, M., et al. (2000). Can yeast glycolysis be understood in terms of in vitro kinetics of the constituent enzymes ? Testing biochemistry, *5329*(May).

Thauer, R. K., Kaster, A. K., Seedorf, H., Buckel, W., & Hedderich, R. (2008). Methanogenic archaea: Ecologically relevant differences in energy conservation. *Nature Reviews Microbiology*, *6*(8), 579–591. https://doi.org/10.1038/nrmicro1931

Thor, S., Peterson, J. R., & Luthey-Schulten, Z. (2017). Genome-Scale Metabolic Modeling of Archaea Lends Insight into Diversity of Metabolic Function. *Archaea*, *2017*. https://doi.org/10.1155/2017/9763848

Todd-brown, K. E. O., Zheng, B., & Crowther, T. W. (2018). Field-warmed soil carbon changes imply high 21st-century modeling uncertainty. *Biogeosciences*, *15*, 3659–3671. https://doi.org/10.3929/ethz-a-010782581

Todd-Brown, K. E. O., Randerson, J. T., Post, W. M., Hoffman, F. M., Tarnocai, C., Schuur, E. A. G., & Allison, S. D. (2013). Causes of variation in soil carbon simulations from CMIP5 Earth system models and comparison with observations. *Biogeosciences*, *10*(3), 1717–1736. https://doi.org/10.5194/bg-10-1717-2013

Villaverde, A. F., Bongard, S., Mauch, K., Balsa-Canto, E., & Banga, J. R. (2016). Metabolic engineering with multi-objective optimization of kinetic models. *Journal of Biotechnology*, *222*, 1–8. https://doi.org/10.1016/j.jbiotec.2016.01.005

Wagai, R., Kishimoto-Mo, A. W., Yonemura, S., Shirato, Y., Hiradate, S., & Yagasaki, Y. (2013). Linking temperature sensitivity of soil organic matter decomposition to its molecular structure, accessibility, and microbial physiology. *Global Change Biology*, *19*(4), 1114–1125. https://doi.org/10.1111/gcb.12112

Wang, Q., Liu, S., & Tian, P. (2018). Carbon quality and soil microbial property control the latitudinal pattern in temperature sensitivity of soil microbial respiration across Chinese forest ecosystems. *Global Change Biology*, *24*(7), 2841–2849. https://doi.org/10.1111/gcb.14105

Welte, C., & Deppenmeier, U. (2014). Bioenergetics and anaerobic respiratory chains of aceticlastic methanogens. *Biochimica et Biophysica Acta - Bioenergetics*, *1837*(7), 1130–1147. https://doi.org/10.1016/j.bbabio.2013.12.002

Welte, C., Krätzer, C., & Deppenmeier, U. (2010). Involvement of Ech hydrogenase in energy conservation of Methanosarcina mazei. *FEBS Journal*, *277*(16), 3396–3403. https://doi.org/10.1111/j.1742-4658.2010.07744.x

Wik, M., Varner, R. K., Anthony, K. W., MacIntyre, S., & Bastviken, D. (2016). Climate-sensitive northern lakes and ponds are critical components of methane release. *Nature Geoscience*. Nature Publishing Group. https://doi.org/10.1038/ngeo2578

Wilkins, M. J., Callister, S. J., Miletto, M., Williams, K. H., Nicora, C. D., Lovley, D. R., et al. (2011). Development of a biomarker for Geobacter activity and strain composition; Proteogenomic analysis of the citrate synthase protein during bioremediation of U(VI). *Microbial Biotechnology*, *4*(1), 55–63. https://doi.org/10.1111/j.1751-7915.2010.00194.x

Wu, Q., Ye, R., Bridgham, S., & Jin, Q. (2021a). Phreeqc script. https://doi.org/DOI: 10.5281/zenodo.4480176

Wu, Q., Ye, R., Bridgham, S., & Jin, Q. (2021b). Q10 dataset. https://doi.org/10.5281/zenodo.4480066

Xia, Q., Wang, T., Hendrickson, E. L., Lie, T. J., Hackett, M., & Leigh, J. A. (2009). Quantitative proteomics of nutrient limitation in the hydrogenotrophic methanogen Methanococcus maripaludis. https://doi.org/10.1186/1471-2180-9-149

Xu, X., Shi, Z., Li, D., Rey, A., Ruan, H., Craine, J. M., et al. (2016). Soil properties control decomposition of soil organic carbon: Results from data-assimilation analysis. *Geoderma*, *262*, 235–242. https://doi.org/10.1016/j.geoderma.2015.08.038

Ye, R., Jin, Q., Bohannan, B., Keller, J. K., McAllister, S. A., & Bridgham, S. D. (2012). PH controls over anaerobic carbon mineralization, the efficiency of methane production, and methanogenic pathways in peatlands across an ombrotrophic-minerotrophic gradient. *Soil Biology and Biochemistry*, *54*, 36–47. https://doi.org/10.1016/j.soilbio.2012.05.015

Ye, R., Keller, J. K., Jin, Q., Bohannan, B. J. M., & Bridgham, S. D. (2016). Peatland types influence the inhibitory effects of a humic substance analog on methane production. *Geoderma*, *265*, 131–140. https://doi.org/10.1016/j.geoderma.2015.11.026

Zheng, J., Thornton, P. E., Painter, S. L., Gu, B., Wullschleger, S. D., & Graham, D. E. (2019). Modeling anaerobic soil organic carbon decomposition in Arctic polygon tundra: Insights into soil geochemical influences on carbon mineralization. *Biogeosciences*, *16*(3), 663–680. https://doi.org/10.5194/bg-16-663-2019

Zhuang, G. C., Heuer, V. B., Lazar, C. S., Goldhammer, T., Wendt, J., Samarkin, V. A., et al. (2018). Relative importance of methylotrophic methanogenesis in sediments of the Western Mediterranean Sea. *Geochimica et Cosmochimica Acta*, *224*, 171–186. https://doi.org/10.1016/j.gca.2017.12.024

Ziemiński, K., & Frac, M. (2012). Methane fermentation process as anaerobic digestion of biomass: Transformations, stages and microorganisms. *African Journal of Biotechnology*, *11*(18), 4127–4139. https://doi.org/10.5897/ajbx11.054